2008-10-31

Surface Relief D-Fiber Bragg Gratings for Sensing Applications

Tyson Lee Lowder
Brigham Young University - Provo

SURFACE RELIEF D-FIBER BRAGG GRATINGS FOR SENSING APPLICATIONS

by

Tyson L. Lowder

A dissertation submitted to the faculty of

Brigham Young University

in partial fulfillment of the requirements for the degree of

Doctor of Philosophy

Department of Electrical and Computer Engineering

Brigham Young University

December 2008

BRIGHAM YOUNG UNIVERSITY

GRADUATE COMMITTEE APPROVAL

of a dissertation submitted by

Tyson L. Lowder

This dissertation has been read by each member of the following graduate committee and by majority vote has been found to be satisfactory.

Date	Stephen M. Schultz, Chair
Date	Richard H. Selfridge
Date	Aaron R. Hawkins
Date	Gregory P. Nordin
Date	Karl F. Warnick

BRIGHAM YOUNG UNIVERSITY

As chair of the candidate's graduate committee, I have read the dissertation of Tyson L. Lowder in its final form and have found that (1) its format, citations, and bibliographical style are consistent and acceptable and fulfill university and department style requirements; (2) its illustrative materials including figures, tables, and charts are in place; and (3) the final manuscript is satisfactory to the graduate committee and is ready for submission to the university library.

Date

Stephen M. Schultz
Chair, Graduate Committee

Accepted for the Department

Michael J. Wirthlin
Graduate Coordinator

Accepted for the College

Alan R. Parkinson
Dean, Ira A. Fulton
College of Engineering and Technology

ABSTRACT

SURFACE RELIEF D-FIBER BRAGG GRATINGS FOR SENSING APPLICATIONS

Tyson L. Lowder

Electrical and Computer Engineering

Doctor of Philosophy

This dissertation presents the novel creation of a surface relief fiber Bragg grating on the flat surface of a D-shaped optical fiber. In order to produce an efficient surface relief grating the grating must be etched into the surface of the glass fiber close to the core. A short etch that removes the cladding above the core is performed in order to decrease the core-to-flat distance and allow the light to interact with the grating on the flat surface. Due to the unique D-shape of the optical fiber the mechanical integrity of the fiber remains high even after the fabrication process.

For traditional fiber Bragg gratings the index modulation occurs in the core of the optical fiber. While this method can produce highly reflective gratings they are not well suited for many sensing applications. For example, the operating temperature range is limited to a few hundred degrees Celsius before the index modulation returns to a more uniform index profile. Also because the gratings are created in the core of the fiber, interaction with the surrounding environment is limited.

The surface relief fiber Bragg grating created for this work overcomes some of the sensing challenges of traditional gratings. The major accomplishments of this

dissertation are a dramatic increase in operating temperature to over 1000°C, the ability to measure multi-dimensional bend, the ability to measure material changes around the fiber such as chemical concentration, and the ability to use a Vernier effect to dramatically increase the sensors sensitivity.

In addition to the sensing applications of this work a more thorough understanding of the reflection and transmission properties of the surface relief grating is also presented. Implementation of the transfer matrix method for simulation of the gratings is also shown to be a fast and accurate modeling tool for predicting the grating response.

ACKNOWLEDGMENTS

First and foremost I must thank my beautiful wife, Marissa, who has stood patiently by my side during my graduate work and research for this dissertation. Her support and trust in me finishing this work has never wavered and her encouragement has helped me make it this far. My parents and parents-in-law have also been a great support to me and I have appreciated their interest in my progress and in this work.

I would also like to thank my graduate committee and in particular Dr. Schultz and Dr. Selfridge for their countless hours of collaboration. Their ideas, advice, and critiques have truly led to the success of this research. They have been excellent mentors and I am a better researcher, engineer, and scientist for having worked with them.

I am grateful to all the fellow researchers that have passed through the BYU Electro-Optics lab during my time here. I am grateful to Kevin Smith and Ben Ipson for helping to lay the foundation for this work. I am grateful to Brian Tebbs, Jonathan Young, and Greg Droge for their many hours of grating fabrication and packaging. I am grateful to Josh Kvavle, Rich Gibson, and Eric Johnson for their friendship, ideas, and discussion and especially to Josh for his many, many hours in front of the fusion splicer.

Finally, I am appreciative of Brigham Young University and the Department of Electrical and Computer Engineering for letting me be a student here for so many years. I would not have made it this far without their generous financial and academic support. KVH Industries, Inc. has been a major contributor to this research by generously donating the D-shaped optical fiber, the Office of the Secretary of Defense, Operational Test and Evaluation Directorate, and the American Society

for Nondestructive Testing have provided the majority of the financial support for this work.

Contents

List of Tables

List of Figures

Chapter 1

Introduction

Knowledge of how well a system or part of a system is performing is critical in any engineering application. The information gathered through sensing nodes and transducers is vital in order to optimize and increase reliability of these systems. As these engineering systems become more complicated, the necessity to detect and process many different variables becomes more important. Adequate sensors must be invented and fabricated that meet the ever increasing needs of the engineering community.

Many traditional sensors are based on mechanical or electrical properties to measure a given variable. While these types of sensors are suitable for many applications, optical based sensors provide an attractive alternative for situations in which a mechanical or electrical based sensor is not feasible. Some situations in which an optical solution should be considered are in environments with strong electromagnetic fields, in areas with high levels of nuclear radiation, in combustible environments, for 'in-vivo' measurements in medicine and biotechnology, and in situations that require distributed sensing of one or more variables [2].

Perhaps the most popular optical sensing solution is the optical fiber Bragg grating (FBG). The FBG reflects a specific wavelength of light that changes based on the surrounding conditions. The shift in the reflected light can be correlated back to a number of different environmental variables such as temperature, strain, or pressure.

While the FBG is an excellent optical sensor, it inherently has certain limitations that restrict its use in some applications. For example, FBGs can only operate in a fairly narrow temperature range of a few hundred degrees Celsius before

becoming unusable. Also, without modification to the optical fiber, FBGs can not sense material changes in the surrounding environment.

To overcome some of these limitations, but still take advantage of the many good qualities of FBGs, this dissertation investigates the use of D-fiber and a fabrication process to physically change the geometry of the fiber and create a surface relief grating. The major accomplishments of this dissertation show a dramatic increase in operating temperature to over 1000°C, the ability to measure multi-dimensional bend, the ability to measure material changes around the fiber such as chemical concentration, and the ability to use the Vernier effect to dramatically increase the sensors sensitivity. The surface relief fiber Bragg grating (SR-FBG) is shown to be a powerful step forward in optical sensing technology.

1.1 Optical Fibers and Optical Sensing

Optical fibers have played an invaluable role in creating the telecommunications infrastructure of the world today. High quality optical fiber has created a transmission line that experiences extremely low loss, has high damage thresholds, and exhibits low non-linear effects [3]. The transmission capabilities of optical fiber have popularized the bandwidth intensive applications of the Internet, cable, satellite, and cell phone industries to name a few. For many of the same reasons that optical fiber has found favor as a data transmission line, optical fiber has also made in roads into the sensing community as a viable alternative to more traditional sensing options.

Three general methods exist for creating optical sensing devices. The first method involves the use of bulk optical components such as lenses, mirrors, and gratings. A second method uses the integration of optical components into or onto a guiding medium of planar optical waveguides. The integration of optical devices onto planar substrates streamlines and simplifies the fabrication process, improves optical alignment, and allows for much more compact optical systems. These advantages mirror those of integrated electronic circuits.

Devices created with bulk or integrated optical components do not interface well with single-mode fibers which form the backbone of optical systems. The difficultly of integrating the system with the optical fiber leads to high insertion loss, power reflection, and poor mechanical integrity. While the integration of optical components onto planar waveguides overcomes many of these problems, planar waveguides still suffer from the difficulty of pigtailing optical fibers to them.

To overcome these difficulties, the sensor itself can be fabricated into or onto the optical fiber eliminating the need for pigtailing or coupling. Optical fiber sensors also offer many advantages because they are light weight, immune to electromagnetic interference, and are generally quite flexible. They are easily multiplexed and many sensors can be fabricated on a single fiber. These sensors can be used to monitor environmental variables such as temperature, strain, pressure, and the presence or absence of chemicals.

Even with these advantages, the regular use of optical sensors in industry based platforms has been a slow process based on a market that already accepts electro-mechanical sensors for reliability and low manufacturing costs [2]. Optical fibers also have the disadvantage of requiring transmission and receiving equipment that can be costly. However, as research continues to improve optical sensing technology their advantages are continually magnified while the drawbacks diminish.

1.2 Contributions

This work extends prior work in which SR-FBGs are first presented [4]. The previous work provides the initial theoretical understanding of SR-FBGs and provides an initial fabrication technique. This dissertation refines the initial work by creating a reliable fabrication process that minimizes device failure. Also, adaptation of the transfer matrix method for grating simulation creates a powerful, fast, and accurate means to model many different and complex SR-FBG structures.

This dissertation also explores the use of SR-FBGs for many different sensing applications. A fully packaged sensor suitable for high temperature operation and industry testing is presented. Characterization of the temporal thermal response

shows that the SR-FBG responds quickly enough for many 'real-time' measurements. Other sensing applications that are presented are a volatile organic compound sensor and a multi-dimensional bend sensor. The work concludes by presenting a non-uniform grating structure that creates multiple peaks in the reflection or transmission spectra. These multiple peaks can be used to create a Vernier effect and a whole new class of sensors is envisioned.

The research contained in this dissertation has directly lead to seven peer-reviewed journal publications, ten conference papers and/or talks, and one provisional patent. In summary the main contributions of this work are as follows:

- Refining of the fabrication process for SR-FBG such that photoresist adhesion to the optical fiber is greatly increased.
- Discovering the importance of not fabricating the grating on the transition regions of etch to unetched fiber in order to maintain a symmetric reflection spectrum.
- Adding a pre-exposure step to the fabrication process in order to predefine the grating region.
- Adapting the transfer matrix method to SR-FBG simulation in order to quickly and accurately model complicated grating structures.
- Explaining the polarization dependence of SR-FBG through experimental and theoretical techniques.
- Fabricating SR-FBGs using rotated core D-fiber to minimize the polarization dependence.
- Creating a fully packaged high temperature sensor that has collected real data from industry field tests.
- Demonstrating the temporal thermal response of the SR-FBG at high temperatures.

- Integrating a chemical sensing material (PDMS) with the SR-FBG to create a volatile organic compound chemical sensor.
- Using the SR-FBG as a multi-dimensional bend sensor.
- Showing theoretically that structured SR-FBGs can use the Vernier effect to greatly increase a sensors sensitivity.
- Fabricating structured SR-FBGs using a simple mask technique created from a laser printer.

1.3 Dissertation Outline

The remainder of this work is outlined as follows. Chapter 2 presents the background and a foundational layer for themes and concepts that are prevalent throughout this work. Background is given on optical D-fiber and FBG transmission and reflection properties. Chapter 3 goes through the fabrication process for SR-FBGs and discusses their spectral properties such as cladding and polarization modes. Chapter 4 investigates the polarization dependence of SR-FBG and shows both theoretically and experimentally that the polarization dependence is due to the asymmetric waveguide structure. Chapter 5 presents the SR-FBG as a high temperature sensor that is able to operate in environments that exceed 1000°C while Chapter 6 discusses the temporal thermal response of the high temperature sensor. Chapter 7 shows how the SR-FBG along with an additional sensing layer can be used to create a volatile organic compound chemical sensor. Chapter 8 presents a multi-dimensional bend sensor using the SR-FBG that can track bend in both the vertical and horizontal directions. Chapter 9 shows that the SR-FBG can be fabricated to create multiple peaks in the reflection or transmission spectra that are suitable for Vernier sensing applications. Using the Vernier effect, these sensors are theoretically shown to increase sensitivity by at least two orders of magnitude. Chapter 10 concludes by summarizing the major accomplishments and contributions of this work. Appendices are also provided to give a step-by-step fabrication process, an explanation of the

computer code used for simulation, and a Fourier analysis of the super structured gratings.

Chapter 2

FBG and D-fiber Background

This chapter provides the foundational layer needed to better understand the work for this dissertation. Although this chapter is dedicated to the necessary background, detailed derivations and detailed theory are intentionally left for the specific applications of each of the proceeding chapters. Rather a general overview of the main components and ideas that are used throughout this work are reviewed.

The three critical ideas which are reviewed in this chapter are: (1) fiber Bragg gratings (FBGs) offer the necessary reflection and transmission properties for many optical sensing schemes, (2) D-shaped optical fiber (D-fiber) provides an excellent platform on which to fabricate sensing devices, and (3) the transfer matrix method is a valid numerical method to model the reflection and transmission properties of both FBGs and surface relief FBGs.

2.1 Fiber Bragg Gratings

The most important concept used throughout this work is that fiber Bragg gratings (FBGs) provide the necessary transmission and reflection properties for sensing applications. A Bragg reflection occurs in an optical fiber when the forward propagating light satisfies the Bragg condition when incident upon a periodic modulation in the refractive index. This phenomenon is well known in the study of crystal lattices where X-rays are reflected at well defined angles due to the periodic arrangement of the atoms [5]. The reflections are described by the Bragg equation as

$$\lambda_b = 2n_{eff}\Lambda \tag{2.1}$$

where λ_b is the wavelength of peak reflection and is known as the Bragg wavelength, n_{eff} is the effective index of the guided mode in the optical fiber, and Λ is the period of the index modulation known as the grating period or the grating pitch.

The FBG has become one of the most useful and well known optical fiber sensors. Dr. Kenneth Hill and George Meltz from the Canadian Communication Research Centre first investigated FBGs in 1978 as high-quality, long-length reflection filters for distributed feedback systems [6]. Their work demonstrated that optical fibers with a photosensitive mechanism in the core, found in Germanium doped fibers, could be used to create a Bragg reflection grating. Since that time, researchers in the field of fiber optics have investigated the use of FBGs for sensing applications.

FBGs can be used in many sensing applications because there are many variables that change either the period or the effective index of the optical FBG. As the temperature, strain, or other environmental variable changes, the reflected Bragg wavelength also changes. The desired information is extrapolated from the corresponding reflected wavelength shift. For example, an increase in temperature causes the Bragg wavelength to change for two reasons. First, thermal expansion causes the period of the Bragg grating to increase, and secondly an increase in temperature changes the indices of refraction of the fiber materials thus altering the effective indices of the modes in the fiber. As these properties of the fiber change, the peak reflected wavelength shifts and can be characterized for the change in temperature.

One of the main advantages in using FBGs in sensing applications is the ease with which multiple sensors can be multiplexed onto a single line. Figure 2.1 shows an illustration of an optical fiber with multiple FBGs. Creating multiple FBGs each with a different grating period allows for distributed sensing as each sensor shifts around it's central Bragg wavelength. Also because there is no coupling between the individual FBGs the sensors can be placed closed together or far apart depending on the application need [4].

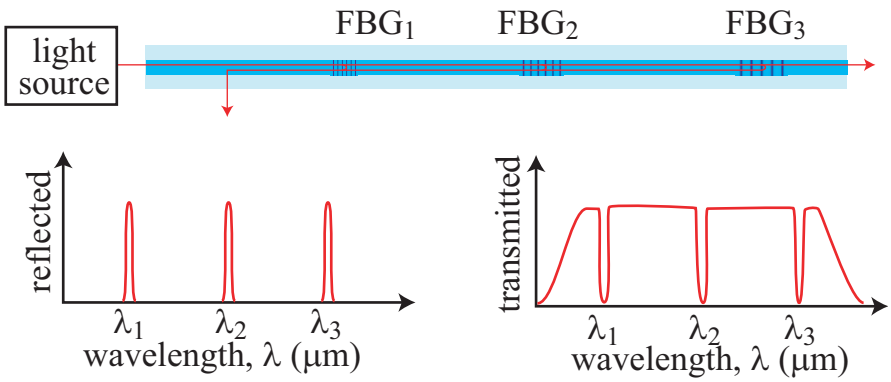

Figure 2.1: Drawing of multiple FBGs distributed on a single optical fiber. Each grating is fabricated with a specific grating period and thus reflects at a specific wavelength.

2.1.1 UV Written FBGs vs. Surface Relief FBGs

Traditional FBG sensors are fabricated by exposing optical fibers to an ultraviolet (UV) interference pattern [7]. Exposing the fiber to UV light affects the photosensitivity of the core and thus changes the refractive index. When used in conjunction with a periodic pattern, either created from interference or from a mask, a periodic refractive index change is written into the core.

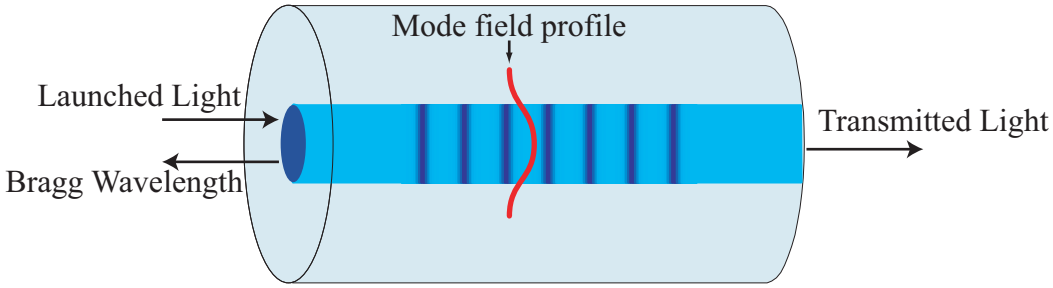

Figure 2.2: Diagram showing the periodic modulation written into the core of an optical fiber.

Figure 2.2 is a representation of what a traditional FBG might look like. The grating reflects light at the Bragg wavelength while light of all other wavelengths

pass through the fiber. The reflectivity of a FBG depends on the length of the grating, the amplitude of the periodic index modulation, and the amount of overlap between the grating and the field of the guided mode in the fiber. This overlap is quantified as the fraction of the modal field profile that falls in the physical area where the index modulation occurs. In these standard FBGs, UV exposure changes the refractive index of the core by a small amount, usually from 10^{-5} to 10^{-3} of the pre-exposure refractive index [6], however, the modulation occurs over the entire cross-section of the fiber core, thus creating a large overlap between the grating and the field of the guided mode. This large overlap means that at the specified Bragg wavelength and with a sufficiently long grating, reflectivity of nearly 100% can be achieved.

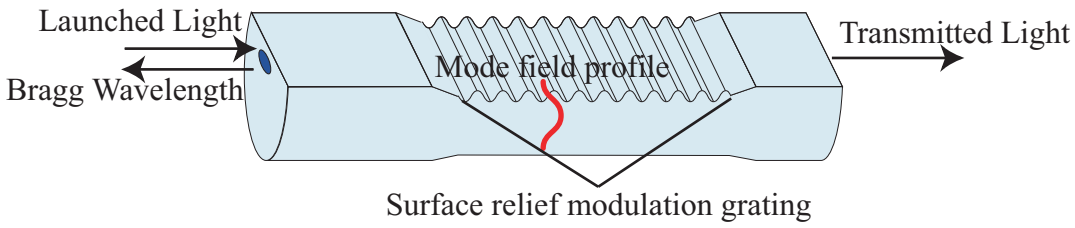

Figure 2.3: Diagram showing the periodic modulation written on the surface of a D-fiber.

As an alternative to the more common fabrication methods, this work investigates the use of D-fiber and a fabrication process to physically change the geometry of the fiber and create a surface relief grating. Using D-fiber, Figure 2.3 is a drawing of a surface relief fiber Bragg grating (SR-FBG) showing that the periodic modulation occurs on the surface of the fiber as opposed to inside the core. Chapter 3 describes the fabrication of such a grating. Because the grating is on the surface of the D-fiber above the fiber core the overlap with the guided mode is minimal. However, because of the large index modulation between the index of the cladding and the index of air, reflectivity of nearly 100% can also be achieved using SR-FBGs created with D-fiber.

2.2 D-shaped Optical Fiber

The two primary features of D-fiber are the elliptical core, which maintains polarization, and the proximity of the fiber core to the flat surface. This proximity allows access to light in the core by removal of the cladding above the core. Etching the fiber such that some of the cladding above the core remains allows for the creation of devices in which the evanescent field of the light guided in the fiber interacts with materials and/or structures on the flat side of the fiber. The D shape of the fiber gives the device mechanical integrity, and approximately the same dimensions of the fiber are preserved after the small cladding removal. Other research is done on circular fibers that are etched close to the core; however, the fiber dimensions are changed dramatically by the etching process [8].

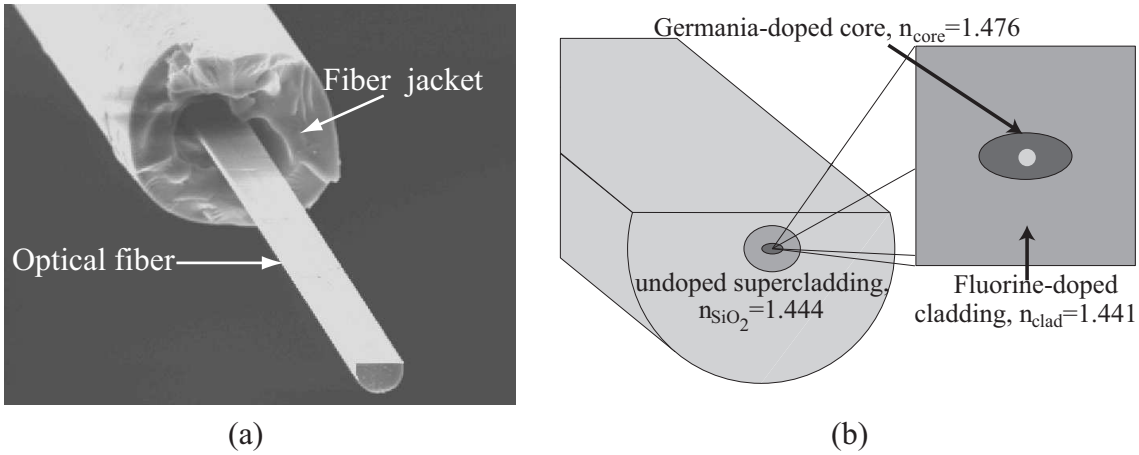

Figure 2.4: (a) Scanning electron micrograph (SEM) and (b) cross section image of a D-fiber. The numerical aperture is 0.32 and the cutoff wavelength is 1230±130 nm.

Figure 2.4(a) shows a scanning electron micrograph (SEM) of a D-fiber and Fig. 2.4(b) illustrates the fibers cross section. KVH Industries, Inc., generously supplies the fiber for this research. The D-fiber is composed of silica with a germania-doped core surrounded by a flourine-doped cladding, which is surrounded by a pure silica supercladding. The diameter of the fiber is approximately 125 μm and the fiber core is approximately 13 μm from the flat surface of the fiber. The core is elliptical

with a major axis of about 4 μm and a minor axis of about 2 μm. The major axis of the elliptical core can be manufactured such that it is parallel to the flat surface of the fiber (horizontal core fiber). The major axis can also be manufactured such that it is perpendicular to the flat of the fiber (vertical core fiber) and rotated away from the flat surface of the fiber (rotated core fiber). In the preform fabrication process, germania diffuses out from the center of the core, leaving a region of undoped silica in the center of the core known as the vapor spot [4].

For the majority of this work only horizontal core fiber is used in the fabrication process. Because the core of the fiber is elliptical the fiber is said to be polarization maintaining and supports two polarization states. This work adopts the convention that when the major component of the electric field is polarized parallel to the flat surface of the fiber then the mode is said to be horizontally polarized. When the major component of the electric field is polarized perpendicular to the flat surface of the fiber then the mode is said to be vertically polarized. Deviation from this convention only occurs in Ch. 4 where the polarization dependence of the gratings is discussed.

While the flat surface of the D-fiber provides a planar surface on which to fabricate devices, the asymmetric shape also creates fabrication and usability difficulties. One challenge arises while trying to keep the fiber flat side up throughout the entire fabrication process. Another challenge arises due to the non-standard cladding shape and smaller than normal core size. The cladding shape and the core size make it more difficult to couple light into the optical fiber. These two problems are specifically addressed in Ch. 3 when the fabrication process is discussed.

2.3 Analysis of FBGs Using Coupled Mode Equations

SR-FBGs may be used in many of the same applications as commercial FBGs but offer additional advantages such as high temperature operation, multi-dimensional bend sensing, and chemical sensing that are discussed in the remainder of this work. Analysis of the transmission and reflection properties of SR-FBGs is nearly the same as the analysis would be for a FBG written in the core of a fiber.

In order to understand the reflection and transmission properties of a FBG, one must analyze how the forward traveling mode is coupled into a reverse traveling mode as it propagates in the optical fiber. This analysis can best be achieved by employing what is known as coupled-mode theory. Other techniques are available for analyzing a perturbed waveguide, however, coupled-mode theory is somewhat straightforward, intuitive, and it accurately models the optical properties of most fiber gratings [9]. In this section a derivation of coupled-mode theory is not presented, but it can be found in many textbooks [10]. Rather the results are given and explanation of how to use the results to better understand FBGs is provided.

In an ideal waveguide the propagating modes are orthogonal and do not exhibit an exchange in energy. However, when a dielectric or other perturbation is present the modes are coupled such that the amplitudes of two modes are related by the following equations,

$$\begin{aligned}
\pm\frac{d}{dz}a_\mu(z) =& -j\sum_\nu \kappa_{\mu\nu}(z)a_\nu(z)e^{-j(\beta_\nu-\beta_\mu)z},\\
\kappa_{\mu\nu}(z) =& \quad \kappa^t_{\mu\nu}(z)+\kappa^z_{\mu\nu}(z),\\
\kappa^t_{\mu\nu}(z) =& \quad \frac{\omega\epsilon_0}{4}\int\int \Delta\epsilon_r(x,y,z)\mathbf{E}^*_{t\mu}(x,y)\cdot\mathbf{E}_{t\nu}(x,y)\mathrm{d}x\mathrm{d}y,\\
\kappa^z_{\mu\nu}(z) =& \quad \frac{\omega\epsilon_0}{4}\int\int \frac{\epsilon_r\Delta\epsilon_r(x,y,z)}{\epsilon_r+\Delta\epsilon_r(x,y,z)}\mathbf{E}^*_{z\mu}(x,y)\cdot\mathbf{E}_{z\nu}(x,y)\mathrm{d}x\mathrm{d}y.
\end{aligned} \tag{2.2}$$

In these equations κ^t and κ^z are respectively the coupling coefficients due to the transverse, $\mathbf{E_t}$, and longitudinal, $\mathbf{E_z}$, fields. They describe how strongly power from the ν^{th} mode is coupled into the μ^{th} mode. Generally speaking $\kappa^z << \kappa^t$ and is usually neglected for fiber modes [9]. In these equations β is the propagation constant, ϵ_r is the relative permittivity, and a is the amplitude of the mode.

For Bragg reflection to occur the grating is designed such that the fundamental forward propagating mode is coupled into the fundamental reverse propagating mode. Near the wavelength for which this occurs, coupling into other modes is negligible thus allowing a simplification of Eq. (2.2). The coupling coefficient is the same for all pairs of modes, i.e. $\kappa_{ff} = \kappa_{rr} = \kappa_{fr} = \kappa_{rf}$, where f and r label the forward- and reverse-traveling modes respectively. Therefore it is possible to write

the coupled-mode equations as

$$\begin{aligned}\frac{d}{dz}a_f(z) =& -j\kappa(z)\big(a_f(z) + a_r(z)e^{j2\beta z}\big),\\ \frac{d}{dz}a_r(z) =& +j\kappa(z)\big(a_r(z) + a_f(z)e^{-j2\beta z}\big),\\ \kappa(z) =& \quad\frac{\omega\epsilon_0}{4}\int\int \Delta\epsilon_r(x,y,z)|\mathbf{E}_{t\mu}(x,y)|^2\mathrm{d}x\mathrm{d}y.\end{aligned} \tag{2.3}$$

While these equations may not look straightforward, they do give great insight into how the modes are dependent upon each other. The effects of the grating are taken into account when calculating $\kappa(z)$ where $\Delta\epsilon_r$ represents the perturbation to the permittivity. Because $\kappa(z)$ greatly complicates the work, these equations are usually solved numerically instead of analytically [4].

2.4 Properties of Uniform FBGs

One instance where the coupled mode equations can be solved analytically is when the FBG is said to be uniform. Figure 2.5 shows a diagram of the refractive index profile for a uniform FBG. A uniform FBG is defined as a grating that has a homogeneous index modulation amplitude and a constant grating period along the entire length of the grating. If this is the case then the coupling coefficient, κ, is constant and Eq. 2.3 simplifies into coupled first-order differential equations with constant coefficients. By assuming appropriate boundary conditions a closed form solution is found.

The periodic index modulation is assumed to begin at $z = 0$ and end at $z = L$. The forward traveling mode $a_f(0) = 1$ and the reverse traveling mode $a_r(L) = 0$. With these assumed boundary conditions, the solutions to Eq. 2.3 are

$$\begin{aligned}a_f(z) =& a_f(0)\frac{\alpha\cosh(\alpha(L-z)) - i\delta\sinh(\alpha(L-z))}{\alpha\cosh(\alpha L) - i\delta\sinh(\alpha L)},\\ a_r(z) =& ia_f(0)\frac{\kappa\sinh(\alpha(L-z))}{\alpha\cosh(\alpha L) - i\delta\sinh(\alpha L)},\end{aligned} \tag{2.4}$$

where $\alpha = \sqrt{\kappa^2 - \delta^2}$ and $\delta = 2\pi n_{eff}\left[\frac{1}{\lambda} - \frac{1}{\lambda_B}\right]$ is known as the detuning parameter. The reflectivity and the transmissivity of the grating as a function of the detuning

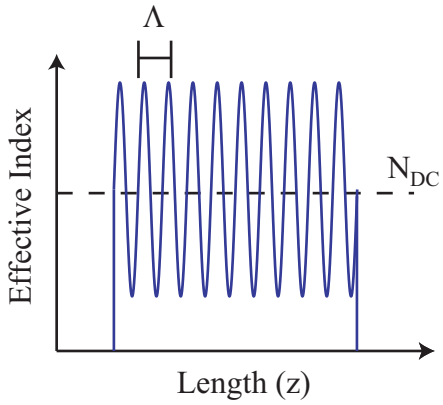

Figure 2.5: Diagram showing the refractive index profile for a uniform FBG. The grating is homogeneous in index modulation amplitude with a constant grating period.

are given as

$$\begin{aligned} r &= \frac{a_r(0)}{a_f(0)} = \frac{i\kappa \sinh(\alpha L)}{\alpha \cosh(\alpha L) - i\delta \sinh(\alpha L)}, \\ t &= \frac{a_f(L)}{a_f(0)} = \frac{\alpha}{\alpha \cosh(\alpha L) - i\delta \sinh(\alpha L)}. \end{aligned} \tag{2.5}$$

The reflectance of the grating is defined as $R = |r^2|$ and is therefore given as

$$R = \frac{\kappa^2 \sinh^2(\alpha L)}{\alpha^2 \cosh^2(\alpha L) + \delta^2 \sinh^2(\alpha L)}. \tag{2.6}$$

The maximum reflectance occurs at the Bragg wavelength λ_B. At the Bragg wavelength the detuning parameter, δ, is equal to zero and therefore the maximum reflectance of a uniform FBG is found to be

$$R_{max} = \tanh^2(\kappa L). \tag{2.7}$$

Figure 2.6 shows three reflection spectra with three different coupling strengths. By increasing the coupling strength both the maximum reflectance increases and the grating bandwidth increases. For weak gratings, where the periodic index modulation is small, the bandwidth is limited by the physical length of the grating. For strong gratings, where the periodic index modulation is large, the bandwidth becomes independent of the physical grating length. The bandwidth is length independent because for strong gratings the light does not penetrate the full distance of

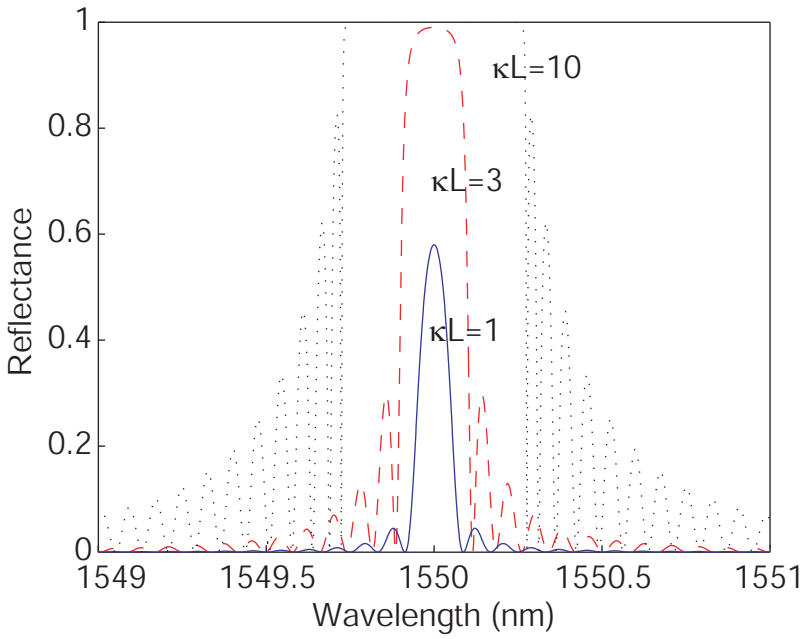

Figure 2.6: Graph showing three different reflection spectra for three different coupling strengths.

the grating before nearly 100% is reflected. For these strong gratings the bandwidth is directly proportional to the index of refraction change [6].

The sidelobes of Fig. 2.6 are produced from a Fabry-Pérot effect at the input and output of the grating [11]. The step changes in the index of refraction at the input and output to the grating form a cavity in the same way that two discrete mirrors form a Fabry-Pérot. If necessary, these sidelobes can be minimized by apodizing the index profile similar to the way antenna pattern sidelobes are minimized in RF theory.

The uniform FBG is the elementary building block upon which most of the sensors in this work are realized. Because of its importance the following list gives a summary of the properties and principles of uniform FBGs.

- The peak reflectivity occurs at the Bragg wavelength i.e. when $\delta = 0$.
- When $\delta = 0$ the maximum reflectance is given by Eq. 2.7.
- For weak gratings the bandwidth of the reflection peak is length limited.

- For strong gratings saturation of the reflectivity occurs before the light has propagated the total grating length. The reflection bandwidth is no longer limited by the length but is instead directly proportional to the index of refraction change.

- As the grating increases in strength so do the relative reflectivities of the side lobes.

2.5 Modeling Fiber Bragg Gratings

Many different techniques have been developed to use computers in the simulation of different FBG structures. Computer simulation is an invaluable tool which allows the designer to gain insight into the reflection and transmission properties of many different FBGs. Perhaps the most obvious method would be the direct numerical integration of the coupled-mode equations. Direct numerical integration of the coupled-mode equations allows for almost complete control of the coupling coefficient along the propagation direction, however, this method can be extremely slow depending on the integration step size [3].

Other methods based on inverse scattering [12], Fourier transforms [13], and thin films [14] have also been developed. While each of these methods offer their own advantages, the major disadvantage of each is the time and computing resources needed to accurately complete the simulation.

A very fast computational method for grating simulation is known as the transfer matrix method [15]. The transfer matrix method models the grating as multiple, small, uniform grating sections. A transfer matrix is created for each discrete grating section and all the transfer matrices are sequentially multiplied together to find the full grating response. Because each discrete grating section is assumed to be uniform, the matrix for each section is comprised of the closed form solution of the coupled-mode equations for a uniform FBG of the previous section. Utilization of a closed form solution eliminates the need for computationally intensive numerical integration.

The major advantage of the transfer matrix method is the speed with which a reflection or transmission spectrum can be calculated. Another advantage of this method is that complicated, non-uniform grating structures can be easily modeled by using a discrete piecewise approach. The major disadvantage of the transfer matrix method is the loss of accuracy that can occur due to the discretization along the grating length. In order for the method to remain valid each discrete grating section should be much longer than the grating period [6]. This limitation can become a problem if the grating period or index of refraction varies rapidly on the order of the grating period. However, in most situations these variables do not vary so rapidly and the transfer matrix method remains valid.

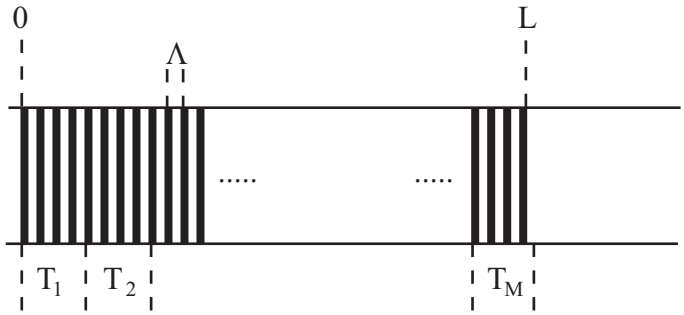

Figure 2.7: Illustration of the key components of the transfer matrix method.

Figure 2.7 shows an illustration of the key components to the transfer matrix method. Over each discrete grating section the transfer matrix is dependent on the local coupling coefficient, the local grating period, the local mode effective index, and the local change in effective index. The transfer matrix for each individual section, T_m, is given as

$$T_m = \begin{bmatrix} \cosh(\alpha dz) - i\frac{\delta}{\alpha}\sinh(\alpha dz) & -i\frac{\kappa}{\alpha}\sinh(\alpha dz) \\ i\frac{\kappa}{\alpha}\sinh(\alpha dz) & \cosh(\alpha dz) + i\frac{\delta}{\alpha}\sinh(\alpha dz) \end{bmatrix}, \tag{2.8}$$

where dz is the length of each discrete grating section and the remainder of the variables have been defined previously.

To find the full grating response each individual grating section is multiplied together such that

$$\begin{bmatrix} a_f(M) \\ a_r(M) \end{bmatrix} = T_M T_{M-1} ... T_2 T_1 \begin{bmatrix} a_f(0) \\ a_r(0) \end{bmatrix}. \tag{2.9}$$

The initial conditions for the simulation are $a_f(0) = 1$ and $a_r(0) = 0$. The grating reflectivity and the grating transmissivity are given in Eq. 2.5. In terms of the transfer matrix components, the grating reflectivity is

$$r = \frac{T_{21}}{T_{11}}, \tag{2.10}$$

and the grating transmissivity is given as

$$t = \frac{1}{T_{11}}. \tag{2.11}$$

Appendix B is dedicated to an explanation of the actual code used to implement the transfer matrix method and gives specific examples of how to use the model to simulate uniform, chirped, apodized and structured gratings. The method works well for modeling both traditional UV written gratings and the surface-relief gratings of this work. As long as the coupling coefficient is accurately calculated then the actual grating type does not matter. Smith has shown that BeamPROP, a commercially available software package, can be used to accurately calculate the coupling coefficient by numerically solving for the overlap of a surface relief grating with the guided mode of the D-fiber [4].

To compare the transfer matrix method with direct numerical integration of the coupled mode equations for SR-FBGs, Figure 2.8 shows a graph of the grating efficiency versus core-to-flat distance for the two different numerical methods. In the simulations the grating length is 1.5 cm, the grating depth is fixed at 100 nm, and both horizontal and vertical core D-fiber is used with horizontally polarized light. The results are nearly identical indicating that the transfer matrix method is a valid, computationally fast simulation tool for SR-FBGs.

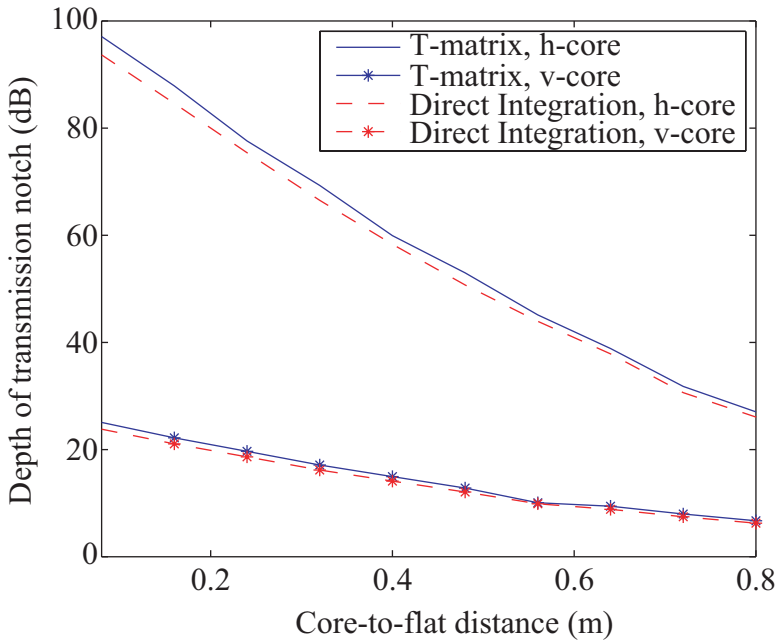

Figure 2.8: Comparison of the SR-FBG efficiency when computed by direct numerical integration and using the transfer matrix method.

2.6 Measuring the Reflection and Transmission Spectra of FBGs

The reflectance is often referred to as the efficiency of the grating. Measurements in both the reflection and transmission regimes allows for a better understanding of how well the grating performs. In reflection it is easy to see very weak gratings as the Bragg reflected signal is often well above the noise floor of the measuring equipment. In transmission, the actual grating reflectance is most easily measured because knowledge of the total transmitted power is well known.

Figure 2.9 shows a diagram of a possible setup that may be used to measure both the reflected and transmitted signal from a FBG. First broadband light is launched into a 50:50 coupler. One leg of the coupler is connected to the FBG that is under test. On the other leg, opposite the FBG, is an optical spectrum analyzer (OSA) that is used to display the reflected signal. The transmitted signal can also be measured by connecting the OSA to the free end of the FBG. All of the ends of the fiber that are not connected should be immersed in index matching oil in order to minimize the effects of back reflections.

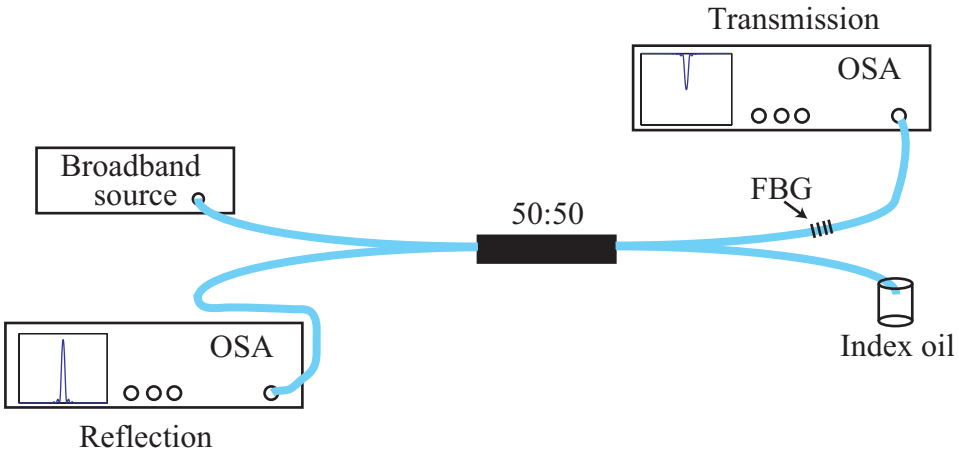

Figure 2.9: Diagram showing a possible setup to measure the transmission and reflection spectra with an OSA.

FBG interrogators are another popular measurement device used to capture the reflection or transmission spectrum. These interrogators use a tunable source and a detector to reproduce the optical spectrum. Figure 2.10(a) shows a diagram of how to properly connect a FBG to an interrogator. Again if only the reflection spectrum is being measured then the free end of the FBG should be immersed in index oil or crushed in order to minimize back reflections. In order to measure the FBG in transmission with the interrogator then two channels must be used with an optical isolator on one channel. Figure 2.10(b) shows how to connect the FBG to the interrogator for a transmission measurement.

The maximum reflectance from a FBG can be calculated by measuring the dip, T_d, in the transmission spectrum in dBs. From the measured dip the reflectance is calculated as

$$R = 1 - 10^{\frac{-T_d}{10}}. \tag{2.12}$$

The maximum reflectance can also be calculated by the peak in the reflected signal, R_p, below that of the transmitted signal in dBs. Knowledge of the transmitted signal is sometimes complicated in reflection due to coupling losses, connector losses, and radiation losses that might occur. From the measured peak the reflectance is

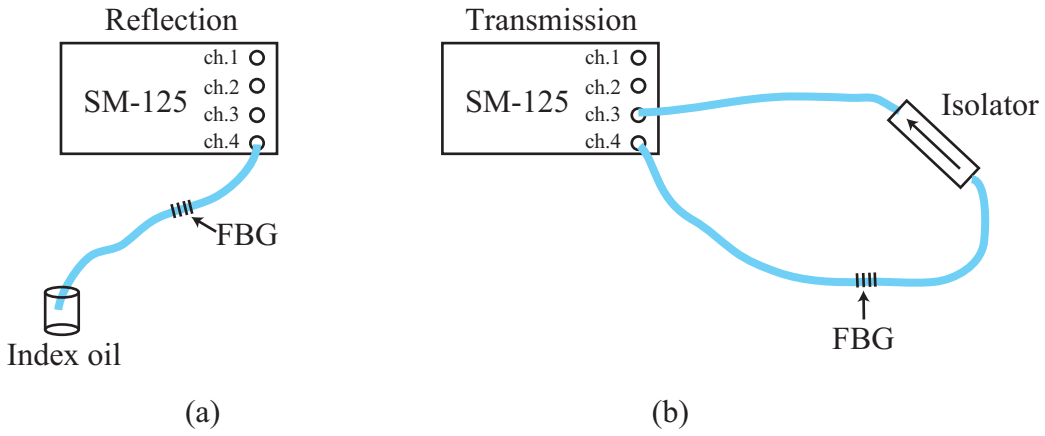

Figure 2.10: Diagram showing how to measure a FBG in (a) reflection and (b) transmission with a SM-125 optical interrogator.

calculated as

$$R = 10^{\frac{-R_p}{10}}. \tag{2.13}$$

Figure 2.11 illustrates a reflection and a transmission spectrum with the proper distance to measure for T_d and R_p. For this particular grating $R_p = 4.37$ dB and $T_d = 1.97$ dB meaning that the maximum reflectance is 0.36.

2.7 Summary

This chapter reviews the three essential ideas for the success of this work. The first is that optical D-fiber provides an excellent platform on which to fabricate optical sensors. Due to the close proximity of the core with the flat surface of the fiber, a short etch allows access to the light in the core while maintaining the mechanical integrity of the fiber. Once the fiber has been etched many different devices can be fabricated on the flat surface in the evanescent region of the propagating mode. The second idea is that fiber Bragg gratings offer the necessary reflection and transmission properties for many sensing applications. Lastly, this chapter reviews the transfer matrix method and shows that it is a fast and accurate method for modeling both FBGs and SR-FBGs. This chapter lays the foundation for the rest of this work on which more complicated principles and specific sensing applications build on.

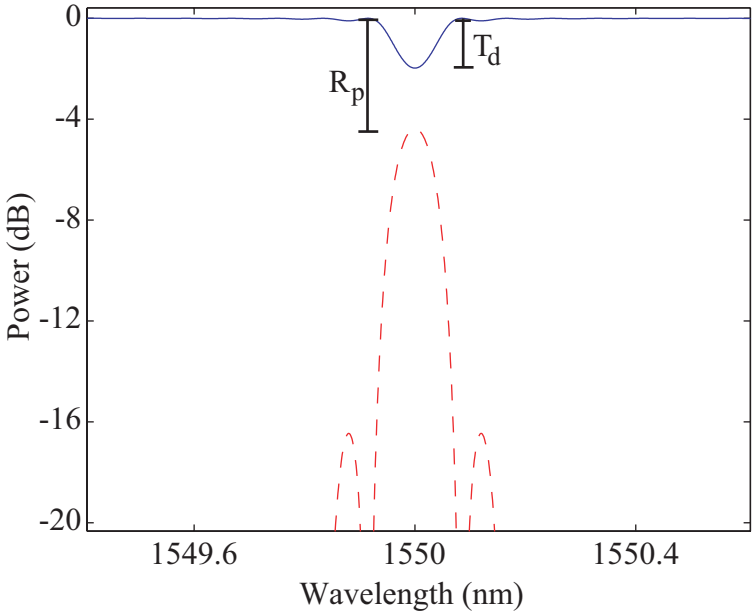

Figure 2.11: Graph showing a reflection (dashed) and transmission (solid) spectrum for the same grating in dB.

Chapter 3

General Fabrication Process

All though the fabrication process varies slightly for each individual sensing application, this chapter is dedicated as an overview of the most basic and foundational fabrication steps. The steps that are explained are the basis on which SR-FBG fabrication is possible. In the proceeding chapters any deviation from these steps or additional steps due to specific sensor fabrication are so noted.

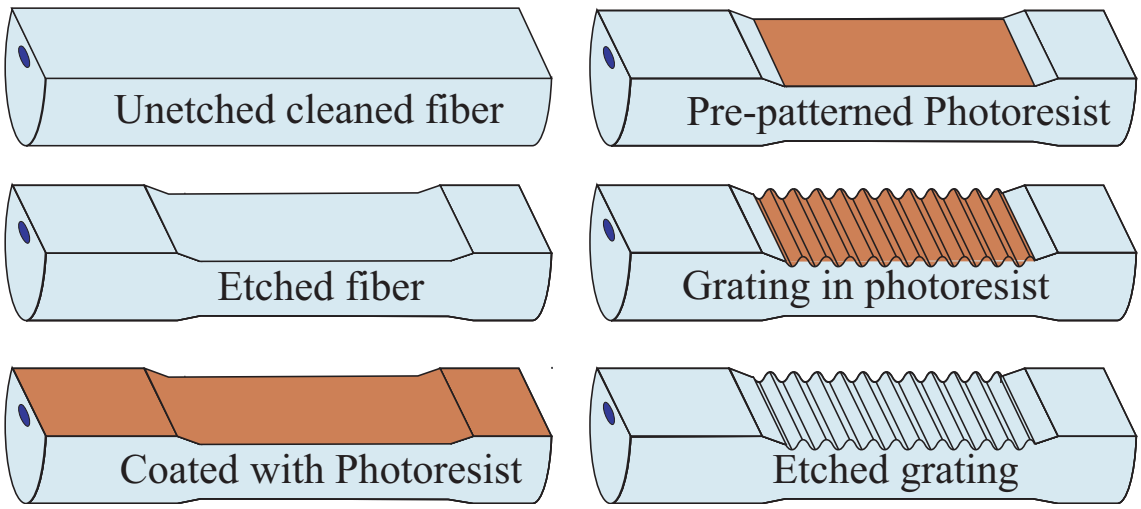

Figure 3.1: Six basic steps to SR-FBG fabrication.

Figure 3.1 shows that the fabrication of SR-FBGs consists of six main steps. (1) The D-fiber is thoroughly cleaned in preparation for wet etching. (2) The fiber is placed in a bath of hydrofluoric acid to etch down the cladding layer above the core. (3) The fiber is coated with photoresist, and (4) is pre-exposed in order to

eliminate any photoresist on the transitions from etched to unetched fiber. (5) The fiber is exposed to a two beam interference pattern, and lastly (6) the grating pattern is transferred into the glass fiber by using a reactive ion etcher (RIE). A step-by-step procedure is given in Appendix A.

In the remainder of this chapter each of these six steps are examined and explained in detail. When necessary, sufficient theory is also provided in order to better understand the reasoning behind the specific fabrication step. Theory is also given to show which design variables can be changed and what the possible outcome of such changes might be.

3.1 Initial Cleaning of the D-fiber

Throughout the entire fabrication process cleanliness of the fiber is paramount in order to produce a successful grating. Because cleanliness is so important, great care is taken during this first step to ensure that any dust particles, films, or jacket fragments are completely removed before the wet etching process.

The first step is to remove $\sim$2-3 cm of the protective polymer jacket from the section of the fiber that will be etched. The jacket removal can be done by using a mechanical stripper, a heat stripper, a solvent such as dichloromethane, or acid such as sulfuric acid. All four methods can be used and yield successful gratings. Several articles are written on the mechanical integrity of an optical fiber after stripping and the advantages and disadvantages to each method [16, 17, 18]. Throughout this work, most of the fibers are stripped using a heat stripper for convenience and ease of use.

Once the jacket is removed the fiber is placed in the etch holder flat side up. Even though the jacket strippers work well, they all leave behind jacket fragments that need to be removed. To remove these jacket fragments the fiber is placed in a bath of isopropyl alcohol (IPA) in an ultrasonic cleaner. The IPA and ultrasonic cleaner work together to remove any remaining jacket fragments.

As a final cleaning step, the fiber is allowed to soak in a bath of DeContam for more than five minutes. DeContam is a cleansing agent used to remove any

contamination and film that is left on the fiber after the IPA bath. After soaking the fiber, the DeContam is rinsed off using de-ionized (DI) water.

3.2 Hydrofluoric Acid Etching

In order to use SR-FBGs as effective sensors, gratings must be etched into the surface of the glass fiber very close to the fiber core. The fiber core is approximately 13 μm from the flat surface of the fiber necessitating the removal of the cladding above the core to improve the mode overlap with the grating. This cladding removal is accomplished by placing the fiber in a bath of 25% by volume hydrofluoric acid (HF). In-situ monitoring of the birefringence between the two polarizations (along the major and minor axis) in the fiber allows for a controlled etch that is terminated when a predetermined amount of cladding is left above the core [19].

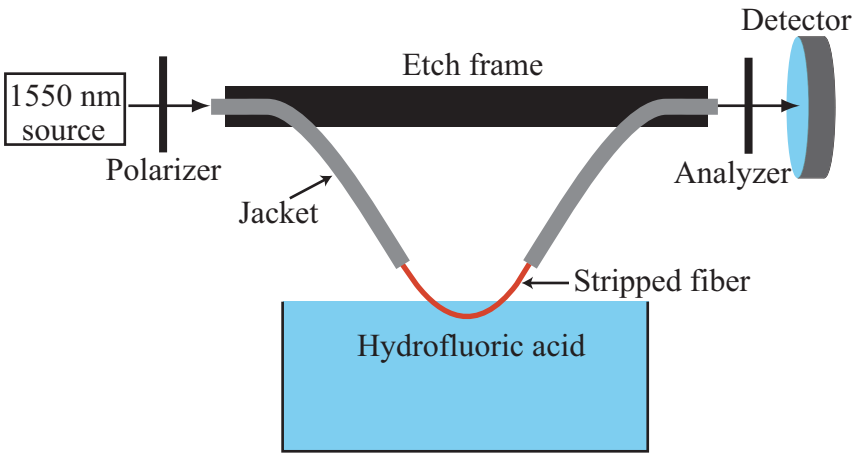

Figure 3.2: Setup to monitor the birefringence of the fiber as it is etched, with a polarizer at the input and an analyzer at the output

Figure 3.2 shows the etch setup used to monitor the etch. A Teflon etch frame holds the fiber so that a 2.0 cm section of the fiber is immersed in HF. 1550 nm light is launched into the fiber through a polarizer at a 45° angle relative to the major axis of the elliptical core of the fiber. Launching the light at this angle allows equal amounts of light to be coupled into each of the two polarization modes. One

mode is polarized along the major axis of the ellipse, and the other along the minor axis. An analyzer is placed at the output of the fiber, at a -45° angle with respect to the major axis of the ellipse, and a detector measures the transmitted power.

3.2.1 Theory of In-Situ Etching

To better understand the etching process, it is useful to go through the mathematical details of changes to the light as it propagates through the fiber and as the fiber cladding layer is etched away. Since the core of the fiber is elliptical it supports two orthogonal modes that are aligned with the major and minor axes of the core. Therefore, the light can be thought of as the sum of two orthogonally polarized electric fields. For example, the time-dependent E-field as a function of the propagating distance, z, in the fiber after being launched through a linear polarizer oriented at an angle θ_p away from the major axis of the core is given as,

$$\mathbf{E}(t,z) = E_0 \cos\theta_p \cos(wt - \beta_z^x z - \phi_x)\hat{\mathbf{x}} + E_0 \sin\theta_p \cos(wt - \beta_z^y z - \phi_y)\hat{\mathbf{y}}, \tag{3.1}$$

where ϕ_x and ϕ_y are some initial phase. The different propagation constants, β_z^x and β_z^y correspond to the light polarized along the horizontal (along the major axis of the core) and the vertical (along the minor axis of the core) axes of the core. These two polarizations are the two orthogonal modes. The propagation constants are,

$$\beta_z^x = \frac{2\pi}{\lambda_0} n_x, \tag{3.2}$$

$$\beta_z^y = \frac{2\pi}{\lambda_0} n_y, \tag{3.3}$$

where λ_0 is the free space wavelength of light launched into the fiber and n_x and n_y are the effective indices of refraction of the two modes.

Because each of the two polarization states have different propagation constants they accumulate a relative phase difference as the light propagates along the fiber. To better understand this relative phase difference it is useful to change from the time-dependent form of Eq. 3.1 to the time-harmonic phasor form given as,

$$\tilde{\mathbf{E}}(z) = E_0 e^{-j\beta_z^x z} e^{-j\phi_x} \left[\cos\theta_p \hat{\mathbf{x}} + \sin\theta_p e^{j\left[\left(\beta_z^x - \beta_z^y\right)z + \phi_0\right]}\hat{\mathbf{y}}\right], \tag{3.4}$$

where $\phi_0 = \phi_x - \phi_y$ is the initial relative phase difference between the two polarization states and the total relative phase difference after propagating a distance z through the fiber is defined as

$$\phi = (\beta_z^x - \beta_z^y)\, z + \phi_0. \tag{3.5}$$

The birefringence of the fiber is defined as $B = n_x - n_y$. With this definition Eq. 3.5 can be rewritten as

$$\phi = \frac{2\pi}{\lambda_0} B z + \phi_0. \tag{3.6}$$

An analyzer is placed at the output of the fiber before the light is detected by a photodiode. After passing through the analyzer Eq. 3.1 becomes

$$\mathbf{E}(t,z) = E_0 \cos\theta_p \cos\theta_a \cos(wt - \beta_z^x z - \phi_x)\hat{\mathbf{x}} + E_0 \sin\theta_p \sin\theta_a \cos(wt - \beta_z^y z - \phi_y)\hat{\mathbf{y}}, \tag{3.7}$$

where θ_a is the angle of the analyzer away from the major axis of the core.

The detected intensity of the photodiode is the time-averaged square of the output field

$$I = \frac{1}{T}\int_0^T \|\mathbf{E}\|^2 dt. \tag{3.8}$$

By substituting the output electric field given by Eq. 3.7 into Eq. 3.8, the intensity becomes

$$I = \frac{{E_0}^2}{2}\left[\left(\cos^2\theta_p \cos^2\theta_a + \sin^2\theta_p \sin^2\theta_a\right) + \frac{1}{2}\sin(2\theta_p)\sin(2\theta_a)\cos\phi\right]. \tag{3.9}$$

Assuming that the input polarizer is at an angle, $\theta_p = 45°$, and the output analyzer is at an angle, $\theta_a = -45°$, then Eq. 3.9 can be reduced to

$$I = I_0\left[\frac{1}{2} - \frac{1}{2}cos\phi\right]. \tag{3.10}$$

By using the trigometric identity

$$\sin^2\theta = \frac{1-\cos(2\theta)}{2}, \tag{3.11}$$

the final intensity at the photodiode is found to be

$$I = I_0 \sin^2\frac{\phi}{2}. \tag{3.12}$$

As the HF reduces the cladding layer of a section of fiber, the effective indices of the two polarization states change thus changing the birefringence of the fiber. The change in birefringence changes the total relative phase difference between the two states and is given by

$$\Delta\phi = \frac{2\pi}{\lambda_0}\Delta B z, \tag{3.13}$$

where ΔB is the difference between the birefringence after having etched a certain distance and the birefringence of the unetched fiber. By using Eq. 3.13 the change in birefringence of the fiber can be related to the output intensity by substituting Eq. 3.13 into Eq. 3.12 resulting in

$$I = I_0 \sin^2 \frac{\Delta\phi}{2}. \tag{3.14}$$

3.2.2 Etching Simulations

Using the commercially available mode solver BeamPROP, the effective refractive indices of the two polarization states are found for different etch depths. Once the effective indices are found, Eq. 3.14 can be used to calculated the output intensity of light for different core-to-flat distances. The core-to-flat distance is defined as the distance from the top of the core to the flat surface of the D-shape. Figure 3.3 shows the birefringence as a function of core-to-flat distance. As evident by the figure the birefringence does not significantly change until the core-to-flat distance has been reduced to about 2 μm.

Figure 3.4 shows the simulated output intensity using the simulated birefringence data and Eq. 3.14. As the cladding layer above the core is reduced, the oscillations in the intensity increase in frequency because the birefringence begins to change more rapidly.

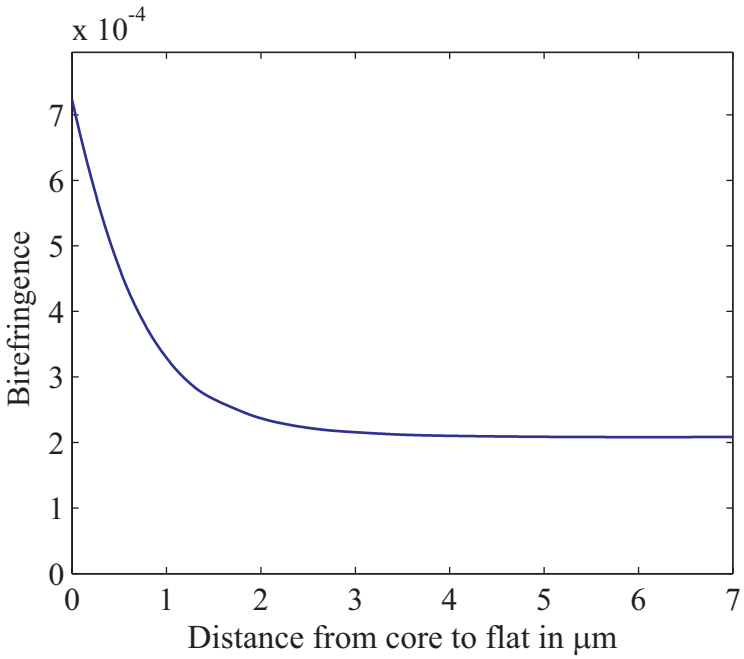

Figure 3.3: Birefringence of a D-fiber as a function of the distance from the top of the core to the flat side of the fiber. The model assumes that the fiber is immersed in HF (n=1.33) with an etch length of 1.5 cm.

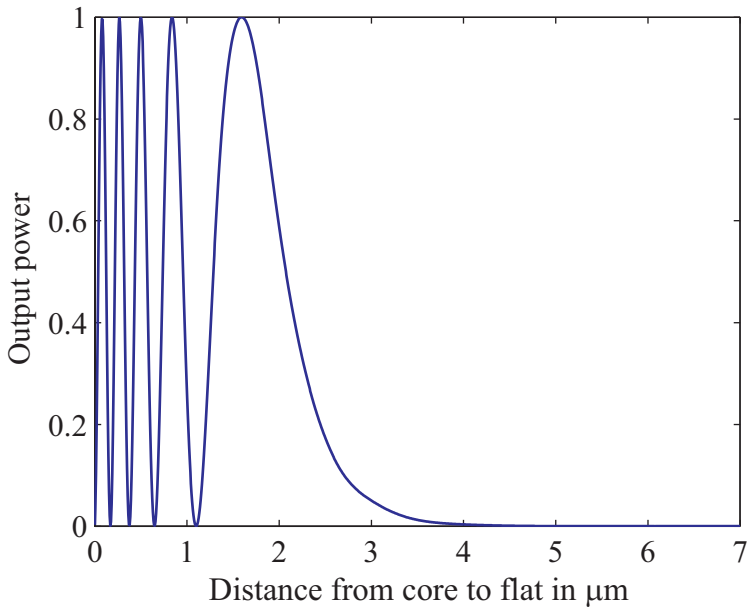

Figure 3.4: Plot of the simulated output power through the analyzer as a function of the distance from the top of the elliptical core to the flat for a horizontal core fiber.

3.2.3 Experimental Results

For most of this work, the etch is terminated when only 0.4 μm of cladding remain above the core. This core-to-flat distance corresponds to approximately three oscillations in output intensity. The etch is performed according to the setup of Fig. 3.2. The actual etch time is variable depending on the environmental conditions such as temperature and humidity. The etch time is also dependent on the acid level in the container and on the D-fiber itself. Different spools of D-fiber tend to exhibit different etch times. Because of the variability in etch time, the in-situ monitoring of the birefringence provides an accurate measurement of the remaining cladding layer above the core of the fiber.

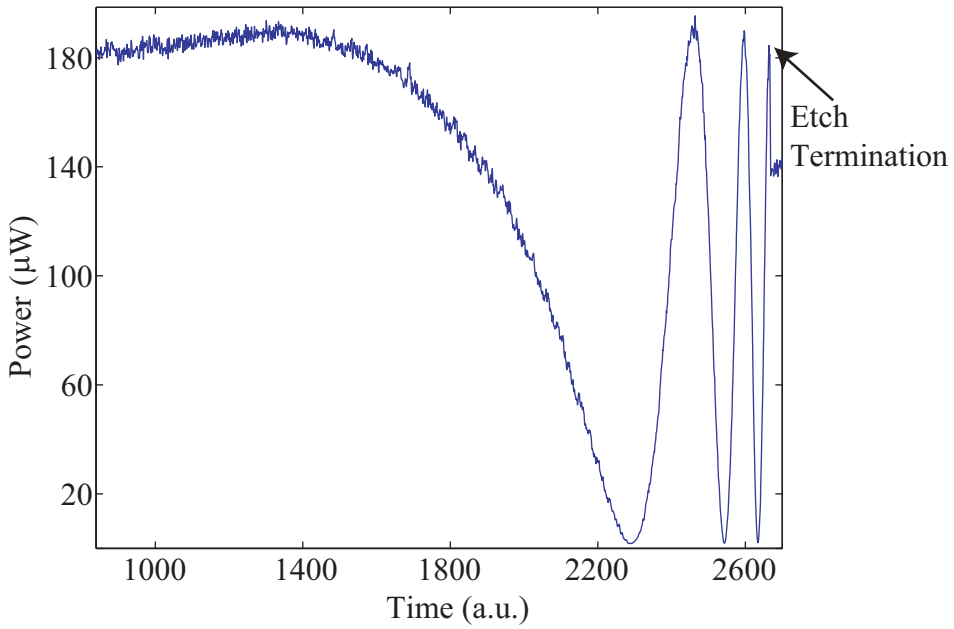

Figure 3.5: Graph showing the output power of the fiber during the etching process. The etch was terminated at the third oscillation.

Figure 3.5 shows the output power from an etch. The fiber is removed from the acid and placed in DI water at the third oscillation indicated by the arrow on the figure. Full extinction is not quite achieved for two possible reasons. First the input polarizer and output analyzer might not be exactly placed at 45° and -45°

with respect to the major axis of the fiber core, and second the extinction ratio of the polarizers is only 25 dB. Excellent agreement between the actual etching and the simulated results is achieved. Figure 3.6 shows that after three oscillations the core-to-flat distance is reduced to about 0.4 μm. The actual distance from the top of the core to the flat is somewhat hard to determine due to the diffusion process during the fiber fabrication that creates a fuzzy boundary between the core and the cladding.

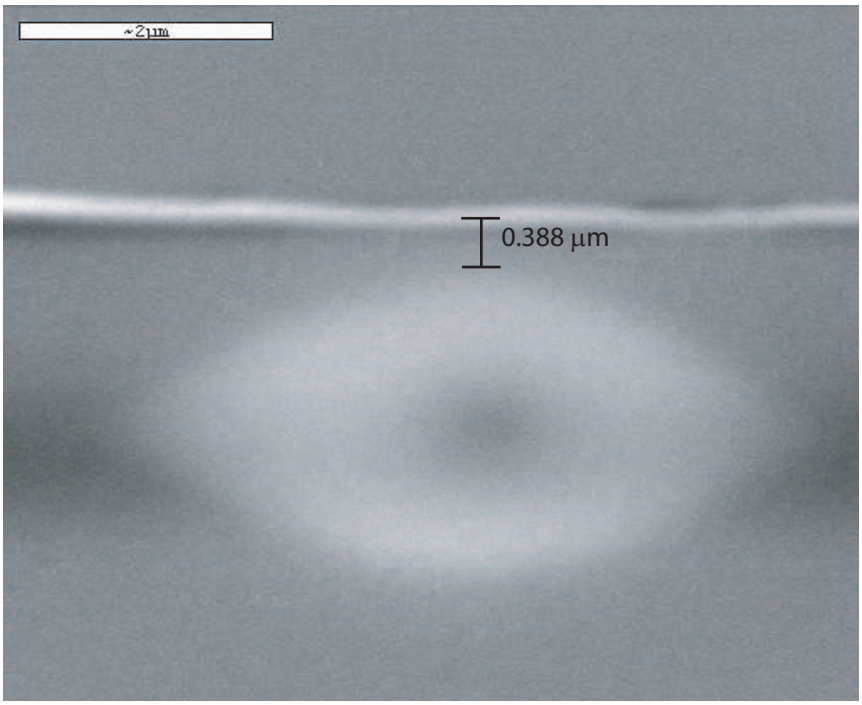

Figure 3.6: SEM image showing the core-to-flat distance to be about 0.4 μm after monitoring 3 oscillations during HF etching.

3.3 Photoresist Application

Preparation of the fiber substrate for photoresist application is crucial for a successful grating. Figure 3.7 shows a grating that is fabricated without a properly prepared fiber surface. Missing grating lines, grating lines that do not stay straight, and fallen over ridges are all common when the substrate is not cleaned and prepared adequately. These non-uniformities in the grating structure ultimately lead to poor

reflectivity and undesired features in the reflection spectrum of the final grating. Adhesion of the photoresist to the D-fiber is a constant battle.

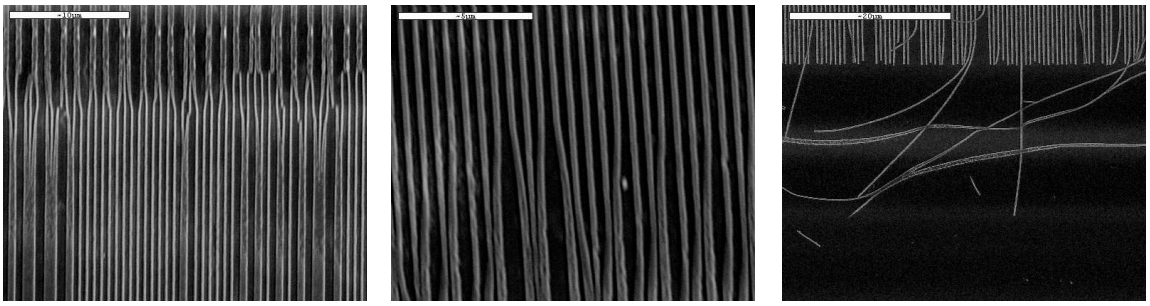

Figure 3.7: Three SEM images showing the resulting grating when the fiber substrate is not properly prepared and cleaned.

Once the fiber cladding is etched down to the desired level, the fiber is ready for the application of photoresist. After the fiber is removed from the acid it is cleaned in a bath of sulfuric acid heated to 190°C for approximately five minutes. The fiber is then rinsed for three minutes under running DI water. Adhesion between photoresist and the glass is dramatically improved if the surface layer of the fiber that was in contact with the HF is removed using plasma etching. Therefore, the fiber is mounted flat side up to a silicon wafer and placed in an RIE and CF_4 plasma is used to remove about 50 nm of this material. Adhesion promoter (Surpass 4000) is then applied, followed by the application of thinned photoresist (2 parts Shipley 1.2L to 1 part thinner) across the entire length of the etched region. The wafer is then spun for 1 minute at 6000 rpm followed by a soft bake for 1 minute at 90°C.

3.4 Photoresist Pre-Exposure

After photoresist is spun onto the fiber, the photoresist is pre-exposed to define the area on the fiber where the actual grating pattern will exist. The Shipley 1.2L photoresist is a positive resist meaning that the areas of the resist on the fiber that do not receive light during an exposure remain after the developing process. Figure 3.8 shows a mask that is used for this exposure step. The black area defines

the area where the grating will be and should be shorter than the etched region. In this work most of the standard gratings are fabricated with a 1.5 cm mask. The mask is placed on the fiber, in the center of the etch region, and the photoresist is blanket exposed using a UV lamp. This step is important in the fabrication process to ensure that the grating does not overlap the section of the fiber that transitions from being etched to unetched.

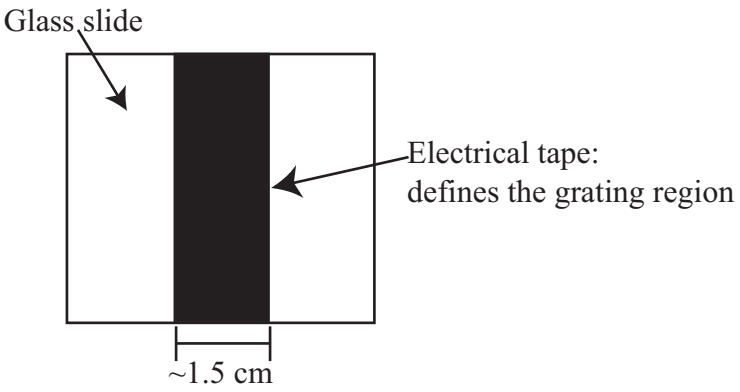

Figure 3.8: Mask used to define the grating region and ensure that the grating won't be fabricated on the transition from etched to unetched fiber.

The transition regions are formed at the edges of the stripped regions where the fiber enters the HF acid. As the fiber etches a small meniscus is formed at this interface creating a gradual transition from unecthed to etched fiber. If the gratings overlap this region of the fiber two things occur. (1) The effective index of the guided mode is no longer constant as it propagates the length of the grating. In effect part of the grating is chirped and the reflection spectrum is wider than a uniform grating. (2) Because only part of the grating is chirped and there is an abrupt change from uniform to non-uniform grating, a sort of Fabry-Pérot cavity is formed [6, 20]. Because the transition regions cause the effective index of the guided mode to increase when going from etched to unetched portions of the fiber, fringes are found on the longer wavelength side of the main Bragg peak in the reflection spectrum.

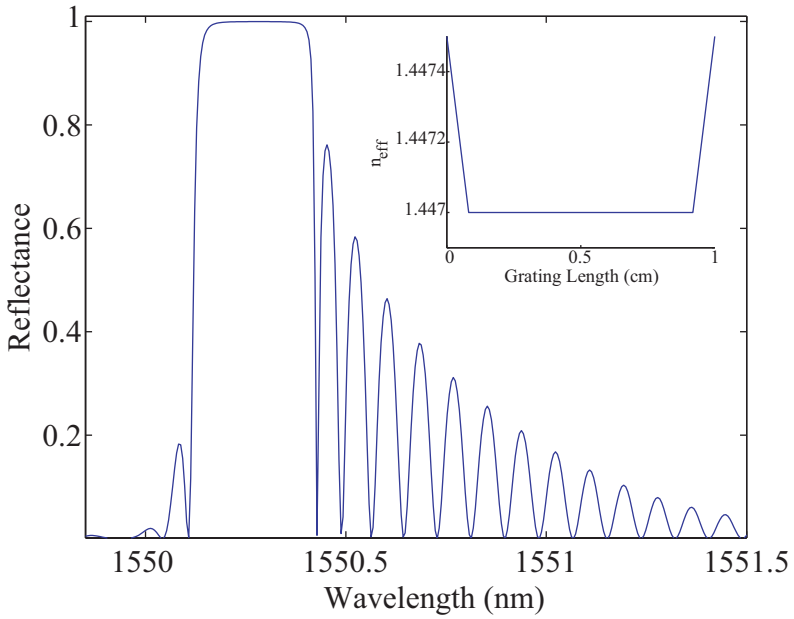

Figure 3.9: Simulated reflection spectrum of a grating that overlaps the two transition regions of an etched fiber. The inset shows the effective refractive index of the guided mode along the length of the grating.

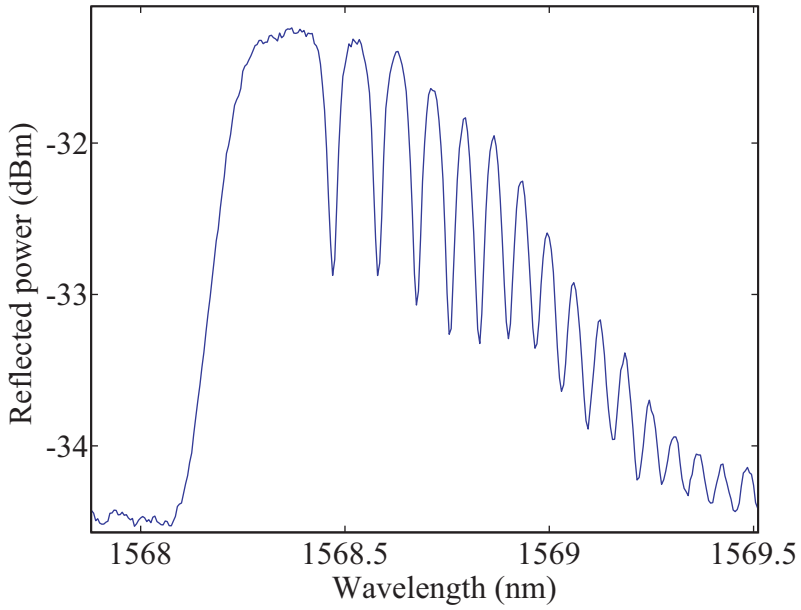

Figure 3.10: Reflection spectrum from a fabricated SR-FBG that overlaps both the transition regions of the etched fiber.

Figure 3.9 shows a simulated reflection spectrum when the grating overlaps both the front and rear transition regions of the etched section of fiber. In the simulation the total grating length is 1 cm with transition lengths of 1 mm each. The inset shows the effective index of refraction of the guided mode along the length of the grating. Figure 3.10 shows the reflection spectrum of an actual grating captured with a Micron Optics SM-125 sensing interrogator. The sensor is fabricated with the grating overlapping the transition regions.

3.5 Exposure to the Two-Beam Interference Pattern

The next step is to expose the photoresist with two interfering beams of light to create a surface relief grating in the photoresist on the flat side of the fiber. Figure 3.11 shows the Lloyd's Mirror arrangement that is used to expose the photoresist [21], in which the mirror and the fiber meet at a right angle. Half of the incident beam falls on the fiber. The other half falls on the mirror, which reflects it onto the fiber. The two halves of the beam combine to create an interference pattern on the surface of the fiber. A Lloyd's mirror configuration is used because it overcomes the problem of small vibrations of optical components, which can wash out a two-beam interference pattern, by having the mirror and the fiber firmly connected to the same base.

The gratings are designed on the fibers so that the Bragg wavelength, λ_B, is 1550 nm. The resulting grating period, Λ, is given by [7]

$$\Lambda = \frac{\lambda_B}{2N}, \tag{3.15}$$

where N is the effective index of the mode in the fiber. The effective indices of both polarizations are very close to 1.45, so the grating period should be 534 nm in order to achieve a reflection peak at 1550 nm.

For the incident beam the 351.4 nm line of an argon ion laser is used. The recorded grating period is given by

$$\Lambda = \frac{\lambda}{2\sin\theta}, \tag{3.16}$$

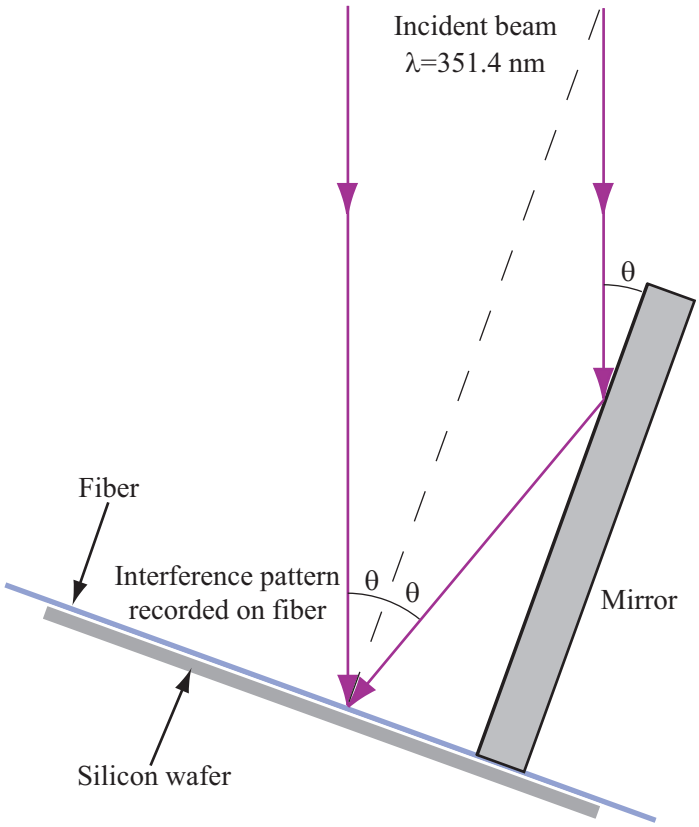

Figure 3.11: Top view of a Lloyd's mirror arrangement for creating an optical interference pattern on the fiber.

where θ is the angle between the normal to the fiber and the interfering beams. To achieve a grating period of 534 nm, the two beams need to be incident onto the fiber at an angle of $\theta = 19.2°$. The photoresist on the fiber is exposed so that the total dose in the most intense portion of the beam is about 21 mJ/cm^2.

Another advantage of the Lloyd's mirror configuration is the ease of which different grating periods can be made. By simply changing the angle of the mirror a different period is formed.

3.6 Grating Transfer into Glass

After exposure, the photoresist is developed in Megaposit MF-24A photoresist developer for 10 seconds and rinsed for 30 seconds in running DI water. The photoresist is then hard baked on a hotplate for 5 minutes. Once the resist is

developed there is a photoresist grating on the flat surface of the D-fiber. The peak-to-trough distance of the grating ridges is found to be between 300 and 400 nm using atomic force microscopy. At this point the gratings are extremely efficient and have reflectivities greater than 99.9%.

In many of the sensing applications it is insufficient to leave the grating in the photoresist. In order to physically change the surface of the fiber, the grating is etched into the glass using an RIE with CF_4 plasma. The plasma etch transfers the grating pattern from the photoresist into the flat surface of the optical fiber. An Anelva RIE is used with 300 W of RF power and a flow rate of 25 sccm of CF_4 gas for 1 minute. This step directionally etches both the resist and the glass, transferring the pattern into the glass fiber.

Even though the two-beam interference creates a sinusoidal fringe pattern the non-linear nature of the photoresist creates square gratings [22]. Figure 3.12 shows a cross section of the grating pattern once it is transfered into a silicon wafer.

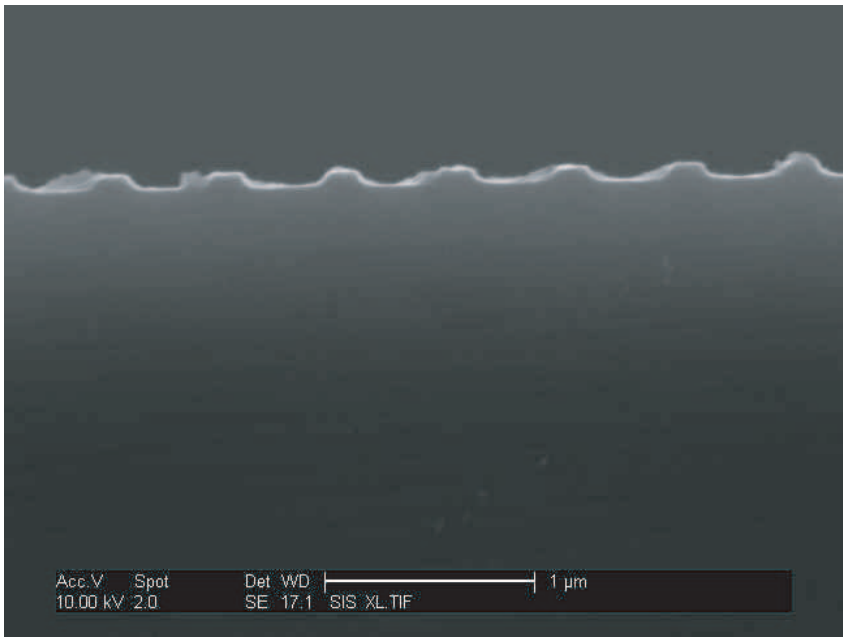

Figure 3.12: Cross sectional image of the gratings in a silicon wafer showing that they are roughly square shaped.

Figure 3.13 shows an SEM image of the gratings etched into the flat side of the D-fiber. These gratings cover a large portion of the flat surface of the fiber and are about 1.5 cm in length. They are about 0.4 μm above the core, and atomic force microscopy shows the grating depth to be ∼80 nm. The fabrication process is completed by rinsing off any remaining photoresist using IPA and acetone.

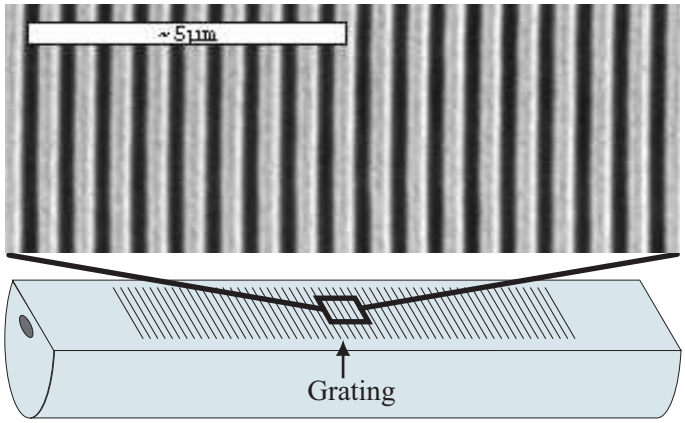

Figure 3.13: SEM image of the grating after it has been RIE etched into the flat surface of the D-fiber.

3.7 Transmission and Reflection Spectra of SR-FBGs

This section shows example transmission and reflection spectra of SR-FBGs when the grating is still in photoresist and after the grating is transferred into the glass fiber. Figure 3.14(a) shows the transmission spectrum from a SR-FBG that is still in photoresist. There are two distinct features that are clearly apparent in the figure. The first feature consists of the multiple sharp dips on the short wavelength side of the main Bragg dip. These resonances are due to coupling between the fundamental guided mode and subsequent cladding modes.

The other obvious feature is the loss profile that is also on the short wavelength side of the main Bragg wavelength. It is believed that this loss profile is a result of radiation mode coupling due to the strong photoresist grating on top of the

D-fiber. Figure 3.14(b) shows a SR-FBG that is transferred into glass. The cladding modes are still apparent in the figure but the loss profile no longer exists.

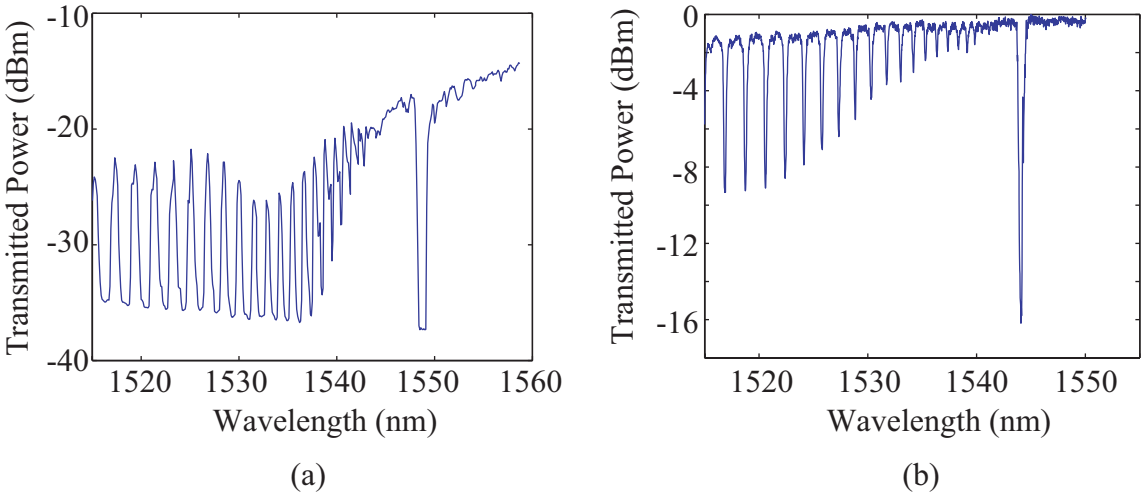

Figure 3.14: (a) Transmission spectrum from a photoresist SR-FBG. (b) Transmission spectrum from a SR-FBG that has been transferred into the glass fiber.

Another feature common to SR-FBGs that are still in photoresist is the ability to see both of the polarization states in the transmission spectrum. Figure 3.15(a) shows the transmission spectrum from the horizontally polarized mode while Fig. 3.15(b) shows the transmission spectrum from the vertically polarized mode. The Bragg dip from the horizontally polarized mode is flat at the bottom because of the noise floor of the measuring equipment. The Bragg dip from the horizontally polarized mode is much wider than the dip from the vertically polarized mode. The difference in the reflectivity between the two modes demonstrates the polarization dependence of SR-FBG which is discussed in the next chapter. Because of this polarization dependence the two modes are not detectable once the grating has been transferred into the glass unless the grating is highly reflective.

Figure 3.16 shows a reflection spectrum from a fully fabricated uniform SR-FBG that is transferred into the glass.

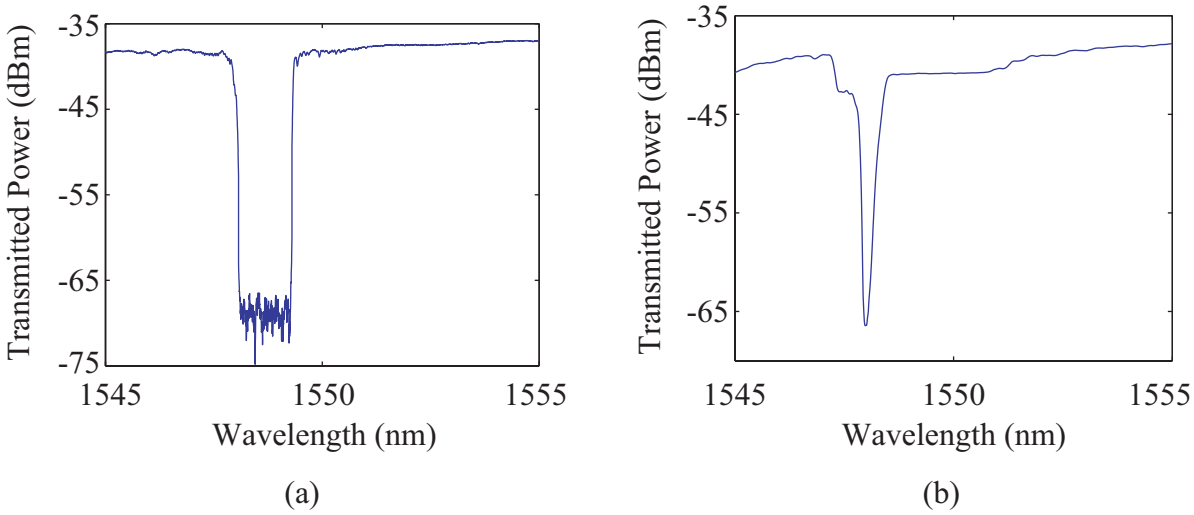

Figure 3.15: (a) Transmission spectrum from a photoresist SR-FBG with horizontally polarized light. (b) Transmission spectrum from a photoresist SR-FBG with vertically polarized light.

3.8 Summary

This chapter describes the foundational steps in SR-FBG fabrication. A successfully fabricated grating is a grating that exhibits the desired reflectivity and spectral characteristics. Most often this means the grating is highly reflective and uniform leading to a single sharp peak in the reflection spectrum. Throughout the fabrication process it is vital to keep the fiber as clean as possible and remove any contaminants that might get on the fiber during each step. The fabrication process can be summarized by first cleaning the fiber, etching away the cladding above the core, applying photoresist and defining the grating region, exposing that region to a two-beam interference pattern, developing the resist, and transferring the photoresist grating into the glass surface of the fiber.

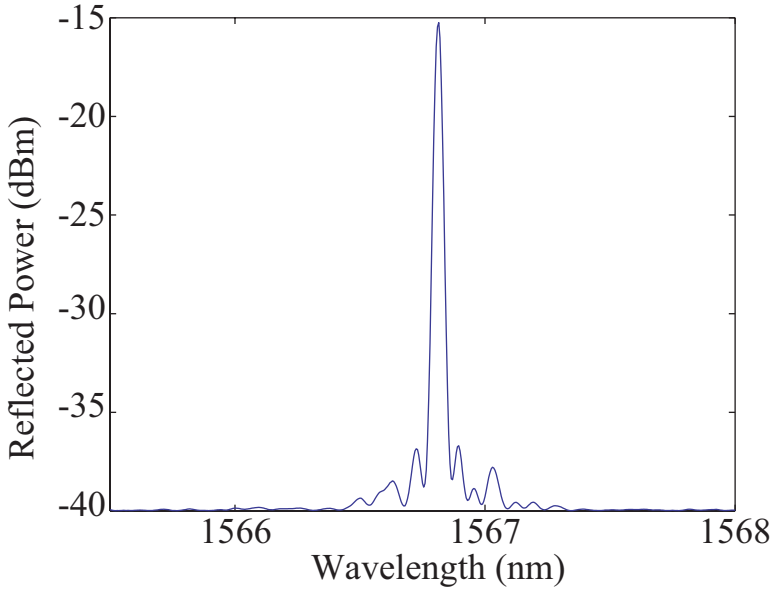

Figure 3.16: Graph showing a typical reflection spectrum from a uniform SR-FBG. The peak reflectance is about 97%.

Chapter 4

Polarization Analysis of SR-FBGs

Because the core of the D-fiber is elliptical, two polarization states are supported. These two polarization states are essentially two modes in the fiber with two different electric field profiles and two different effective indices of refraction. When light is equally launched into both polarization states two Bragg reflections should occur corresponding to the different effective indices of refraction. The additional Bragg wavelength leads to an additional degree of freedom that could be used to better monitor environmental variables such as strain in two dimensions [23].

As explained in the previous chapter the gratings for this work are created on the flat interface between the glass fiber and the surrounding air. Even though the reflection spectrum of SR-FBGs is similar to that of ultraviolet written fiber Bragg gratings (UV-FBGs), the reflection efficiency can be strongly polarization dependent thus limiting the Bragg reflection efficiency of one of the polarization states [24].

Understanding the polarization dependence of SR-FBGs is especially important in sensor applications which might exploit the polarization dependence of the device. Furthermore, having a device that is very polarization dependent can cause problems if the illuminating source is not polarized with the same E-field orientation to produce a return signal from the sensor. For example, super luminescent diodes (SLDs) are desirable as illuminating sources due to their relatively low cost, however, their fabrication process inherently makes them somewhat polarized making them a risky choice if the sensor is strongly polarization dependent.

This chapter describes both theoretically and experimentally how the polarization dependence of a SR-FBG is caused by the glass-air interface and the asymmetry of the etched waveguide structure. The orientation of the transverse electric field with respect to the flat surface of the D-fiber is found to be the dominate source of the polarization dependence independent of the D-fiber core orientation. Theoretically the D-fiber is compared to an asymmetric slab waveguide which is also found to be polarization dependent. Experimentally it is shown that, the polarization dependence can be adjusted by varying the orientation of the elliptical core relative to the flat surface of the D-fiber or by changing the index of refraction of the surrounding media.

4.1 Background and Naming Convention

For a SR-FBG the efficiency of the Bragg reflection depends on many factors that are discussed in previous chapters. The three main factors that contribute to a difference in the efficiency of the two polarization states are: (1) the index contrast of the glass and the surrounding media, (2) the fraction of the modal power that overlaps the area of the grating, and (3) the orientation of the electric field with respect to the flat surface of the fiber.

Figure 4.1 shows a cross-section of D-fiber with three different core orientations. Fig. 4.1(a) shows a horizontal core fiber with the major axis of the core parallel to the flat surface while Fig.4.1(b) and 4.1(c) show fibers where the major axis is perpendicular to the flat of the fiber (vertical core fiber) and rotated away from the flat surface of the fiber (rotated core fiber).

D-fiber supports only hybrid modes, where the electric and magnetic fields are never completely transverse and always have a component in the direction of propagation [25]. For this reason, this chapter adopts the convention for naming the modes as EH or HE placing the dominate longitudinal field first [26].

As the core of an optical fiber changes from circular to elliptical, the HE_{11} fundamental mode degenerates into two fundamental modes [27], the odd HE_{11} (oHE_{11}) and the even HE_{11} (eHE_{11}). Figure 4.2 shows that the transverse electric

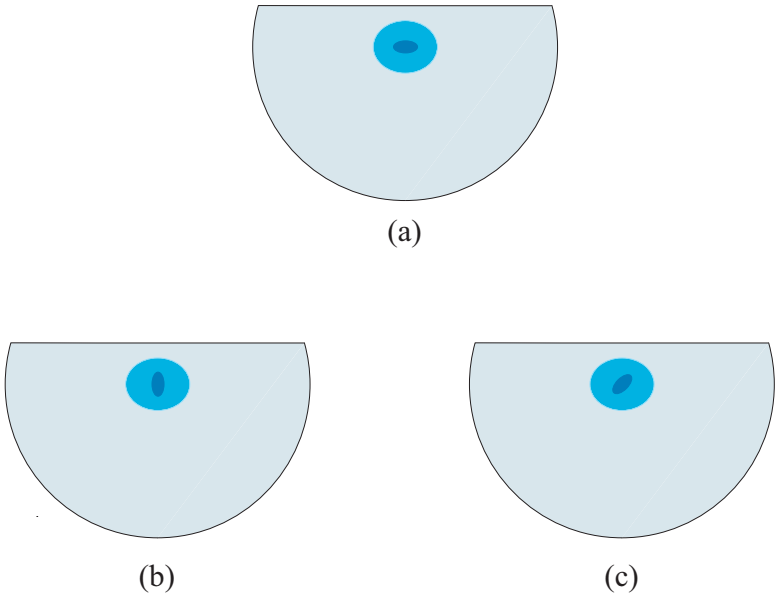

Figure 4.1: Cross-Section of a D-fiber with (a) a horizontal core (b) a vertical core and (c) a rotated core.

field vector for the oHE_{11} mode is polarized along the major axis of the elliptical core and the transverse electric field vector for the eHE_{11} mode is polarized along the minor axis of the elliptical core [25]. This definition is independent of core orientation. These two fundamental modes are called the two polarization states of the fiber. They have slightly different effective mode indices and field profiles.

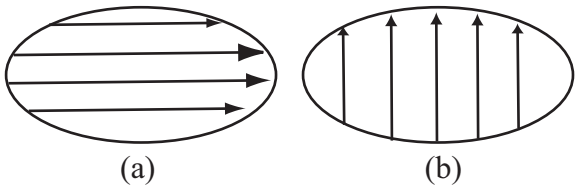

Figure 4.2: Diagram showing the polarization of the transverse electric field for the (a) oHE_{11} mode and the (b) eHE_{11} mode of an elliptical core fiber.

4.2 Polarization Dependence of SR-FBGs

4.2.1 Slab Waveguide Comparison

The SR-FBG requires the D-fiber to be etched such that the cladding-air interface is close to the core; thus, enabling interaction between the light guiding in the core and the grating fabricated on this surface. When the cladding-air interface is brought close to the core it also affects the fundamental modes of the fiber. This change can be thought of as changing the symmetric waveguide (same index on the top and bottom) to an asymmetric waveguide.

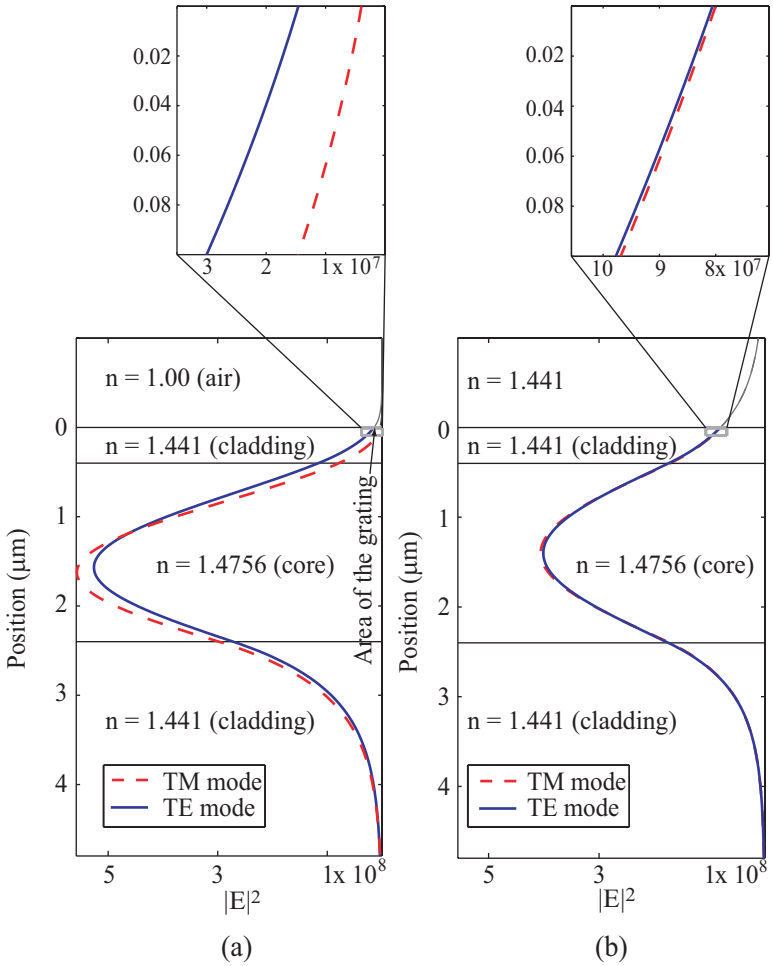

Figure 4.3: (a) Field profile for both the TE (n_{eff}=1.4578) and TM (n_{eff}=1.4566) modes of a multilayer, asymmetric slab waveguide at a free space wavelength of 1.55 μm. (b) Field profile for both the TE (n_{eff}=1.4606) and TM modes (n_{eff}=1.4602) when the surrounding refractive index is equal to the cladding refractive index.

The asymmetric slab waveguide can be used to help show the effect of the cladding-air interface on the fundamental modes. Figure 4.3(a) shows the field profile for both the TE and TM modes of the asymmetric slab waveguide. In both the TE and TM case, the total power in the mode is normalized to be 1 W. The TE or TM mode of the slab waveguide does not exclusively correspond to the oHE_{11} or eHE_{11} mode of the fiber due to the different possible core orientations. However, the TE mode of the slab waveguide does correspond to a mode with the dominant electric field parallel to the flat of the D-fiber while the TM mode corresponds to a mode with the field perpendicular to the flat of the D-fiber. The inset of Fig. 4.3(a) shows the field profile around the area of the grating. It is clear that the TE mode has greater area under the curve, representing more power and more modal field overlap, in the region of the grating when compared to the TM mode. The larger modal field overlap means the grating would be more efficient for the TE case. This mode field profile distribution is similar to other asymmetric optical waveguides [28].

The primary cause of different modal field overlap between the two modes is the index difference between the cladding and the surrounding media. By matching the refractive index of the surrounding media with the refractive index of the cladding, the asymmetric waveguide is converted into a symmetric waveguide and Fig. 4.3(b) shows that the modal field overlap becomes equal.

4.2.2 Field Discontinuities at the Air-Cladding Interface

Another effect of the air-cladding interface that contributes to the polarization dependence of SR-FBGs is the presence of field discontinuities, in the area of the grating, when the transverse electric field is polarized perpendicular to this interface. The boundary condition equations are given as,

$$\hat{n} \times (\mathbf{E_1} - \mathbf{E_2}) = 0, \tag{4.1}$$

$$\hat{n} \cdot (\mathbf{D_1} - \mathbf{D_2}) = \rho_\mathbf{s}. \tag{4.2}$$

Equation 4.1 states that when the electric field is tangential to the air-cladding interface then the electric field must be continuous across the boundary. On the other

hand, Eq. 4.2 states that when the electric field is normal to the air-cladding interface then there may be discontinuities at the interface due to dielectric differences between the two materials.

Figure 4.4 shows a contour plot of the oHE_{11} mode in a horizontal core D-fiber. For this core orientation the oHE_{11} mode has the major component of its transverse electric field polarized tangential to the air-cladding interface. The inset shows that the contour lines at the interface and in the area of the surface relief grating are continuous across the boundary as is expected.

Figure 4.5 shows a contour plot of the eHE_{11} mode in a horizontal core D-fiber. For this core orientation the eHE_{11} mode has the major component of its transverse electric field polarized normal to the air-cladding boundary. Unlike the oHE_{11} mode, the inset clearly shows that there are discontinuities at the air-cladding interface and in the area of the grating. These discontinuities reduce the coupling strength between the forward mode propagating normal towards the grating and the backward mode propagating normal away from the grating [29, 30, 31].

Numerous papers are published that account for the field discontinuities when the mode is polarized perpendicular to the flat surface of a surface relief grating [32, 33, 34]. In [29] the choice of the ideal waveguide boundary is chosen such that a reduction in coupling efficiency for the perpendicularly polarized mode is accounted for. Where as in [31] a reduction factor is calculated and multiplied by the calculated coupling coefficient. In this work, the reduction factor is chosen due to its ease of implementation. The new coupling coefficient for a mode polarized perpendicular to the air-cladding interface is given as,

$$\kappa(z) = \frac{\omega\epsilon_0}{4\xi}\int\int \Delta\epsilon_r(x,y,z)|\mathbf{E}(x,y)|^2 \mathrm{d}x\mathrm{d}y, \tag{4.3}$$

where ξ is the reduction factor and is given as,

$$\xi = \frac{1}{2}\Big(\frac{{n_{clad}}^2}{{n_{cover}}^2} + \frac{{n_{cover}}^2}{{n_{clad}}^2}\Big). \tag{4.4}$$

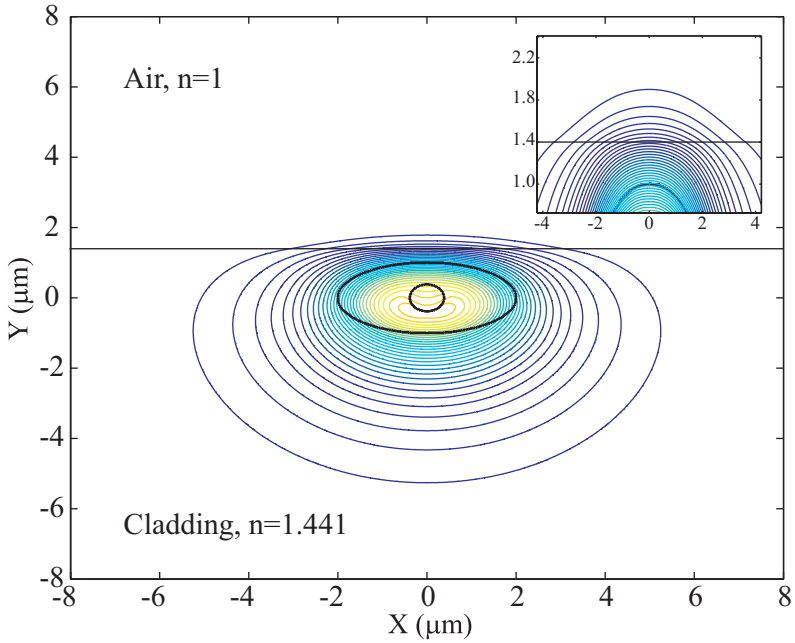

Figure 4.4: Contour plot showing the oHE$_{11}$ electric field profile in a horizontal core D-fiber. The inset is zoomed in around the area of the grating at the air-cladding interface and shows that the e-field is continuous across this boundary.

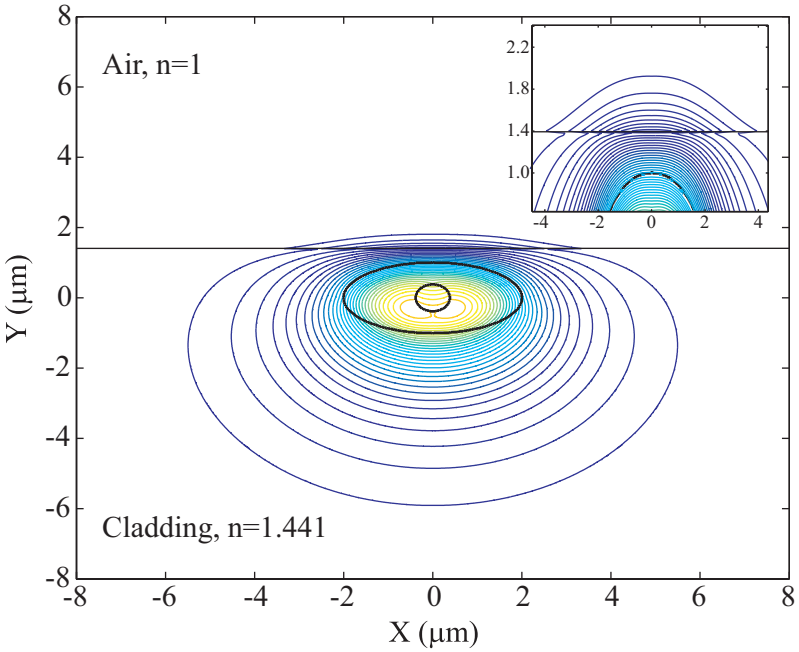

Figure 4.5: Contour plot showing the eHE$_{11}$ electric field profile in a horizontal core D-fiber. The inset is zoomed in around the area of the grating at the air-cladding interface and shows that the e-field has discontinuities across this boundary.

4.2.3 Horizontal and Vertical Core D-fiber

Using the commercial software package BeamPROP^{TM}, the supported modes and corresponding field distributions of the etched D-fiber for both horizontal and vertical core D-fibers are found. The beam propagation method used by BeamPROP^{TM} is based on the paraxial approximation to the Helmholtz equation, which assumes that the field varies slowly along the propagation axis and has small angular divergence from this axis. These assumptions are well suited to problems dealing with light propagation in optical fibers and waveguides [35]. Once the supported mode of the fiber is found, the coupled-mode equations are numerically solved with a Runge-Kutta solver taking into account the reduction in the coupling coefficient for the appropriate mode. To simplify the model, coupling from the forward to the backward propagating core mode is only considered while ignoring coupling to cladding or radiation modes.

Figure 4.6 shows the reflected power difference between the two modes of a horizontal core fiber, P_{odd}-P_{even}, as a function of the reflected power of the oHE$_{11}$ mode, P_{odd}. On the graphs, P_{odd} and P_{even} correspond respectively to the reflected power of the oHE$_{11}$ and eHE$_{11}$ modes. The SR-FBG has a core-to-flat distance of 0.4 μm and a total grating length of 1.2 cm. These grating parameters are consistent with the parameters of the fabricated SR-FBGs which are presented in the following sections. The grating height is varied to simulate different grating efficiencies. The graph is strictly positive meaning that the grating is more efficient for the oHE$_{11}$ mode. As explained earlier, the oHE$_{11}$ mode has the dominant electric field component along the major axis of the ellipse, therefore, the mode with the dominant electric field component parallel to the flat surface has the largest reflection.

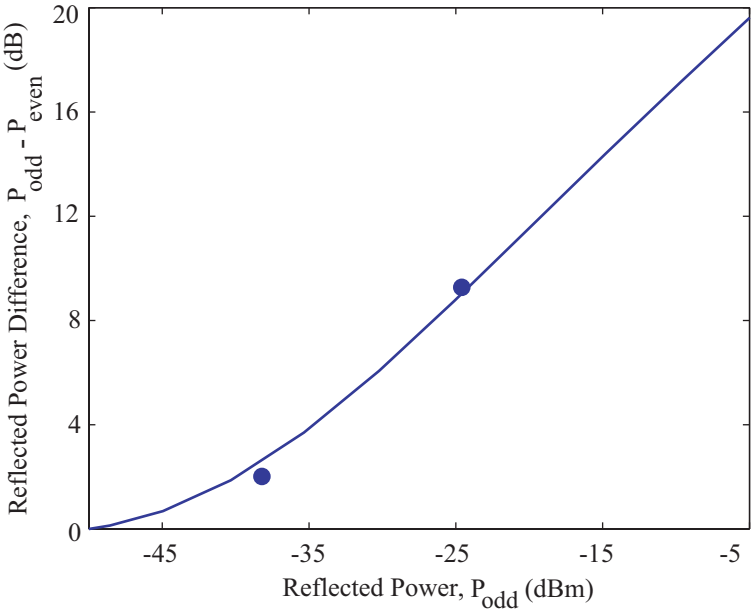

Figure 4.6: Simulation results for horizontal core fiber, P_{odd} and P_{even} correspond to the reflected power of the oHE_{11} and eHE_{11} modes respectively. The dots represents experimental data.

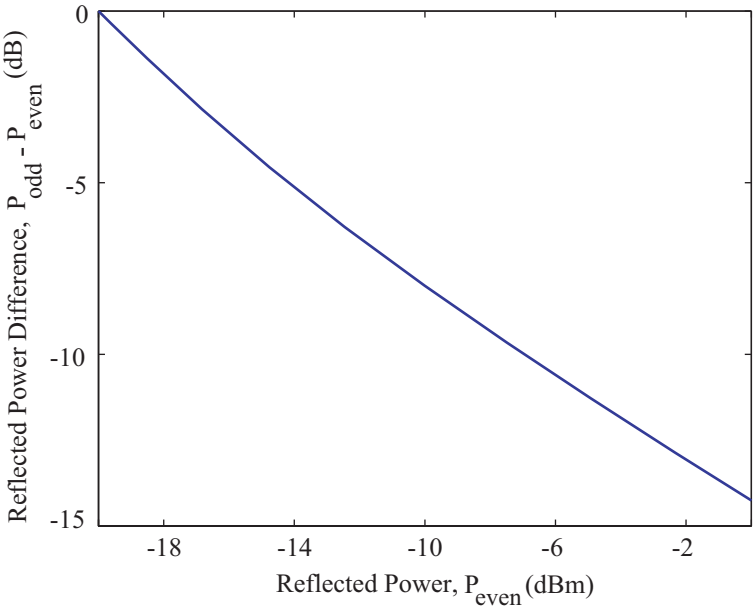

Figure 4.7: Simulation results for vertical core fiber, P_{odd} and P_{even} correspond to the reflected power of the oHE_{11} and eHE_{11} modes respectively.

When vertical core fiber is used, the modes are less tightly confined to the area of the grating and their evanescent tails do not extend out as far when compared to horizontal core fiber. Consequently, in order to generate acceptable reflection efficiencies for either mode, the core-to-flat distance needs to be reduced. The analysis is performed with a core-to-flat distance of 0.1 μm and a total grating length of 1.2 cm. Again the grating height is varied to simulate different grating efficiencies. Unlike the horizontal core fiber which exhibits higher reflectivity for the oHE_{11} mode, Figure 4.7 shows that for the vertical core fiber the reflected power difference between the two modes is strictly negative meaning that the eHE_{11} mode has the greater reflectivity. The eHE_{11} mode has a dominant electric field component along the minor axis of the ellipse and thus, the gratings reflectivity is still greater for the mode that has its dominant electric field component oriented parallel to the cladding-air boundary.

These simulations confirm that when the electric field is perpendicular to the flat surface the electric field profile has significantly less power above the core than when the electric field is parallel to the flat surface, similar to the asymmetric slab waveguide. Hence, the mode with its dominant electric field component parallel to the cladding-air interface has the largest reflection.

4.3 Experimental Verification of Polarization Dependence

To demonstrate the polarization dependence and verify the simulated results gratings are etched into the flat surface of a horizontal core D-fiber $\sim$0.4 μm above the core with a grating period of $\Lambda = 535$ nm. By coupling 670 nm light into the fiber the fabricated grating length is measured to be $\sim$1.2 cm long. Figure 4.8 shows the resulting reflection spectrum using a Micron Optics sm125 FBG interrogator when light is launched into both polarization states.

The larger peak corresponds to reflection by the oHE_{11} mode and has a reflected power of -25 dBm. The smaller peak corresponds to reflection by the eHE_{11} mode and has a reflected power of -34 dBm. The smaller peak is blue shifted $\sim$1 nm from the larger peak due to the difference in the effective indices of the two modes.

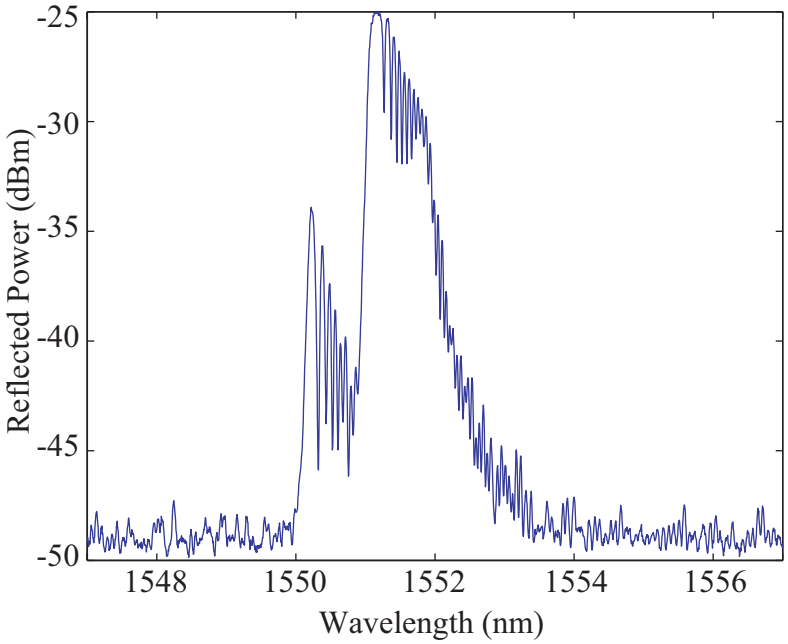

Figure 4.8: Reflection spectrum of a SR-FBG fabricated with horizontal core D-fiber when light is launched into both polarization states. The larger peak corresponds to reflection from the oHE_{11} mode, and the smaller peak corresponds to reflection from the eHE_{11} mode.

The efficiency difference between the oHE_{11} and eHE_{11} modes is $\sim$9 dB and, as shown in Figure 4.6, agrees well with the predicted value.

The widening of the reflection peaks and the longer wavelength features in the reflection spectrum are results of chirping effects that are artifacts from the fabrication process. This particular fiber was fabricated before the effects of creating a grating on the etched transition regions was realized (see Chapter 3 Section 3.4 for more on this effect).

Figure 4.9 shows the reflection spectrum for a SR-FBG with the chirping effect removed by masking off the transition areas before transferring the grating pattern into the glass. The peak reflectivities for the two modes are much less because the masking process shortens the effective grating length. The reflected power difference between the two modes is $\sim$2 dB and, as shown in Figure 4.6, also agrees well with the predicted value.

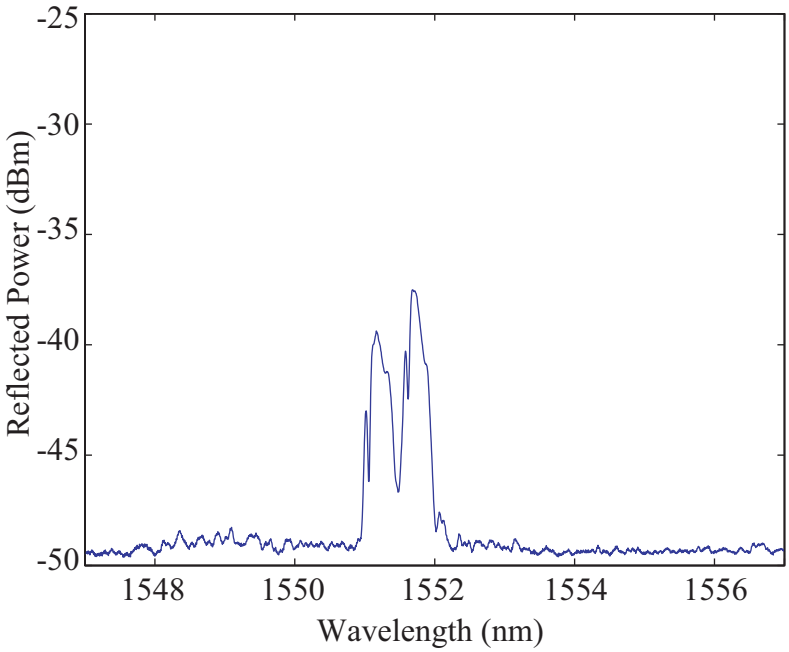

Figure 4.9: Reflection spectrum of a SR-FBG fabricated with horizontal core D-fiber when light is launched into both polarization states. The fiber was pre-masked to ensure that grating did not overlap the transition regions of the etch. The larger peak corresponds to reflection from the oHE_{11} mode, and the smaller peak corresponds to reflection from the eHE_{11} mode.

As explained earlier, one of the primary causes of different reflection coefficients is the index difference between the cladding and the surrounding media. To better demonstrate the effects of the cladding-air interface, the reflection coefficients as a function of the surrounding index of refraction are simulated and measured. For the simulations the same grating parameters as described above for the horizontal core fiber are used, and for the experiment the same fiber presented in Figure 4.8 is used. Refractive index liquids from Cargille Labs vary the index above the grating.

Figure 4.10 shows that as the index above the fiber increases the difference in grating efficiency between the two polarization states decreases. The difference becomes equal when the surrounding refractive index is equal to the cladding index thus creating a symmetric waveguide and eliminating the interface at the flat surface of the fiber. The reflection efficiency for both modes decreases due to a decrease in index contrast at the grating and the center wavelengths shift due to a change in the

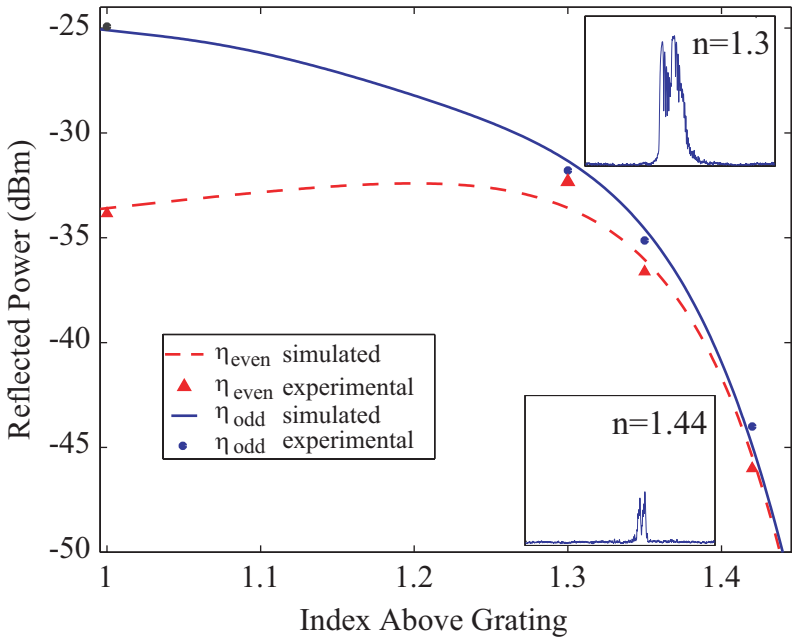

Figure 4.10: Graph showing the simulated and experimental grating efficiencies of a horizontal core SR-FBG for both polarization states versus various indices above the grating. The dots and triangles represent the experimental data, and the insets are reflection spectra at varying indices.

effective indices of the modes. The insets of Figure 4.10 are reflection spectra that demonstrate these trends showing the change in reflection efficiency and wavelength shift for different indices above the grating.

4.4 Rotated Core D-fiber

As demonstrated the fundamental mode that has the largest reflection coefficient is primarily dependent on which mode has a dominant electric field component parallel to the flat surface of the fiber. Thus, the dominant mode can be either the oHE_{11} or eHE_{11} mode dependent on the core orientation of the optical fiber. By rotating the core orientation with respect to the flat surface, the transverse electric field for the two modes can have components that are both parallel and perpendicular to the air-cladding interface reducing the polarization dependence. The efficiency of the Bragg grating is modeled for the two polarization states while rotating the core from an angle of 40° with respect to the normal of the flat surface, through 45°, to

an angle of 50°. Numerical simulations of the fiber are again performed using the commercial software package BeamPROP™.

4.4.1 Analysis

Figure 4.11 shows the calculated difference in reflected power of the two polarization states versus the angle of the core. The simulation is preformed for a 1 cm long grating and a core-to-flat distance of zero. As the figure demonstrates, when the core is in a more vertical position ($< 45°$), the more efficient reflection occurs from the eHE_{11} mode. When the core is oriented at exactly 45° the reflection efficiencies from both the eHE_{11} and oHE_{11} modes are equal, and as the core rotates past 45° to a more horizontal position the oHE_{11} mode produces the more dominant reflection.

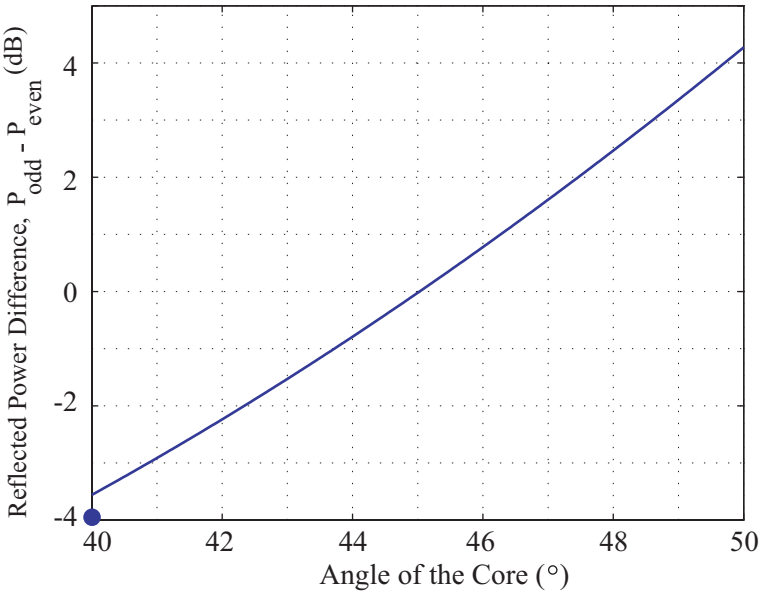

Figure 4.11: Difference in reflected power between the two polarization states as the elliptical core is rotated from 40° to 50° with respect to a line normal to the flat surface. The dot represents experimental data.

The graph is not symmetric about 45° due to changes in mode confinement as the core rotates. As explained earlier, when the core is oriented in a vertical position, the mode is more tightly confined to the core. As the core rotates toward

a more horizontal position the mode is not as tightly confined and the field overlap with the grating increases, thus increasing the reflection efficiency.

4.4.2 Fabrication and Measurement

Manufacturing rotated core D-fiber starts with the elliptical core glass preform which is fabricated with the familiar inside modified chemical vapor deposition (MCVD) process using a tube with non-uniform wall thickness. The preform tube is simultaneously heated to the softening point and subjected to a slight vacuum. In this way the surface tension in the shaped walls during the collapse cause the preform core to be nearly elliptical in cross section despite the nearly perfect circular outer preform shape. In order to produce D-fiber [36], the circular preform is mounted, with the desired angular orientation of the elliptical axis, inside a grooved surface plate fixture and ground. With the D-shape outer surface of the preform and the core in a predetermined geometric relationship to the core, the drawing rate and temperature are controlled to produce a fiber with a cross section similar to that of the preform.

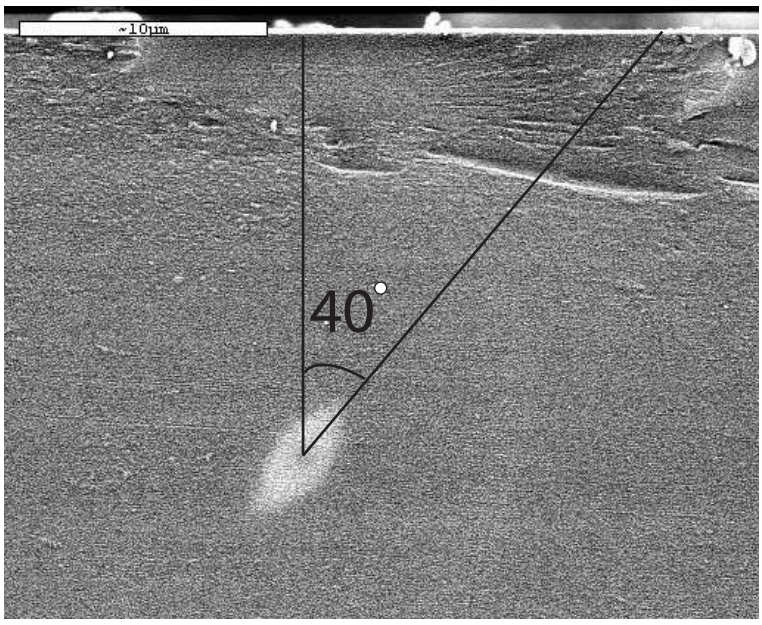

Figure 4.12: A scanning electron microscope (SEM) image of a D-fiber where the core has been rotated 40° from the vertical.

Figure 4.12 is a SEM cross section image of a rotated core D-fiber showing the core of the fiber rotated 40°. To fabricate SR-FBGs with rotated core D-fiber the cladding above the core is reduced. If the core is significantly breached, the photoresist used for patterning the grating onto the flat surface of the fiber does not adhere properly, and the lack of adhesion is detrimental to the fabrication process. To reduce the cladding without breaching the core, red laser light (670 nm) illuminates the fiber and the transmitted power monitored. When the power begins to decline rapidly, as discussed in earlier papers [37, 38], the fiber is removed from the etching solution. Removing the fiber at this point still allows the core to breach as shown in Figure 4.13, however, this small breach is less than 80 nm deep and still allows for effective grating fabrication although the loss caused by the grating increases. By coupling 670 nm light into the fiber, the fabricated grating length is measured to be ∼1 cm. Figure 4.14 shows an SEM image of a completed grating in the rotated core D-fiber.

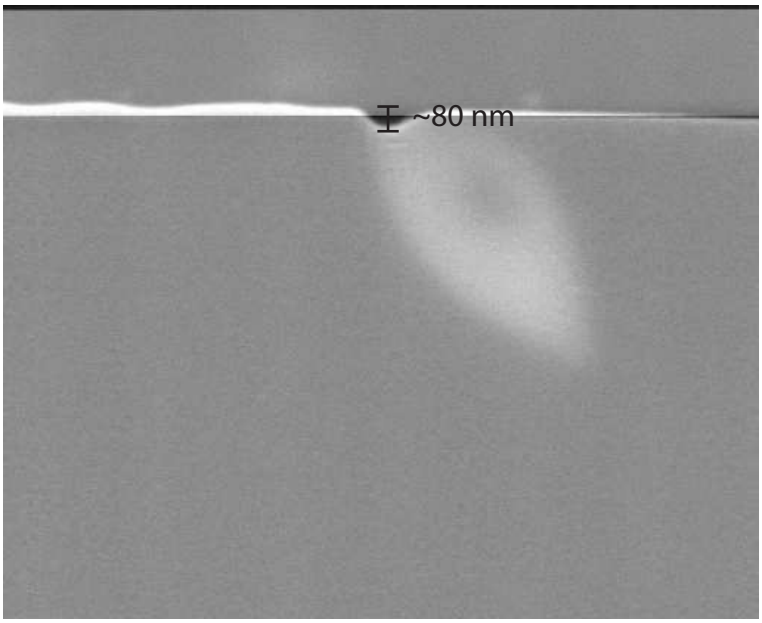

Figure 4.13: An SEM image showing the breach in the core. The depth of the core breach is less than 80 nm.

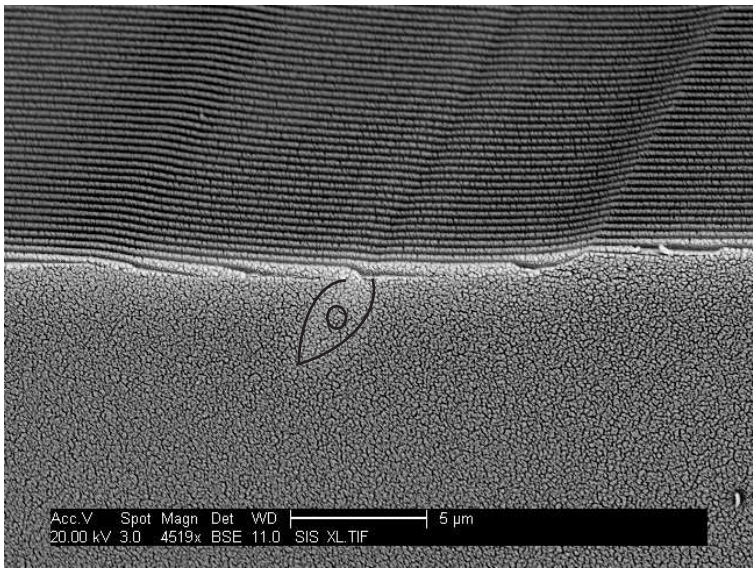

Figure 4.14: An SEM image showing the completed grating in the rotated core fiber.

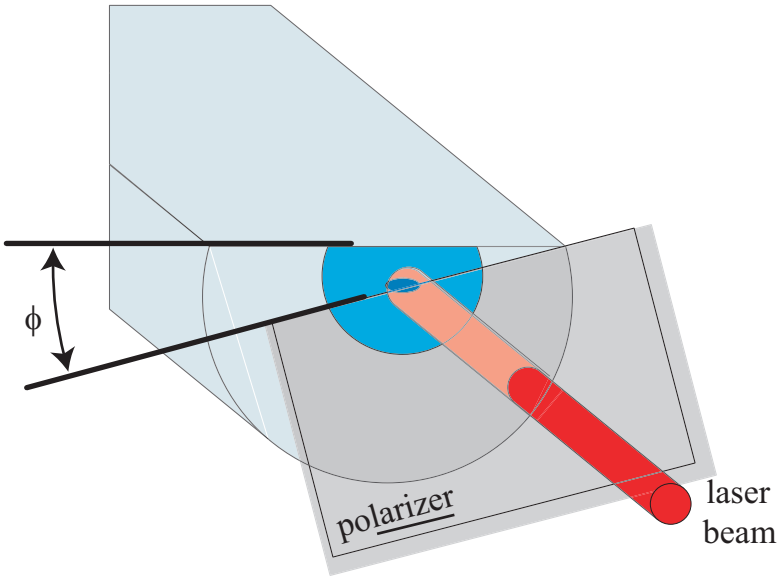

Figure 4.15: Diagram showing a D-fiber illuminated by a laser after it has passed through a polarizer. The polarizer angle, ϕ, is varied to change the orientation of the electric field.

To test the rotated core D-fiber, the setup shown in Figure 4.15 is used. Linearly polarized light is launched into the fiber and the angle between the polarization axis and flat surface of the fiber is varied while monitoring the transmission spectrum of the fiber. Figure 4.16 shows the transmission spectrum for a SR-FBG using the 40° core D-fiber comparing the two polarization states. The Bragg dips occur at different wavelengths when compared to Figure 4.8 because the rotated core D-fiber grating was fabricated with a different grating period. The reflection dip corresponding to the eHE_{11} mode is at 1548.8 nm while a Bragg reflection dip corresponding to the oHE_{11} mode is at 1548.4 nm. The difference in efficiency is ∼4 dB, which agrees well with predicted values. Because the core of the fiber is not manufactured precisely at 45° the difference in efficiencies between the two modes is not exactly zero. Figure 4.17 shows the transmitted power of the Bragg dip as a function of polarizer angle for the two polarization states. There is no change in the center wavelength for the two polarization states as a function of polarizer angle. The loss introduced by the grating is ∼1 dB.

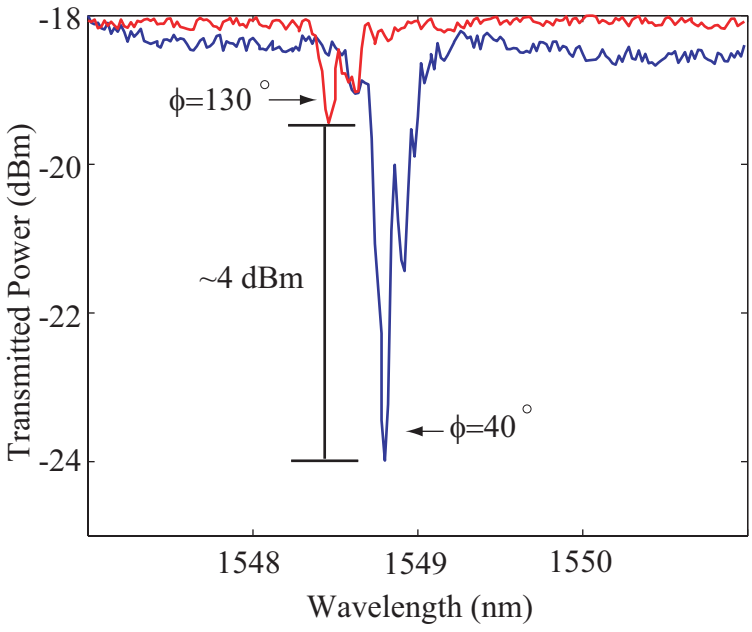

Figure 4.16: Comparison between the two polarization states of a SR-FBG fabricated with 40° core D-fiber.

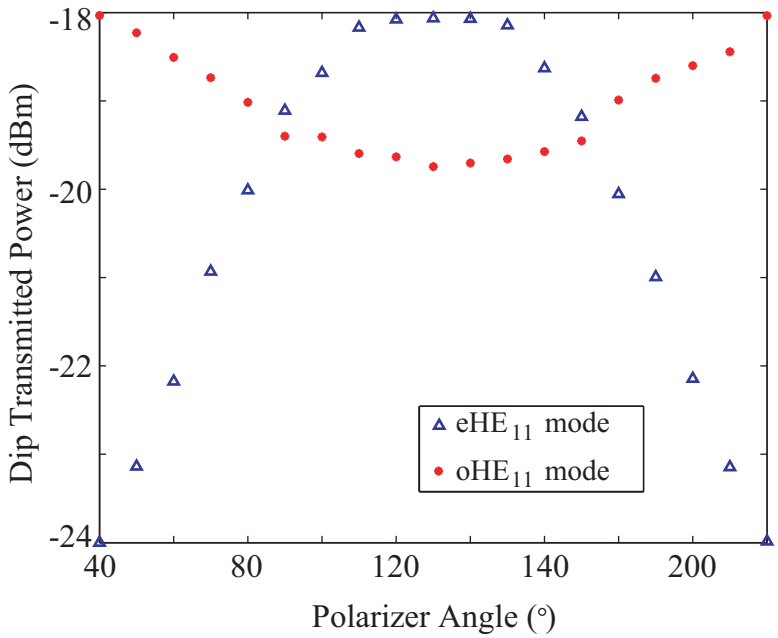

Figure 4.17: Graph showing the transmitted power of the Bragg dip as a function of polarizer angle for both the eHE_{11} and oHE_{11} modes of a rotated core SR-FBG.

4.5 Summary

In this chapter the polarization dependence of SR-FBGs is analyzed in horizontal, vertical, and rotated core D-fiber. The grating efficiency is strongly influenced by the amount of modal field overlap in the area of the grating and also on the orientation of the electric field with respect to the flat surface. The air-cladding interface causes the modal field overlap to be less when the electric field is polarized perpendicular to the flat surface of the fiber compared to when it is polarized parallel to the flat surface. The cladding-air interface also causes discontinuities in the electric field when the field is polarized perpendicular to this boundary. These discontinuities reduce the coupling strength of the forward propagating mode into the backward propagating mode. These results are verified experimentally for horizontal and rotated core fiber.

Results are also presented for a SR-FBG fabricated with rotated core fiber. By using rotated core D-fiber, the transverse electric field for the two polarization

states can have components both parallel and perpendicular to the cladding-air interface. When the core is rotated exactly 45° to this interface the reflection efficiencies for both modes are equal and the polarization dependence can be eliminated.

Chapter 5

High Temperature Sensor

Perhaps the greatest drawback to traditional UV inscribed fiber Bragg grating sensors is the limited temperature range in which the sensors can operate. The limited temperature range seriously affects the device performance whether the intended sensing application is a direct temperature measurement or some other unknown variable.

In this chapter the SR-FBG is presented as a high temperature sensor. As shown previously, SR-FBGs are a physical change in the geometry of the fiber and not just a UV induced change in the core. Because SR-FBGs are formed within the fiber material there is an elimination of any material interface problems or thermal expansion mismatches that might occur if a grating of another material is simply placed in contact with the fiber. These physical changes allow the grating to operate at high temperatures.

5.1 Background and Existing Technologies

As explained in Chapter 2, traditional FBG sensors are fabricated by exposing the optical fibers to an ultraviolet interference pattern [7]. In these standard FBGs, ultraviolet exposure changes the refractive index of the core by a small amount, usually from 10^{-5} to 10^{-3} of the pre-exposure refractive index [39]. The ultraviolet interference pattern creates a modulation in the index of refraction of the core and reflects light when the Bragg condition is met.

Figure 5.1 shows that a major drawback of standard FBG sensors is that the gratings are quickly and permanently washed out by exposure to temperatures

above 200°C [40, 3]. The wash out occurs because high temperature causes the modulated index change to return to a more uniform index profile.

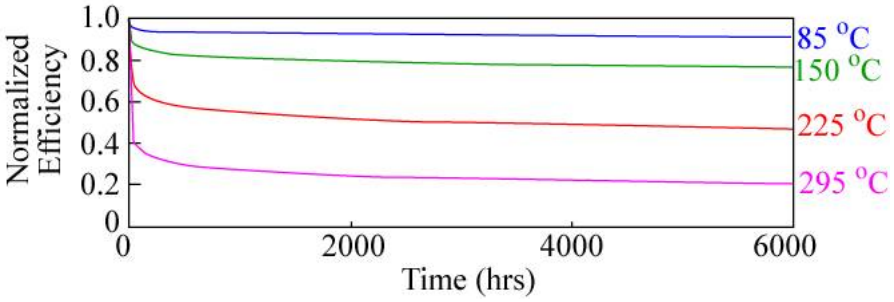

Figure 5.1: Graph showing the decay of UV inscribed FBGs at elevated temperature over time. Taken from [1].

Some researchers have shown that the thermal stability of FBG sensors can be improved upon by various methods. One such method involves doping the fibers with tin, however, this type of fiber also decays quickly above 800°C [41]. Furthermore, by adding additional dopants into the fiber preform transmission and optical properties of the fiber could be undesirably changed.

More recently researchers have shown that chemical composition gratings and gratings written with infrared femtosecond lasers can operate up to 1100°C. However, these methods require a high-temperature annealing process during fabrication [42, 43].

During the time that it has taken to present this work, researchers have shown the possibility of using tapered microstructured fibers for high temperature sensing [44]. These fibers are able to sense temperatures up to 1000°C, however, the use of multimode fiber is undesirable for many applications. In addition, the fiber tapering process dramatically reduces the diameter of the optical fiber and therefore compromises the mechanical reliability.

5.2 Principle of Operation

As with most fiber Bragg grating sensors, the temperature of the fiber can be measured by tracking the peak of the Bragg wavelength reflection. The Bragg reflection depends on the effective index of the guided mode of the fiber and on the periodicity (sometimes referred to as pitch) of the grating. As the temperature surrounding the fiber changes these two grating properties change and thus produce a shift in the Bragg resonance.

The Bragg wavelength equation is given by Eq. 2.1. By taking the partial derivative of this equation with respect to temperature, the change in the Bragg wavelength is related to the change in the effective index of the guided mode and the change in the grating period [39]. The change in Bragg wavelength is expressed as,

$$\frac{\partial \lambda_B}{\partial T} = 2\left(\Lambda \frac{\partial n_{eff}}{\partial T} + n_{eff}\frac{\partial \Lambda}{\partial T}\right), \tag{5.1}$$

where the partial derivative of the effective index of the mode with respect to temperature represents the thermo-optic effect and the partial derivative of the grating period with respect to temperature represents the thermal expansion effect. These two terms can be expressed as the thermo-optic and thermal expansion coefficients by setting,

$$\begin{aligned} \alpha_\Lambda &= \frac{1}{\lambda}\frac{\partial \Lambda}{\partial T}, \\ \alpha_n &= \frac{1}{n_{eff}}\frac{\partial n_{eff}}{\partial T}. \end{aligned} \tag{5.2}$$

For a typical germania-doped, silica-core optical fiber $\alpha_\Lambda = 0.55x10^{-6}$ and $\alpha_n = 8.6x10^{-6}$ to first order. Therefore the dominate effect for the shift in the Bragg wavelength as the temperature changes is the change in the effective index of the guided mode.

5.3 Experimental Setup

In order to test the SR-FBG and measure its sensitivity at high temperatures, the fiber is heated and the shift in Bragg wavelength correlated to the temperature. Figure 5.2 shows the experimental setup used to take the SR-FBG to high

temperature. First the ends of the fiber are terminated with standard fiber connectors in order to more easily launch light into the D-fiber. To ensure that the grating is efficiently heated, the section of the fiber containing the grating is placed directly in the middle of the furnace. A thermocouple is also placed inside the furnace adjacent to the grating to obtain an accurate temperature measurement. The reflection spectrum is measured using a Micron Optics fiber sensor interrogator and both the interrogator and the thermocouple are connected to a PC for simplified data acquisition.

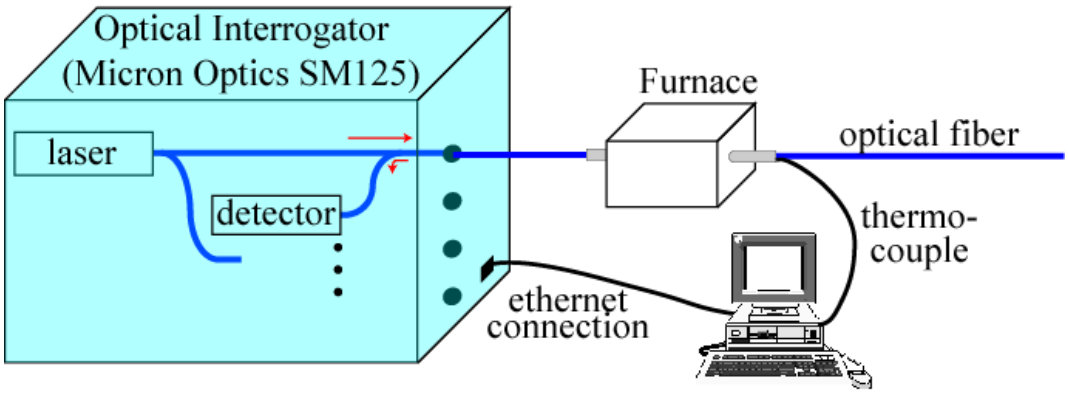

Figure 5.2: Illustration of the test setup used to characterize the SR-FBG response to temperature changes.

5.4 Experimental Results

Figure 5.3(a) shows the reflection spectrum from the grating taken at room temperature and the reflection spectrum recorded at 1000°C. The spectral characteristics have not changed even after such a dramatic change in ambient temperature. The peak reflected power and FWHM are nearly constant throughout the temperature cycling and no hysteresis is observed as the fiber is allowed to cool back down to room temperature. The Bragg wavelength shifts nearly 16 nm over the temperature range.

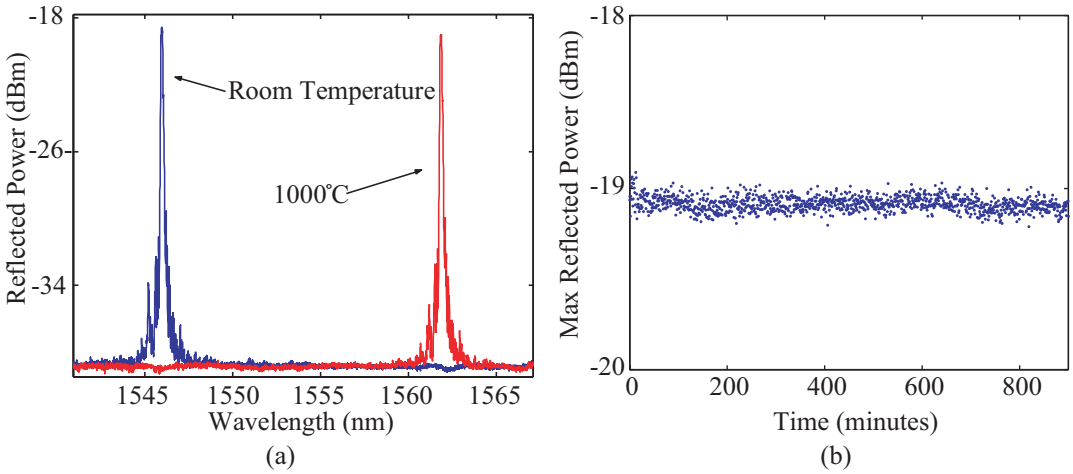

Figure 5.3: (a) Graph showing the reflection spectrum from the SR-FBG at room temperature and at after the fiber is heated to 1000°C. (b) Graph showing the maximum reflected power during nearly 15 hours at high temperature.

5.4.1 Linear vs. Quadratic Behavior

Figure 5.4(a) shows the change in the peak Bragg wavelength as a function of temperature. The dots on the graph are the recorded data and the solid line is a linear fit to the data. While the linear fit is mostly accurate for a small temperature range, the residuals to the fit are not scattered about zero indicating that a linear fit is not ideal. Figure 5.4(b) shows a scatter plot of the residuals to the fit. As evident from the graph a higher order component exists and appears to be quadratic. Figure 5.4(c) shows the derivative for the fitted line. The derivative is approximately 16°C/pm.

Figure 5.5(a) shows the the same temperature test data with a quadratic fit. Figure 5.5(b) is a scatter plot of the residuals from the experimental data to the quadratic fit. Unlike the linear fit residuals, the quadratic fit residuals are scattered about zero over the complete temperature range indicating a good fit. The quadratic fit to the data is more reliable due to the thermo-optic coefficient of fused silica glass [45]. Figure 5.5(c) shows the derivative for the quadratic fit and shows that the sensitivity increase from about 13°C/pm to nearly 18°C/pm.

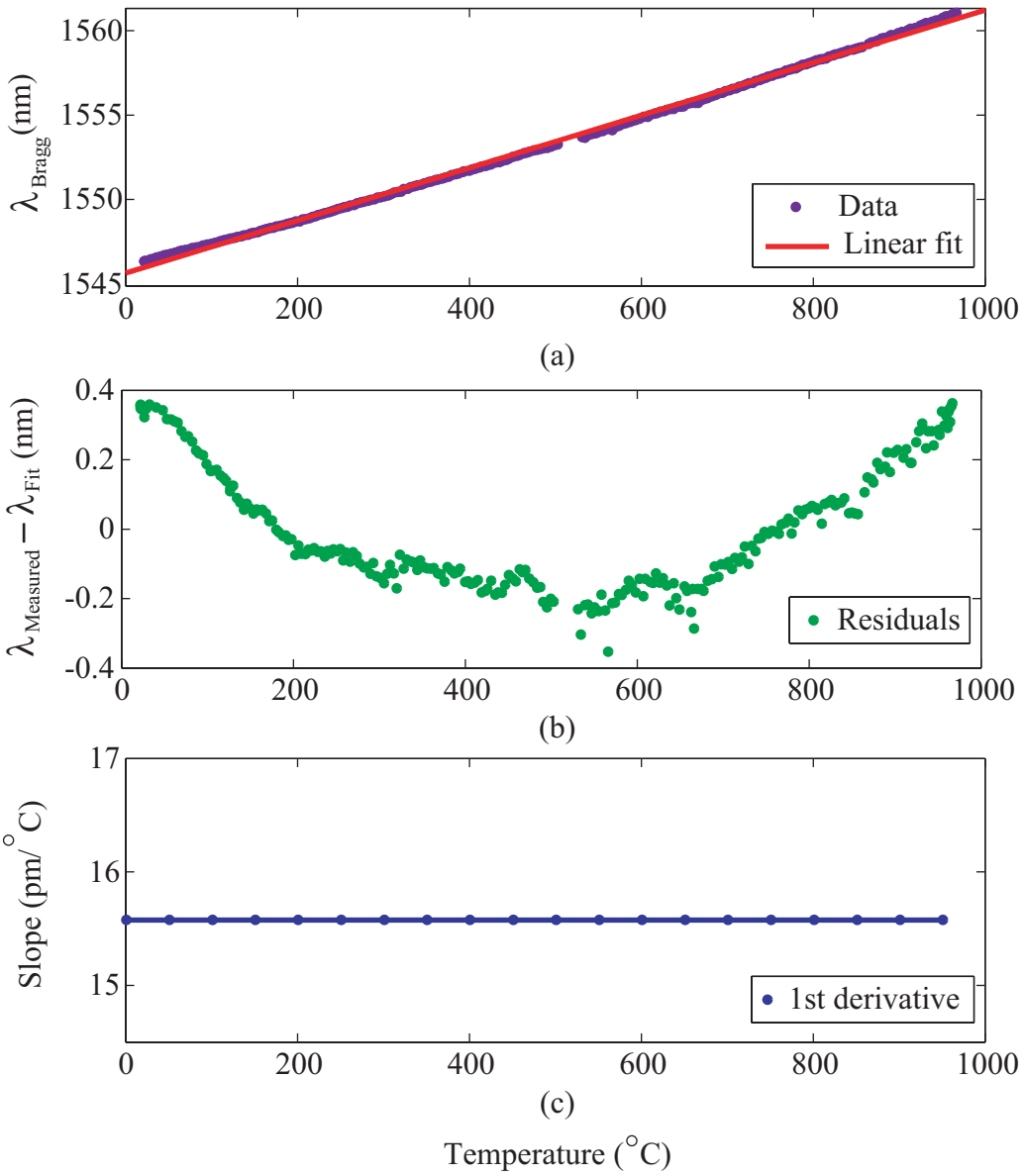

Figure 5.4: (a) Graph showing the peak Bragg wavelength as a function of temperature. The solid line is a linear fit. (b) Residuals to the linear fit and (c) the derivative to the linear fit.

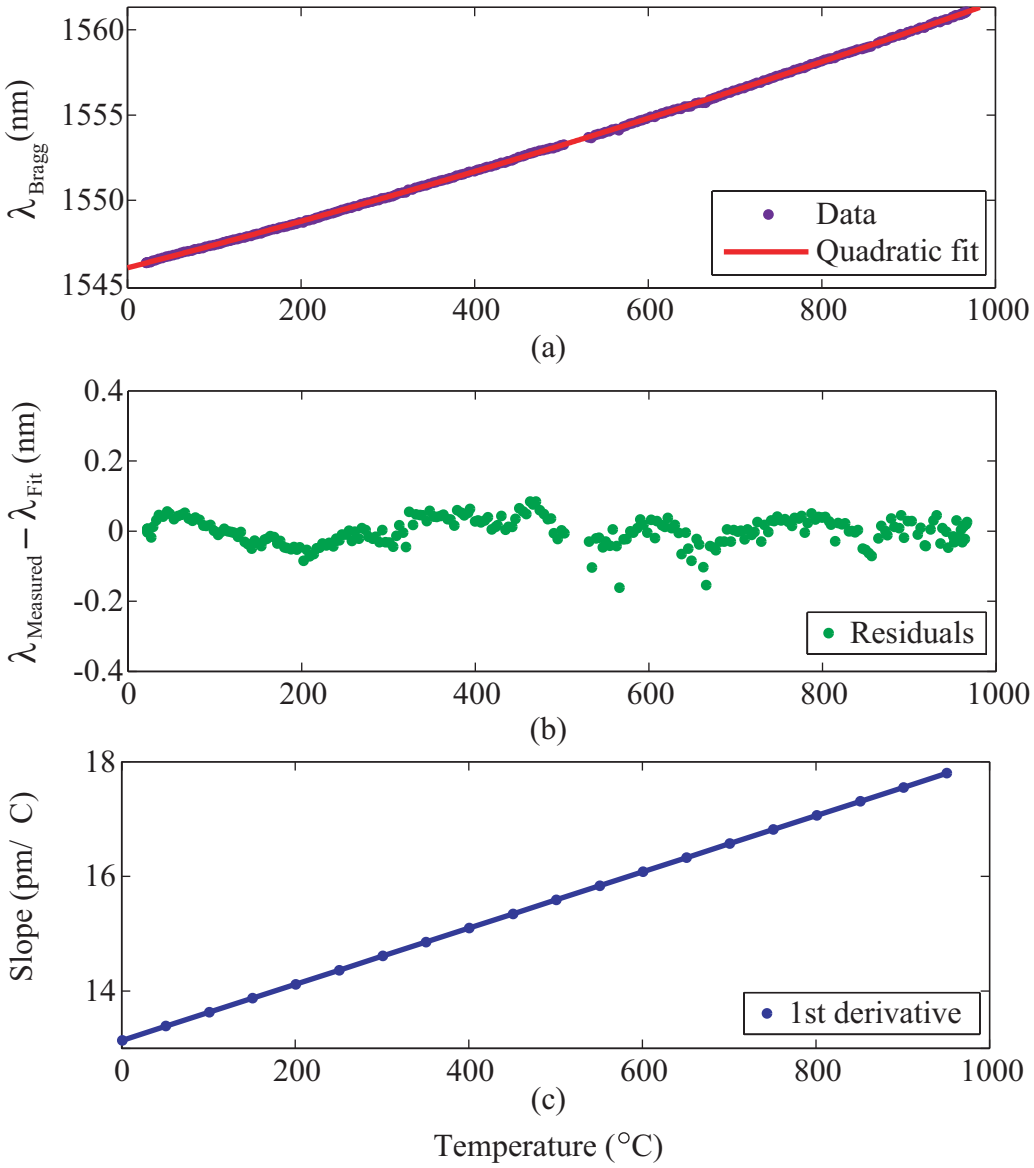

Figure 5.5: (a) Graph showing the peak Bragg wavelength as a function of temperature. The solid line is a quadratic fit. (b) Residuals to the quadratic fit and (c) the derivative to the quadratic fit.

5.4.2 Short Term Heating Effects

In order to determine the upper limit on operating temperature the SR-FBG is illuminated with a high power CO_2 laser. The CO_2 laser emits a wavelength of 10.6 μm. At this wavelength the glass fiber absorbs almost all of the light thus converting the incident power into heat. Using the CO_2 laser also allows for accurate control of an on/off heating pulse.

The reflection spectrum from the grating is monitored while the CO_2 laser illuminates the fiber with 1 second pulses. The fiber is previously calibrated in the tube furnace to determine the wavelength shift to temperature fit. Using the calibrated data it is possible to know the temperature of the fiber based on the Bragg wavelength shift. With each pulse the CO_2 laser power is slightly increased resulting in higher incident temperatures on the optical fiber. The process continues until the Bragg grating fails meaning that the reflection peak is no longer visible due to the melting of the optical fiber. The failure does not occur until the pulse after a 1450°C incident temperature is recorded. On the subsequent pulse the fiber is melted in half. This experiment shows that the SR-FBG can survive extremely high temperatures for a short period of time.

5.4.3 Long Term Heating Effects

The next experiments determine the long term heating effects of the SR-FBG at temperatures near 1000°C. Although core diffusion occurs at these high temperatures the normalized frequency stays constant, thus allowing the fiber to continue guiding light [46, 47].

The SR-FBGs are tested at 1000°C for extended periods of time. After nearly 15 hours at high temperature, Fig. 5.3(b) shows that the gratings still perform as expected with no degradation in reflectance. However, it is apparent that the fibers become brittle after these high temperature tests indicating that a suitable packaging method needs to be investigated. Brittleness is noticed in every fiber that is taken to high temperature including D-fibers without etched gratings and standard cylindrical

fibers. The effect of fiber brittleness at high temperatures is also observed by other researchers [48].

A literature search is performed to determine the general consensus as to the cause of brittleness. The research suggests two possible causes for fiber brittleness. (1) The formation of microcracks in the fiber due to OH diffusion from water vapor in the ambient environment during heating, and (2) devitrification (or the formation of crystals) on the fiber surface which creates weak points where the fiber can fracture [49, 50].

Figure 5.6 shows an SEM image of a fiber that is taken to high temperature for an extended period of time. As evident in the figure, micro-cracks propagate throughout the fiber. These cracks severely weaken the fiber and cause the fiber brittleness. Besides a reduction in the mechanical properties of the fiber, the micro-cracks can also lead to a reduction in the optical properties of the fiber. If the cracks propagate close to the core of the fiber or actually penetrate the core, excessive scattering loss can occur.

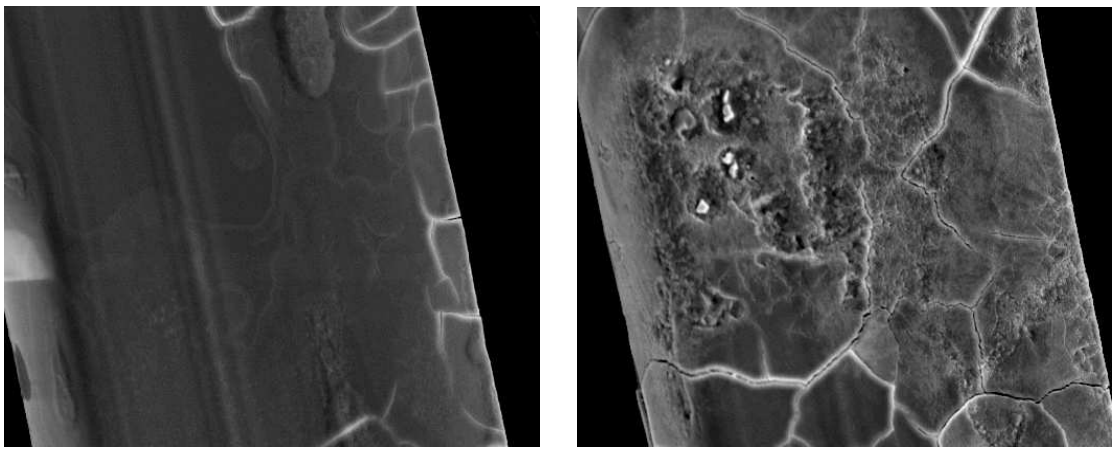

Figure 5.6: SEM figures showing the micro cracks that occur after long term heating of the optical fibers.

Several experiments are performed in order to try and minimize the brittleness of the optical fibers. These trials include trying to heat the fibers in an

environment other than room air, different methods of stripping the jacket off of the fiber, and encapsulation of the fiber in another material.

To heat the fiber in an environment other than room air, argon gas is freely flowed through a ceramic tube that includes the optical fiber. After heating the fiber with the flowing argon gas, a reduction in the fiber brittleness is noticed as the fiber is handled. Even though a reduction in brittleness occurs, the reduction is minimal and it is determined not to be significant enough to pursue further.

Different methods of stripping the fiber include mechanical stripping, acid stripping, heat stripping, and solvent stripping. All of the stripping methods are used to create successful SR-FBG, however, the acid stripping seems to give the greatest reduction in fiber brittleness after long term, high temperature heating. Again, even though there is a noticeable reduction in brittleness, the reduction is minimal.

Trying to encapsulate the fiber in another material is difficult due to the lack of materials that are both able to withstand the high temperature, harsh environment, and demonstrate the necessary optical properties. This approach is not pursued further, but it is suggested that further work needs to be done in this area.

Even though most of the efforts to reduce the fiber brittleness are not successful, it is decided that for many applications the brittleness will not be a point of failure as long as the fiber itself does not break completely. This idea leads to a packaging scheme that protects the fiber even though it might become brittle. By designing a proper package a robust, high temperature probe can be realized.

5.5 SR-FBG Packaging as a High Temperature Probe

In order to package the gratings many design aspects need to be carefully considered. Some of these design considerations are the final sensor application, physical sensor flexibility, sensor to interrogator distance, and final sensor cross sectional area. No matter what the intended sensing application is, the packaging scheme should not dramatically affect or change the unpackaged sensors response. It would be undesirable to create a package that adequately protects the grating and the fiber but that reduces the final sensors sensitivity to the intended measurand.

In the following sections two possible packaging schemes are presented and actual sensors are built and tested. The two options include a rigid and a flexible probe. For both of the packages presented the final sensors are tested as high temperature probes.

5.5.1 Rigid Probe Packaging

The rigid probe is defined as a probe that does not bend when under a reasonable amount of bending force. The rigid probe is useful in applications which do not require the probe to be threaded through any number of system parts. The rigid probe is ideal for situations where the temperature to be measured is accessible such as exhaust from a gas-turbine engine. Also due to the probes rigid package the grating and optical fiber do not break even after repeated high temperature cycles when it is expected that the fiber becomes brittle. The rigid probe offers a sensor that can easily, and repeatably, be handled without having to worry about catastrophic failure due to a break in the optical fiber.

Figure 5.7 shows a schematic of the rigid probe structure. Consulting for this probe design came from Cleveland Electric Labs. To create the the probe the fiber is first inserted into an extremely small stainless steel (s.s.) tube. The tube's outer diameter is 0.020 inches with a wall thickness of 0.005 inches. Before inserting the fiber into the small s.s. tube, the protective polymer jacket is removed using hot sulfuric acid. Removing the jacket is important so that it does not burn off and contaminate the fiber at elevated temperatures. The small tube is used to provide some robustness to the optical fiber and make it easier to handle without compromising the unpackaged sensor's sensitivity. One end of the s.s. tube is capped in order to keep contaminants off of the grating and fiber.

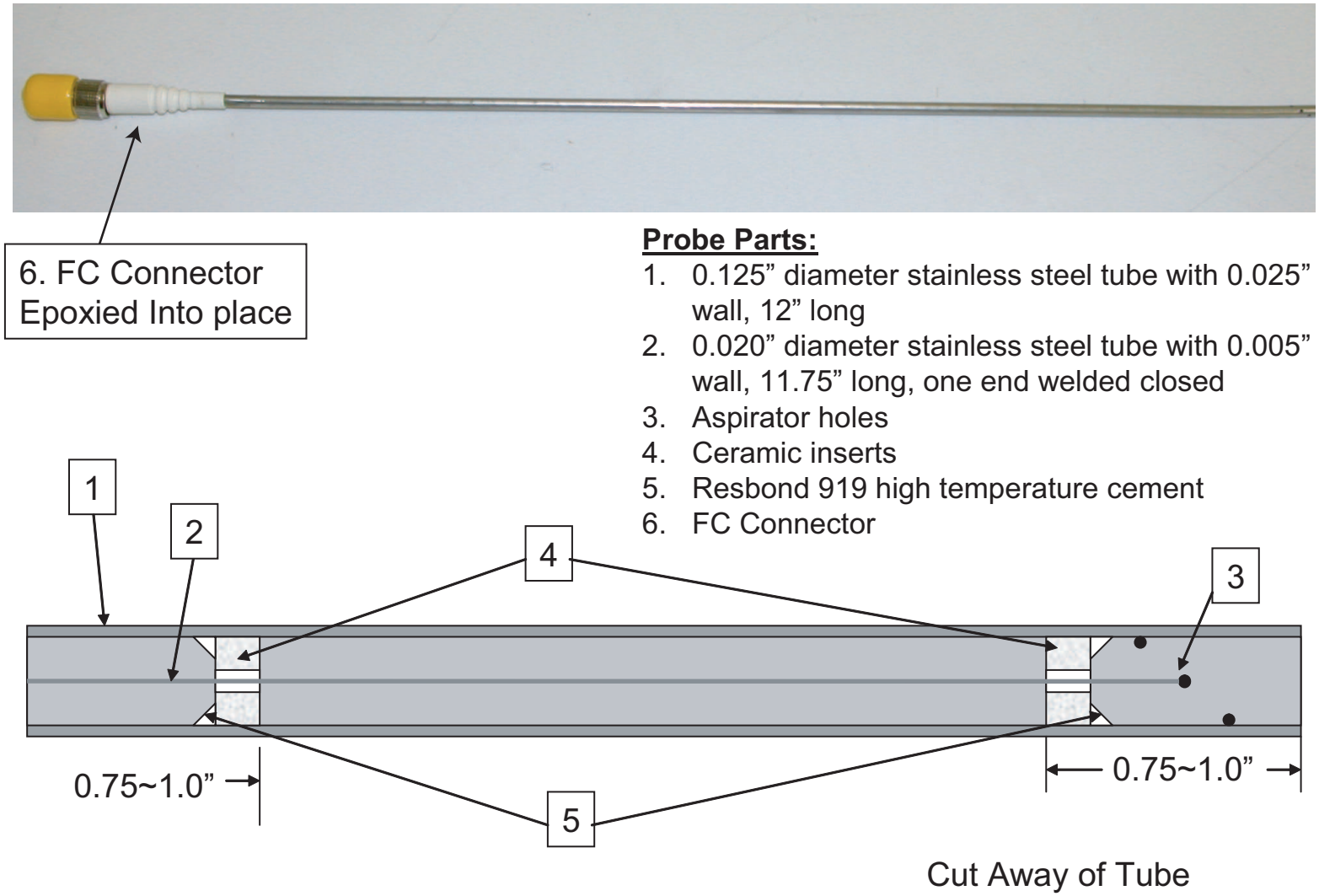

Figure 5.7: Schematic and picture of the rigid probe package with an FC connector used to terminate the probe.

In order to create the rigid probe structure the small s.s. tube is threaded and cemented through ceramic eyelets that are cemented inside of a larger s.s. tube. The larger tube has an outer diameter of 0.125 inches and a wall thickness of 0.025 inches. The end of the tube which contains the the grating is open and aspirator holes are drilled around the tube circumference to allow the most accurate temperature measurement to the surrounding environment. The non-grating end of the D-fiber can be terminated with either an FC connector or it can be spliced to an SMF-28 patch cord using the bridge splice method [51]. The top of Fig. 5.7 shows a fully packaged rigid probe that is terminated with an FC connector.

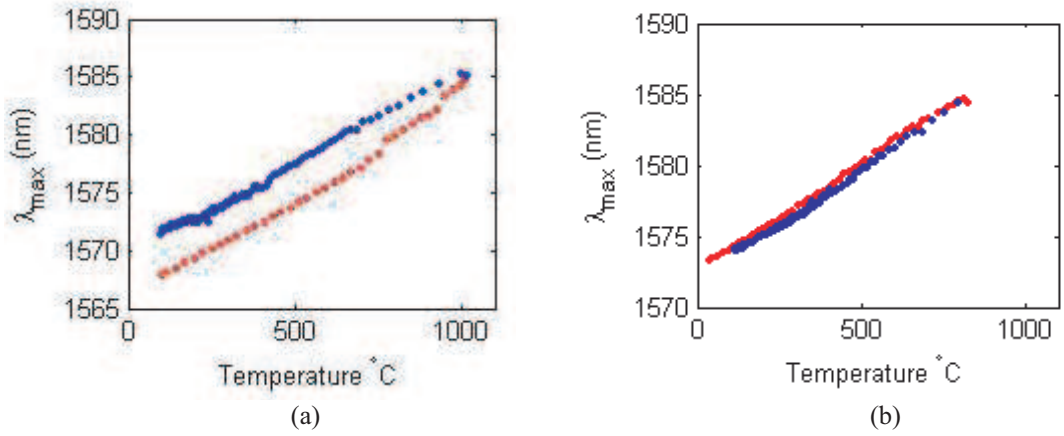

Figure 5.8: (a) Graph showing a large wavelength shift in the Bragg wavelength when the optical fiber is heated and cooled inside of a s.s. tube. The red dots indicate the Bragg wavelength during heating and the blue during cooling. (b) Graph showing that after the initial shift the probe experiences no hysteresis.

Initial testing of the probe demonstrates a large, approximately 5 nm, red shift in the room temperature wavelength after one temperature cycle. Figure 5.8(a) shows this wavelength shift. The red dots indicate the Bragg wavelength as the fiber is heated and the blue dots indicate the Bragg wavelength as the fiber cools. Figure 5.8(b) shows that after continued temperature cycles the room temperature Bragg wavelength remains at the red shifted point. A wavelength shift this large is initially thought to be strain induced due to physical catching of the optical fiber within the

s.s. tube during heating and cooling as the tube expands. Diffusion of the core, and thus a change in the effective index of the guided mode, would not produce a shift this dramatic.

To test the catching theory another fiber is heated to 1000°C inside of the small s.s. tube. Again a large red shift is observed after the probe is allowed to cool. The optical fiber is removed from the tube and the spectrum is retested showing that the Bragg reflection peak remains at its red shifted value. This result indicates that the fiber is not catching on the tube as first suspected. Figure 5.9 shows the reflection spectrum of the probe before being heated, after being heated in the tube, and after being removed from the tube. It is believed that as the s.s. tube is heated, a material is deposited from the tube onto the etched region of the optical fiber causing the large wavelength shift. The widening of the reflection band also indicates that an additional material is being deposited onto the fiber.

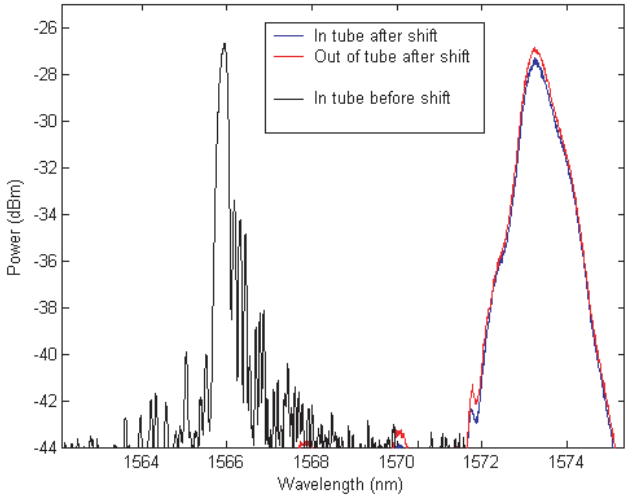

Figure 5.9: Reflection spectra from a grating in a s.s. tube before being heated (black), after being heated and cooled but still in the tube (blue), and after being removed from the tube (red).

To overcome the large wavelength shift, the s.s. tube is first preheated to 1000°C without the optical fiber. Preheating the tube allows for any deposition to

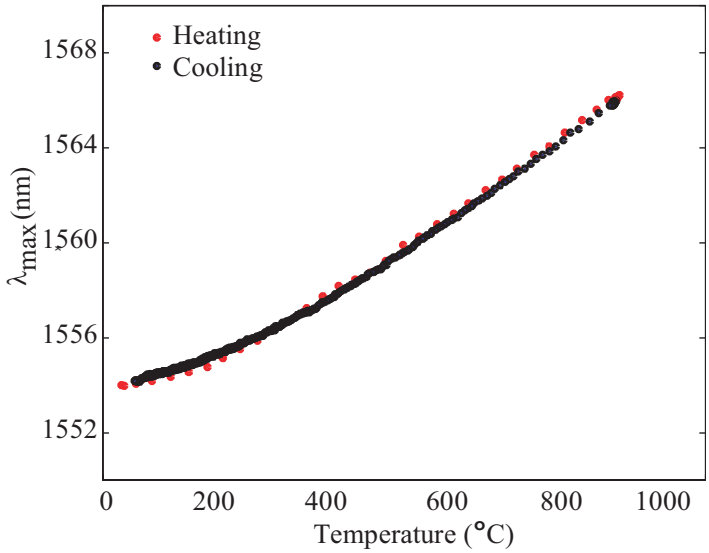

Figure 5.10: Graph showing the Bragg wavelength as a function of temperature for a probe that included a preheating step.

occur without contaminating the optical fiber. Figure 5.10 shows the Bragg wavelength as a function of temperature for a fully packaged rigid probe that includes a preheating step. No hysteresis is observed and the grating's sensitivity is only slightly changed as the trend is more quadratic due to the heating properties of the s.s. tube.

5.5.2 Flexible Probe Packaging

The flexible probe package design is ideal for situations in which the sensor head needs to be threaded through and around system components in order to reach the intended sensing location. The design is well suited to measure temperatures inside of an airframe or in hard to reach engine compartments.

The flexible probe consists of many of the same parts as the rigid probe design. Again a s.s. tube is used to thread the fiber into in order to offer mechanical integrity. The s.s. tube has an outer diameter of 0.0625 inches and a wall thickness of 0.0026 inches. Again the fiber jacket is striped in hot sulfuric acid and the s.s. tube is preheated before the optical fiber is inserted. Figure 5.11 shows a picture of a flexible probe package. For this particular probe the D-fiber is terminated using the

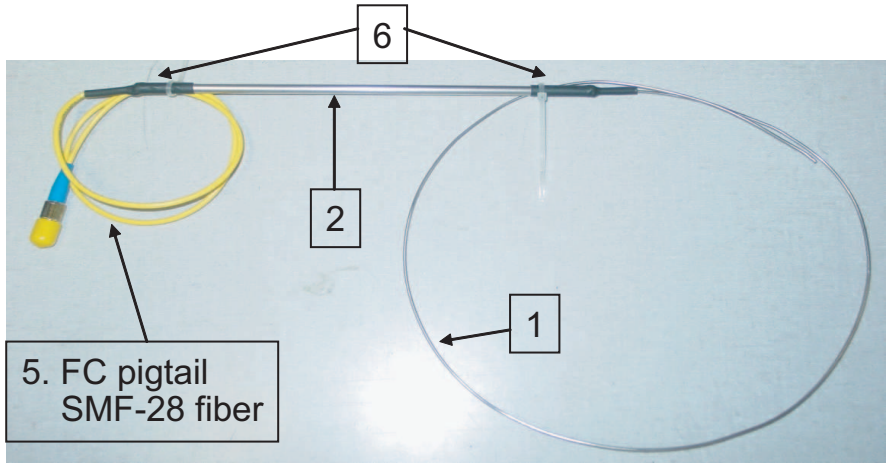

Probe Parts:

1. 0.0625'' outer diameter stainless steel tube with 0.0026'' wall
2. Stainless steel tube spice protector 7/32" o.d. with 0.02" wall
3. E-fiber bridge splice
4. Fusion splice protector sleeve
5. SMF-28 patch cord
6. Heat shrink tubing
7. 5 minute epoxy

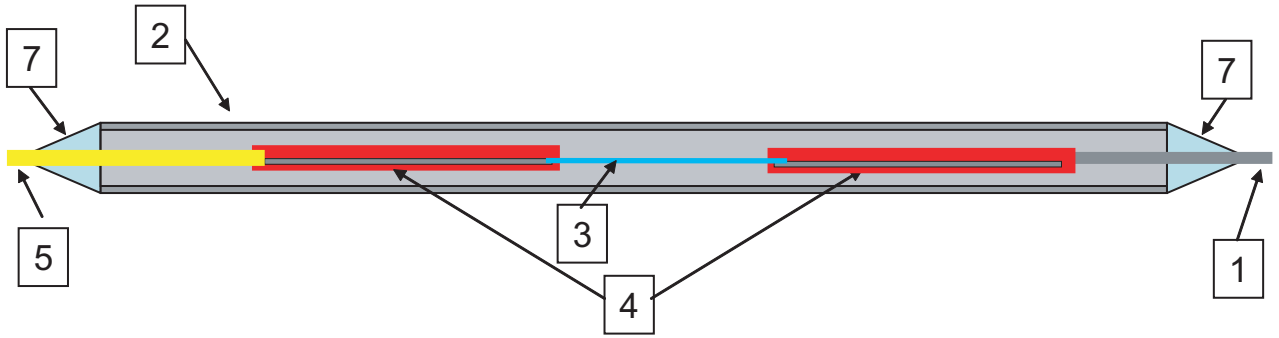

Figure 5.11: Schematic and picture of the flexible probe package with an FC SMF-28 patchcord.

bridge splice method to an SMF-28 patchcord. The two splices are protected with splicing sleeves and a rigid piece of s.s. tube. Again the sensitivity and response is only slightly different due to the s.s. tube.

5.6 Industry Field Testing

Flexible probes are successfully employed as engine temperature probes as part of an engine fire suppression system on board a small aircraft that flies from Florida to Wisconsin for an air show. The probes are integrated into a test aircraft that is built by Comp Air. The probes are able to accurately monitor the temperature and the flexibility and durability allows them to be inserted into hard to reach compartments. Figure 5.12 illustrates that the aircraft is instrumented with standard FBG sensors on the wings for strain and moderate temperature sensing and with the SR-FBG flexible probes inside the engine compartment.

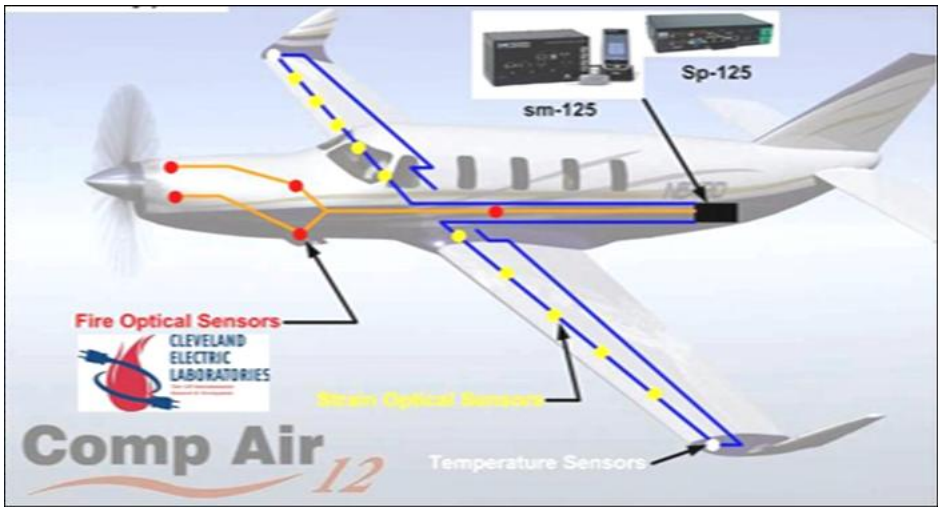

Figure 5.12: Illustration of the personal airplane used in the field test indicating the locations of the FBG sensing elements and the location of the sensor interrogation system.

The SR-FBG probes are installed into the aircraft by Chandler Monitoring Systems Inc. Figure 5.13 shows the engine compartment of the aircraft where two of

the sensning probes are installed. Figure 5.14 shows one of the probes that is installed into the aircraft. The SR-FBG sensing elements are installed into a 2 foot and a 3 foot section of the flexible s.s. tubing. Figure 5.15 shows a picture of the probe that is integrated into the engine compartment.

Figure 5.13: The engine compartment of the aircraft where the SR-FBG high temperature probes were installed.

The major accomplishment of this field test shows the ability of the SR-FBG probes to operate in a relevant test environment. In addition to a real demonstration of the probes, this test also demonstrates that the SR-FBG probes can be installed in external facilities and by external personal not intimately familiar with optical fiber sensors.

5.7 Summary

The SR-FBG is shown to be well suited for high temperature measurements. The physical change in the D-fiber's topography means that the grating is not washed out at elevated temperatures. Unlike standard FBGs that can only operate up to approximately 300°C, SR-FBGs can operate up to 1000°C for extended

Figure 5.14: One of the SR-FBG high temperature probes installed into the test aircraft.

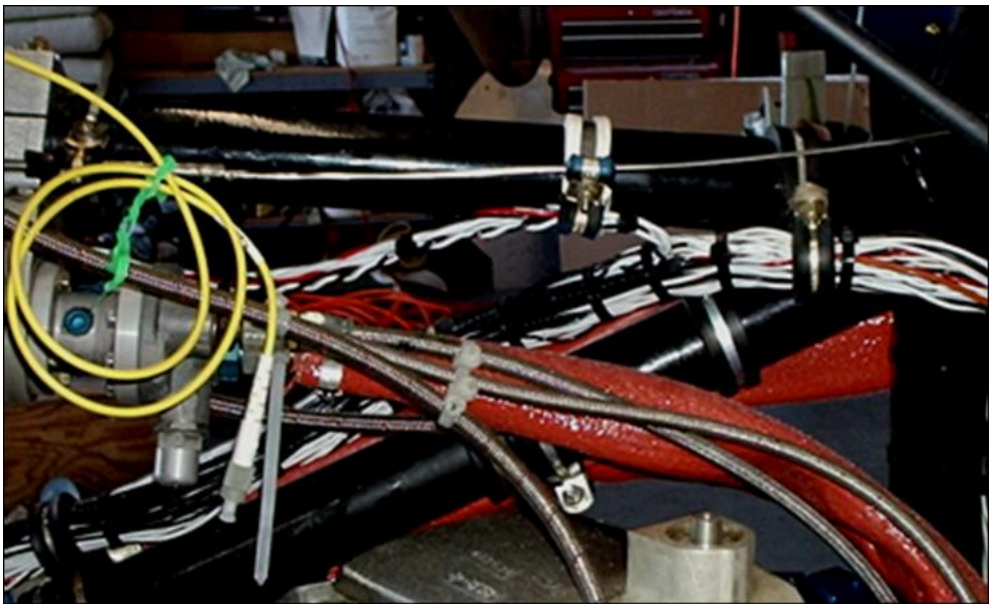

Figure 5.15: The SR-FBG high temperature probe installed into the engine compartment.

periods of time and even up to 1450° for short periods of time. Two packaging designs are also presented in order to give physical strength to the optical fiber and improve ease of handling. The rigid package design is ideal for measurements where the intended point to measure is easily accessible. The rigid package design also allows the probe to be reused for multiple tests even after it is expected that the fiber is brittle. A flexible design is shown to allow the probe to be threaded and inserted through any number of system components in order to reach the intended measuring point.

Chapter 6

Temporal Thermal Response of the High Temperature Sensor

As discussed in the previous chapter, temperature is often an essential variable to measure in any system. Moreover the temperature response can provide meaningful insight into the inner workings of rapidly changing dynamic systems. Knowledge of the temperature response is especially important for systems which use combustible fuels for conversion into mechanical energy such as internal combustion engines [52]. Observing the temperature history, temperature fluctuations, and overall non-steady state temperature response allows for fine tuning of the system that can lead to better energy conversion factors and increase overall performance.

In many of these systems, such as gas turbine engines, there are two main requirements to attain improved temperature sensing. (1) The sensing elements need to withstand high temperature environments often in excess of 1000°C. (2) The sensing elements and the interrogation system need to monitor many sensing elements with a fast response time to reflect the system dynamics.

Traditional thermocouples consist of two metals that form a junction. The temporal response of thermocouples is dependent on the specific metals used to form the junction and also on the physical dimensions of the metal. Many thermocouples are developed for rapid response [53], however, if more than one sensor is required to monitor the system, the combined thermocouple weight, complexity, and power budget needed to monitor the sensors quickly increases. In addition, if the thermocouple is used in a combustible or explosive system, the generated voltage across the junction would be undesirable as it could lead to premature combustion or explosion.

FBGs are desirable because they are light weight, small, immune to electromagnetic interference, chemically and electrically inert, are easily multiplexed, and can be efficiently installed into the desired system. Also due to the small physical dimensions and small mass of the optical fiber, fast response times to temperature changes should be observed [52]. However, standard FBGs cannot withstand high temperatures and are usually limited to an operating range of a few hundred degrees Celsius [40].

In this chapter a temperature sensing system is demonstrated that is capable of both high operating temperature and high response speed. The basic sensing element is the SR-FBG [54], which is shown in the previous chapter to be robust at high temperature and has a fast rise time and fall time because of the small cross-sectional size. Furthermore, a high speed optical fiber sensor interrogation system, in development by fellow students at the BYU Electro-Optics Lab, called the fiber sensor integrated monitor (FSIM) is used to track the rapid temperature changes.

6.1 Background on the Fiber Sensor Integrated Monitor (FSIM)

In order to measure the temporal thermal response of the SR-FBG it is essential to use an interrogation system that can probe the sensor at sufficiently high speeds as to observe and record the temperature changes. Traditional optical interrogation systems such as a broadband light source and an optical spectrum analyzer do not operate at the necessary speeds to capture the dynamic response of the grating. Fellow researchers in the Electro-Optics Lab are developing an interrogation system that can capture the data at the required speeds. Furthermore the FSIM is able to record full spectral scans at high speed which makes additional, and highly useful, analysis possible.

The FSIM is an optical fiber sensor monitoring system that incorporates all of the components necessary for high speed interrogating, processing, and communicating data collected from fiber sensors. Figure 6.1 shows a block diagram of the basic FSIM operation. The FSIM can be divided into two main parts which consist of the electronics and the optics.

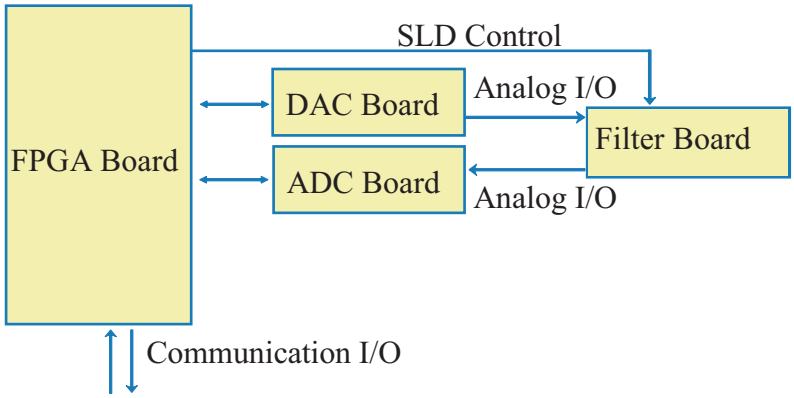

Figure 6.1: Block diagram of the basic FSIM operation.

The main component of the electronics is the field programmable gate array (FPGA) which is used to control the data flow from the optical sensors to the external I/O. The main benefit of the FPGA is the ability to perform tasks in parallel. The parallel processing capability enables the FSIM to attain high complexity without severely impacting the data collection speed. The parallel processing results in a dramatic improvement in operating speed. The use of an FPGA results in the measurement speed being increased from around 10 Hz to greater than 3 kHz [55, 56]. This speed increase enables the fiber sensors to be applicable to more dynamic measurements rather than quasi-static measurements.

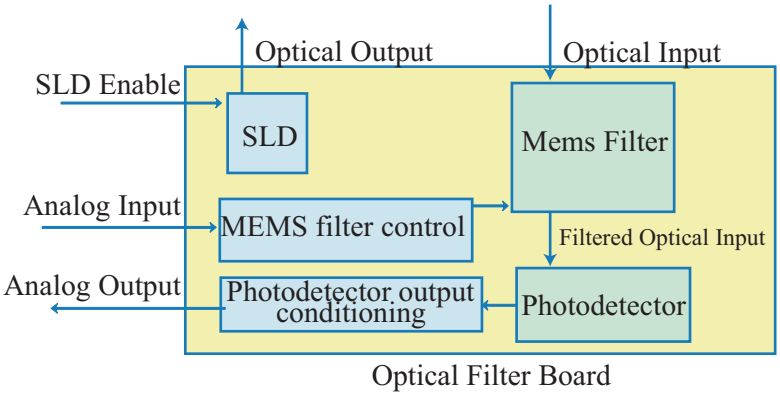

Figure 6.2: Block diagram of the optical filter board.

Figure 6.2 shows the optical components used in the FSIM. The key optical component of the FSIM is a MEMS based tunable optical filter. This wavelength discriminator is a Fabry-Pérot optical filter that transmits a narrow wavelength band (approximately 60 pm wide) that can be tuned over a large wavelength band (1520 nm to 1610 nm) with the application of a voltage in the range of 0-36V. The optical sensor reflection from a superluminescent diode (SLD) is filtered by the MEMS device allowing only a 60 pm window of optical power at any instant. As the MEMS device is tuned across the wavelength band the complete spectrum from the optical sensor can be constructed. Figure 6.3 shows a picture of the high speed FSIM.

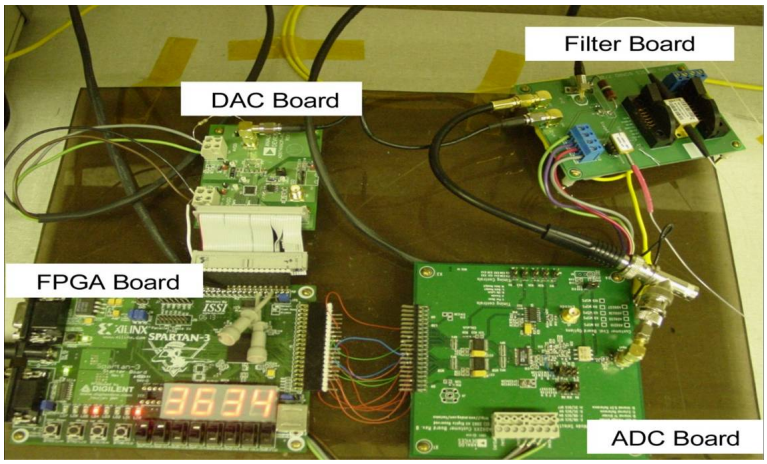

Figure 6.3: Picture of the high speed FSIM.

Figure 6.4 shows the spectrum as recorded from the FSIM. The spectrum on the left shows high frequency noise on top of the spectrum envelope. The noise is most likely noise from the op-amps used in the FSIM circuitry. Because the FSIM is a research project in progress parts of the circuit are still laid out on bread boards which often leads to high amounts of noise. In order to deal with the noise, the reflection spectra are first captured using the FSIM and then de-noised in MATLAB. The right spectrum shows the reflection spectrum from the SR-FBG captured with the FSIM and de-noised during post processing.

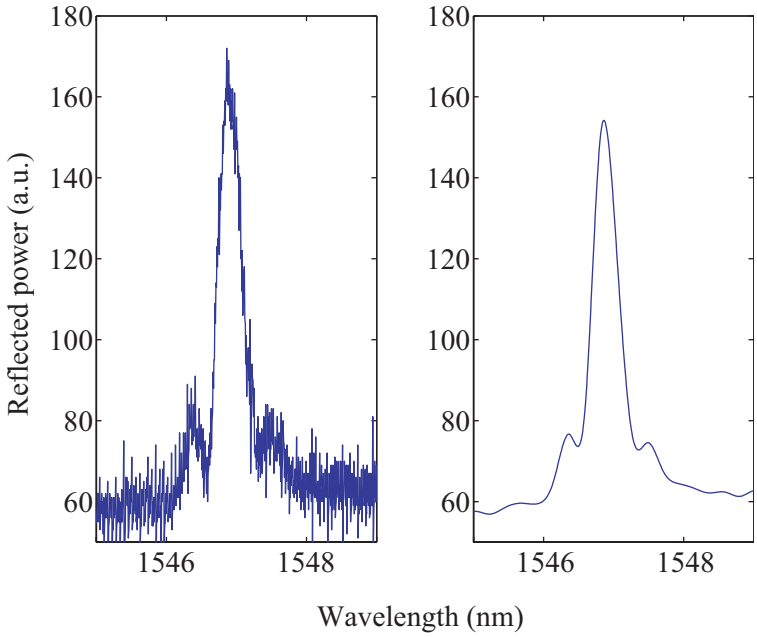

Figure 6.4: Reflection spectrum from a SR-FBG captured with the FSIM. The spectrum on the left shows the spectrum captured with high frequency noise. The right spectrum shows the spectrum after it has been filtered during post processing in MATLAB.

6.2 Experimental Setup

In order to use the SR-FBGs for temperature response tests, the specific grating used for the test is first calibrated to temperature changes in a small table top tube furnace. The reflection spectrum from the grating is monitored along with the furnace temperature as the grating is heated from room temperature to 400°C. The calibration temperature range is chosen such that a good fit is established without compromising the integrity of the optical fiber which occurs when the fiber is at high temperatures (>800°C) for prolonged periods of time [48]. Figure 6.5 shows the change in the peak Bragg wavelength as a function of temperature. The dots on the graph are the recorded data and the solid line is a quadratic fit to the data that is used as a calibration curve for the high speed, high temperature tests. While a linear fit is mostly accurate for small temperature ranges, it is shown that a quadratic fit to the data is more reliable due to the thermo-optic coefficient of fused silica glass [45].

Figure 6.6 shows the experimental setup used to characterize the temporal response of the SR-FBG to high temperature changes. A CO_2 laser is chosen as the heating source because it can be accurately controlled to approximate a step function when heating or cooling the fiber. Also because the lasing wavelength is in the far infrared, $\lambda_{laser} = 10.6$ μm, the fused silica fiber absorbs almost all of the incident radiation and extreme temperatures are achieved.

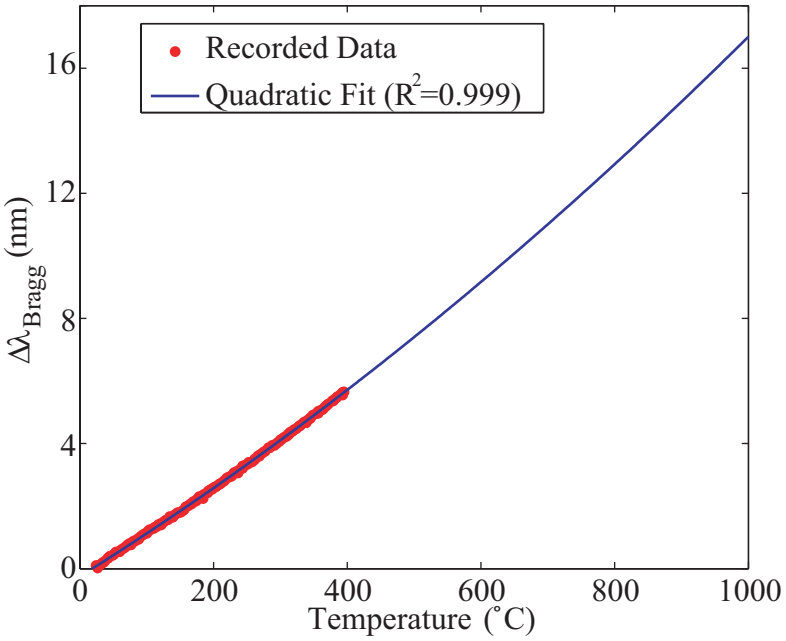

Figure 6.5: Graph showing the change in the peak Bragg wavelength versus temperature during the grating calibration. The dots are the recorded data and the solid line is the quadratic fit.

The light from the laser first passes through a spherical lens with a focal length of 38.1 cm. The beam is turned using two flat mirrors in order to increase the path length and allow for sufficient divergence of the incident beam. The diverging beam is focused down to a line using a cylindrical lens with a focal length of 15.24 cm. The SR-FBG is placed at the focus of the cylindrical lens to achieve maximum heating. The path length is such that the focused laser line is approximately 1 cm long when it reaches the SR-FBG.

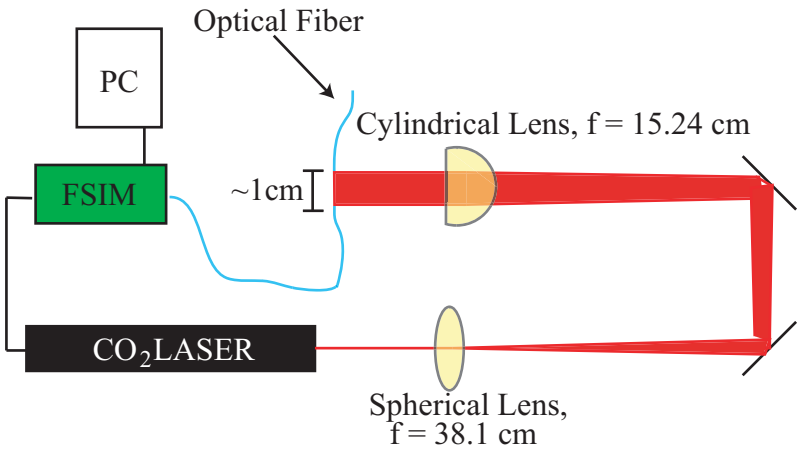

Figure 6.6: Diagram of the experimental setup to measure the temporal thermal response of the SR-FBG.

The optical fiber is attached taut at two points on either side of the SR-FBG causing the grating to be suspended in the air. This mounting method is chosen so that there is no residual heat by attaching the fiber directly to another material. The optical fiber and the mounting stage are attached to an x-y stage in order to precisely align the SR-FBG in the path of the incident laser radiation.

To ensure that the SR-FBG is heated uniformally by the laser source, the reflection spectrum from the grating is monitored in real time while adjusting the x-y stage. If the fiber is not heated uniformally then chirping occurs due to the non-uniform distribution of the effective index of the guided mode and the reflected spectrum broadens and becomes asymmetric [57]. By precisely adjusting the x-y stage nearly uniform heating occurs. To further assure that the grating experiences uniform heating the gratings used for the experiment are fabricated to be only 2 mm long. The FSIM is used to capture the reflection spectrum and to control the on-off pulse from the CO_2 laser.

6.3 Experimental Results

This section presents the results from various heating and cooling experiments with the SR-FBG. To quantify the results the collected data is fitted to an

exponential heating and cooling model. The temperature, T, as a function of time can be modeled as

$$T(t) = T_s + (T_0 - T_s)e^{\frac{-t}{\tau}}, \tag{6.1}$$

where T_s is the surrounding temperature and T_0 is the initial temperature of the fiber. A time constant, τ, can also be defined as the point at which heating reaches ~67% of its maximum value or the point at which cooling reaches ~67% of its starting value.

The time constant is mainly affected by the thermal mass of the sensor. Because the sensor is fabricated using an asymmetric D-fiber the heating time constant is variable depending on the orientation of the sensor with respect to the incident heating radiation. Therefore the asymmetric D-shape needs to be accounted for when quantifying the temporal thermal response.

6.3.1 Results for Different Sensor Orientations

The primary mechanism that causes the Bragg wavelength to shift as the grating is heated is the change in the effective index of the guided mode in the core of the fiber due to the thermo-optic effect. Because the gratings are fabricated using D-shaped optical fiber, the distance from the flat surface to the core is different when compared to the distance from the rounded side of the fiber to the core. This variation in distance creates a difference in thermal mass depending on the directionality of the incident heat. To quantify this variation, the heating time constant is found when the SR-FBG is oriented such that the flat side is toward the incident laser radiation and when the SR-FBG is oriented such that the round side is toward the incident radiation.

To heat the fiber the FSIM captures two complete spectra and then turns the laser on for ~700 ms. During this time the FSIM continues to capture the reflection spectrum until the fiber is heated to a steady state level. The reflection spectra are then post processed to find the peak of the Bragg reflection. These peak wavelengths are converted into temperature measurements using the calibration curve shown in Figure 6.5.

Figure 6.7 shows the results of heating the fiber for both flat side incident and round side incident heating tests. The squares on the graph are the collected data when the laser radiation is incident on the flat side of the fiber and the triangles are the collected data when the laser radiation is incident on the rounded side of the fiber. The solid lines are fits to the data using the exponential heating and cooling model of Eq. 6.1. The final temperature values for the tests are slightly different most likely due to the fact that the fiber had to be realigned when changing the fiber from flat side forward to round side forward.

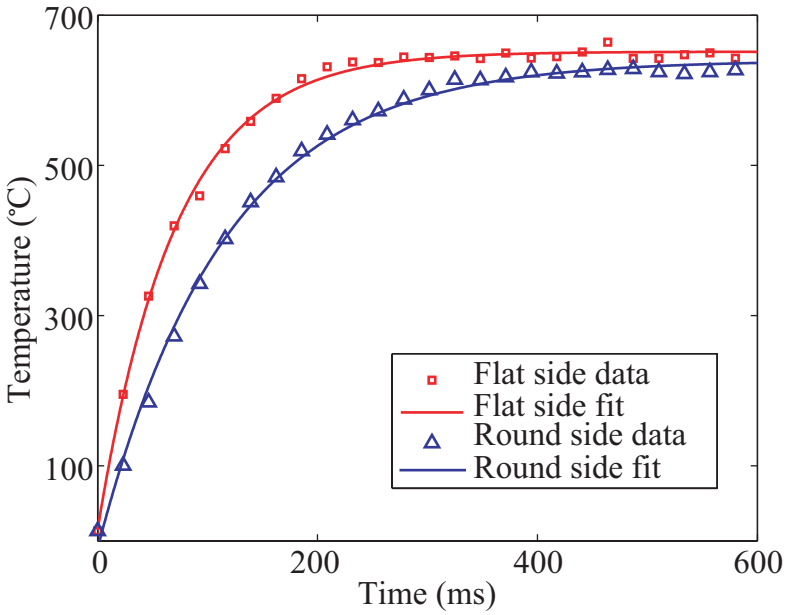

Figure 6.7: Graph showing the difference in heating times when the laser radiation is incident on the flat side or when incident on the rounded side of the D-shaped optical fiber.

Using the time constant as defined in Eq. 6.1, Figure 6.7 clearly shows that the fiber responds more quickly when the laser radiation is incident on the flat side of the fiber when compared to laser radiation incident on the round side of the fiber. The fiber responds more quickly because the distance from the flat side to the guided light in the core is minimized. The time constants for the flat side and

round side heating are τ = 76 ms and τ = 115 ms respectively. These results show that the grating responds approximately 40% more quickly when heated from the flat side of the fiber. In a situation where the heating occurs more isotropically, the time constant is expected to be somewhere between these two extreme values. In fact, the thermal difussivity of an optical fiber is measured to be 1.21x10^{-7} m^2/s [58]. Given the cross sectional area of a D-fiber, the thermal diffusion is calculated to be about 95 ms which is approximately half way between the time constants of 76 ms for flat side heating and 115 ms for round side heating.

6.3.2 Heating and Cooling Experimental Results

To demonstrate the grating response to different levels of heating the output power from the CO_2 laser is varied and the reflection spectra recorded. Figure 6.8 shows the grating temperature as a function of time for several different output powers. The maximum experimental heating is about 1200°C which occurs when the output laser power is approximately 9 W. The time constant for heating the grating is found to be similar independent of the final temperature. This time constant is measured to be τ=77$\pm$3 ms.

For the cooling tests the laser radiation is initially on until the fiber temperature reaches a steady state. Once steady state is achieved the FSIM begins to capture reflection spectra and the laser is turned off. With the laser off, the fiber begins to dissipate heat back to the surrounding media (air) and return to room temperature. Figure 6.9 shows the results of starting the fiber at various initial temperatures and allowing the fiber to cool down to room temperature.

Again the time constants are found to be similar independent of the initial fiber temperature. The time constants are measured to be τ=143$\pm$10 ms. The time constants are slower for cooling when compared to heating because the heat dissipates isotropically away from the fiber. The difference in heating and cooling time constants is unique to the asymmetric D-shape of the optical fiber and would not be seen in a symmetrical round shaped optical fiber.

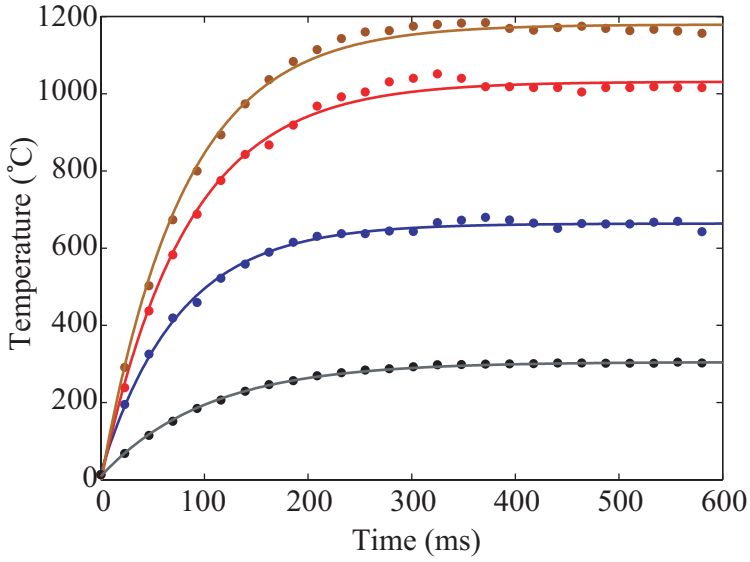

Figure 6.8: Graph showing different heating curves for the SR-FBG as a function of time. The different curves correspond to different output powers from the laser and thus different final temperatures. The time constant is τ=77±3 ms.

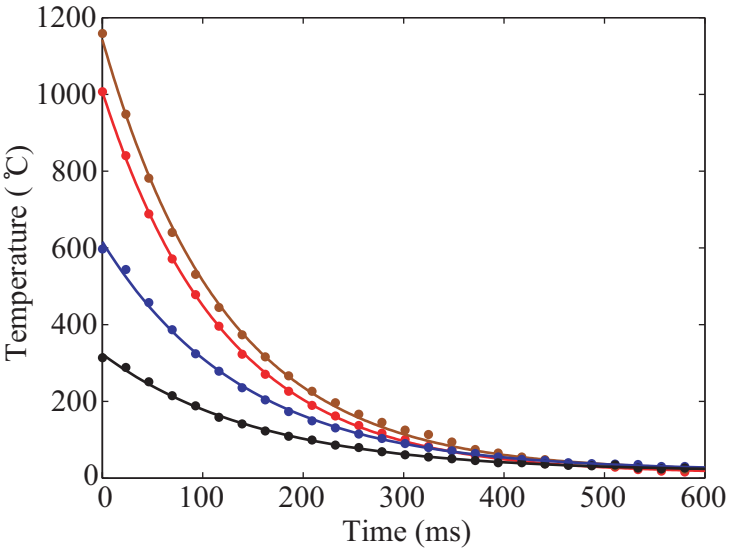

Figure 6.9: Graph showing different cooling curves for the SR-FBG as a function of time. The time constant is τ=143±10 ms.

In addition to measuring the temperature response of the grating at high speed, the FSIM's capability of capturing and storing full spectral scans allows for further analysis that would not be possible with traditional optical interrogator systems. For example, the full-width half-maximum (FWHM) of the reflected signal could be analyzed to show if the fiber is uniformly heated. Figure 6.10 shows the FWHM of the Bragg reflection as the grating is heated. The small variation indicates that the fiber experiences nearly uniform heating during the experiments. The evolution of the FWHM would not be captured using traditional interrogation systems and vital information would be lost.

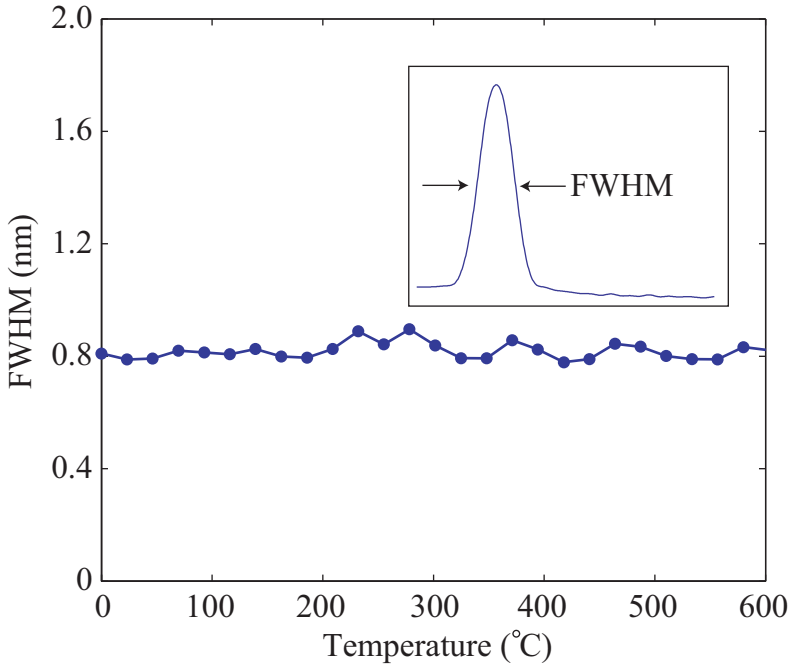

Figure 6.10: Graph showing the FWHM of the Bragg reflection as a function of temperature during one of the heating experiments. The inset shows the location of the FWHM on the reflection spectrum.

On the other hand, Figure 6.11 shows the reflection spectra when the fiber is not heated uniformly. The figure shows that as time progresses the reflection spectrum widens and additional features become evident. This widening of the spectrum

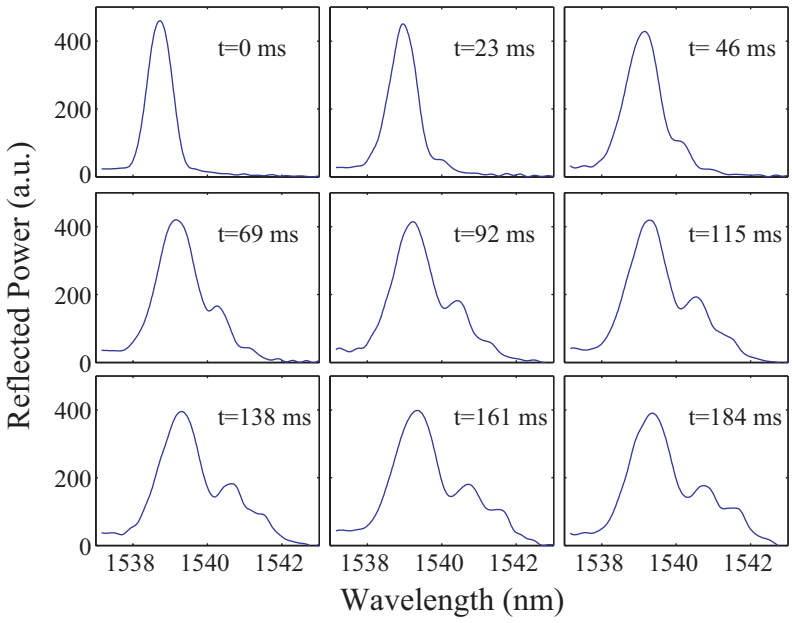

Figure 6.11: First nine reflection spectra captured with the FSIM while heating the edge of grating.

(known as chirping) indicates that the temperature distribution across the grating is non-uniform and a temperature gradient is created [57]. The evolution of the grating chirp would not be captured using traditional interrogation systems and vital information would be lost. Due to the unique capabilities of the FSIM, the full spectral response is recorded and the propagation of the heat pulse is observed. This data could be further post processed using inverse scattering techniques to extract the full temperature profile across the grating [59].

6.4 Summary

This chapter demonstrates that a SR-FBG along with the FSIM monitor form a complete system which is able to monitor non-steady state high temperature conditions at high speed. The dynamic thermal response is important to measure in order to better understand the inner workings of a given system. The SR-FBG provides a sensor that is able to withstand harsh high temperature environments while at the same time responding quickly enough to temperature fluctuations. The FSIM provides a system that is able to interrogate the sensor and stores the data

at more than sufficient speeds such that additional information can be gained that would be lost otherwise.

Chapter 7

A Volatile Organic Compound Chemical Sensor

Another sensor is developed for this dissertation that monitors volatile organic compound (VOC) chemicals. Interest in chemical and biological sensors has increased ever since the September 11^{th} attacks on the World Trade Center in New York City. The need for reliable sensors increases as the threat of chemical and biological attacks also increases.

The private sector also has an increasing interest in chemical sensing applications. Industries that use dangerous chemicals during fabrication processes can benefit from the knowledge of a good monitoring system. Safety and process yield increases as information about these dangerous chemicals is obtained. Whether it be for the military or private sector, small and reliable sensors that are easily transportable are essential as people are put into ever increasing dangerous situations.

In this chapter, the SR-FBG developed in this work is used as a chemical sensor. Specifically, the SR-FBG with the addition of a polymer sensing layer is presented as a volatile organic compound (VOC) chemical sensor. The need for such a sensor is discussed along with a discussion of current technology that meets this need. The deficiencies in these technologies is noted and the SR-FBG VOC sensor is shown to alleviate some of these short comings. Changes to the general fabrication process for SR-FBGs are discussed and experimental verification of the completed VOC sensor is given.

7.1 Need for VOC Sensors

VOCs are valuable in many industrial and academic settings but often raise environmental and health related concerns. For example, chlorinated hydrocarbons (CHCs) are often used as cleaning solvents but have significant ozone depleting potential. In addition, many CHCs are known human carcinogens, requiring restrictions to their use. Through monitoring the concentrations of VOCs in either gas or liquid forms, VOC sensors can help maintain human and environmental safety. In addition, chemical concentration data acquired through the sensors can be applied to process control systems to improve product quality and yield [60].

7.2 Fiber Optic Based Chemical Sensors

Fiber optic based chemical sensors provide in-situ remote monitoring of VOC concentrations in liquid or gaseous forms. The small size and ease of integration with electronic systems allows the fiber optic chemical sensor to be placed in extremely small and remote areas. Fiber optic chemical sensors are also chemically inert to a wide range of hazardous chemicals. These sensors can be used to monitor several concentrations of VOCs throughout an array of sensing locations, providing detailed and accurate monitoring of VOC concentration levels.

Usually there are two methods for which optical fibers are deployed as chemical sensors. The first method uses a chemically selective polymer as a cladding layer to change the absorption and transmission properties of the guided light as different chemicals are absorbed into the cladding layer. The second method uses FBGs that are etched down such that the evanescent field of the guided mode interacts with the surrounding refractive index. Both methods have advantages and disadvantages which are individually discussed in the next sections.

7.2.1 Non-FBG Based Fiber Optic Chemical Sensors

In order for a fiber-optic chemical sensor to distinguish chemical concentration levels, the chemical of interest must interact with the light traveling through

the fiber. However, optical fibers are generally not chemically sensitive without modification. Some fiber-optic chemical sensors use a selective polymer to interact with the desired chemical. Placing a chemically selective polymer film in the evanescent interaction region of the optical waveguide mode provides the basis for a chemical sensor [61]. Polymers compatible with optical fiber are required to have low optical loss and a relatively low refractive index. To maintain beam transmission through the fiber, the film must have a lower index than that of the fiber core.

Several reusable fiber-optic chemical sensors are demonstrated that use a selective polymer to absorb analyte chemicals of interest [62, 63, 64]. The changes in the polymer's refractive index and absorption spectra are dependent on chemical type and amount absorbed. Conzen et al. report on a fiber-optic evanescent-wave absorbance sensor based on a PDMS clad fiber [62]. Changes of refractive index in the polymer cladding resulting from analyte absorption are observed as both a change in transmitted power and a change in the absorption spectrum of the transmitted light. These types of sensors, however, require a long fiber length, resulting in an average response over a relatively large region. Also, the sensor can only be effective in sufficiently large analyte volumes.

Klunder et al. demonstrate a core-based intrinsic fiber sensor where two fiber ends are coupled into a solid cylinder of PDMS [65]. Chemical absorption into the PDMS is similarly monitored as a change in absorption spectrum of the transmitted light. Although the sensor itself is relatively small, this sensor requires the light to leave the fiber completely, travel through the PDMS block, then couple into another fiber. This coupling requirement results in optical transmission loss and limits sensor strength by the lack of strong adhesion of the polymer to the small fiber tip. In addition, bending the fiber at the sensor region may significantly increase the loss, requiring a bulky holder to maintain linear geometry of the entire sensor region. The sensors response times are relatively long, taking several minutes for the sensor to reach 90% of its equilibrium response.

7.2.2 FBG Based Fiber Optic Chemical Sensors

Many recent papers have been published on the use of fiber Bragg gratings (FBGs) as fiber optic chemical sensors [66, 67, 68]. FBGs are attractive because the sensing response is wavelength encoded making fluctuations in input power irrelevant, and they are easily multiplexed to create sensor arrays. They are also small enabling point detection of the chemical being sensed. These papers demonstrate excellent sensitivity to changes in the surrounding refractive index (SRI) by monitoring shifts in the Bragg wavelength. Nevertheless, further research is needed to create a link between changes in SRI and chemical sensing. Without the ability to detect and classify specific chemicals, the FBG, by itself, is inadequate as a chemical sensor.

In order to create the link between changes in SRI and chemical sensing and overcome the limitations of the previous fiber optic based chemical sensors, a fiber optic chemical sensor is presented using a SR-FBG fabricated with D-fiber and a thin layer of a chemically selective sensing material. The primary contribution of this chapter is combining the SR-FBG with a material that is (1) compatible with the optical properties of the SR-FBG and (2) exhibits good chemical selectivity. Polydimethylsiloxane (PDMS) satisfies both of these requirements because it has an index of refraction (n$\sim$1.41) that is lower than that of the optical fiber core, is optically transparent at the operating wavelength, and is only sensitivity to a specific class of chemicals, namely VOCs [62, 63, 69].

7.3 Properties of Polydimethylsiloxane

For the chemical sensor, a layer of PDMS is placed on the D-fiber flat. Since the index of refraction of PDMS is lower than that of the fiber core, beam transmission is maintained. PDMS also has good spectral transmission in the near-infrared range, and high chemical, mechanical, and thermal stability.

The PDMS membrane exhibits selective transport for organic molecules with respect to polar molecules such as water and low molecular-weight gases such as nitrogen, oxygen, and helium [70]. In addition, PDMS is more penetrable to large,

hydrocarbon-based VOCs than to small molecules [71]. The polymer maintains its selective transport properties in both liquid and gaseous environments.

The sorption of analyte molecules into the PDMS layer leads to a change of refractive index. The new refractive index can be higher or lower than the original refractive index, depending on the refractive index of the analyte. In addition, the change in refractive index of the polymer is dependent on the amount of analyte absorbed [72]. When placed in contact with a VOC, the PDMS absorbs the VOC until an equilibrium is reached. That equilibrium is dependent on the VOC concentration and its solubility in PDMS. Lee et al. report solubility parameters for 38 organic solvents [73]. Contributors to each solubility parameter includes dispersion forces, polar forces, and hydrogen-bonding forces within the material. The amount of analyte absorbed into the PDMS membrane, as well as the amount of swelling due to sorption is dependent on the analytes solubility parameter.

As the VOC is absorbed, the index of refraction of the PDMS changes to more closely match the refractive index of the analyte [72] which results in a Bragg wavelength shift to longer or shorter wavelengths depending on the absorbed VOC's refractive index. Furthermore, the change in refractive index of the PDMS, and thus the shift in Bragg wavelength, depends on the solution concentration. These unique properties of the PDMS/SR-FBG sensor mean that specific chemicals can be identified and chemical concentration can be determined.

7.4 SR-FBG Response to SRI Changes

Unlike standard UV-written FBGs, where the index modulation is small and occurs in the core of the fiber, the index modulation of a SR-FBG occurs on the flat surface of the fiber and results from the cladding-air structure. The efficiency of the Bragg reflection is related to this index contrast. Figure 7.1 shows that as the SRI approaches the index of the cladding the reflectivity of both modes decreases. In order to maintain a highly reflective grating a thin, high index buffer is placed between the grating and the PDMS layer. Using E-beam evaporation $\sim$80 nm of sapphire (Al_2O_3) is deposited over the grating to provide a buffer and maintain the index contrast.

To test the SR-FBGs response to changes in SRI, a grating is immersed in various index matching oils purchased from Cargille Labs while monitoring the Bragg wavelength shift. Because the core of the D-fiber is elliptical two orthogonal modes are supported and two reflection peaks occur due to the different effective indices of the two modes. Figure 7.2 shows the shift in Bragg wavelength for both horizontal (polarized along the major axis of the core) and vertical (polarized along the minor axis of the core) modes as a function of SRI. The figure also shows the shift in Bragg wavelength calculated using the commercially available software package BeamPROP^{TM} to find the effective indices of the modes given different SRIs.

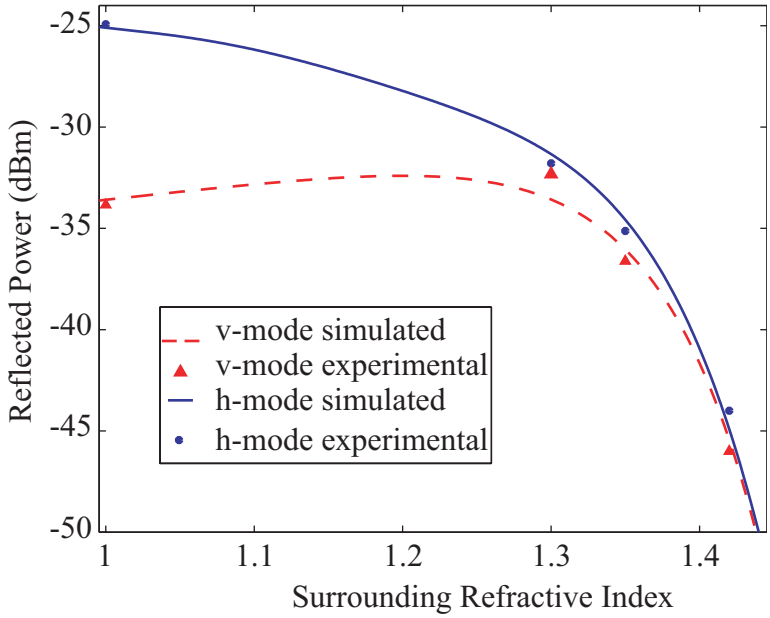

Figure 7.1: Graph showing the reduction of grating efficiency when the SRI is increased to match the cladding layer.

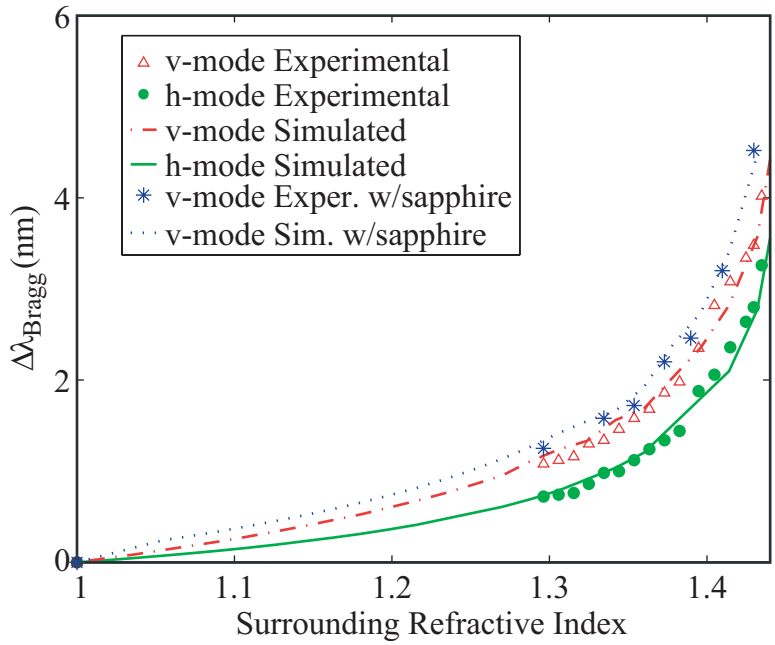

Figure 7.2: Change in Bragg wavelength for both the horizontal (h-mode) and vertical (v-mode) modes as a function of SRI. The shift in Bragg wavelength is also shown for the vertical mode for a grating coated with sapphire.

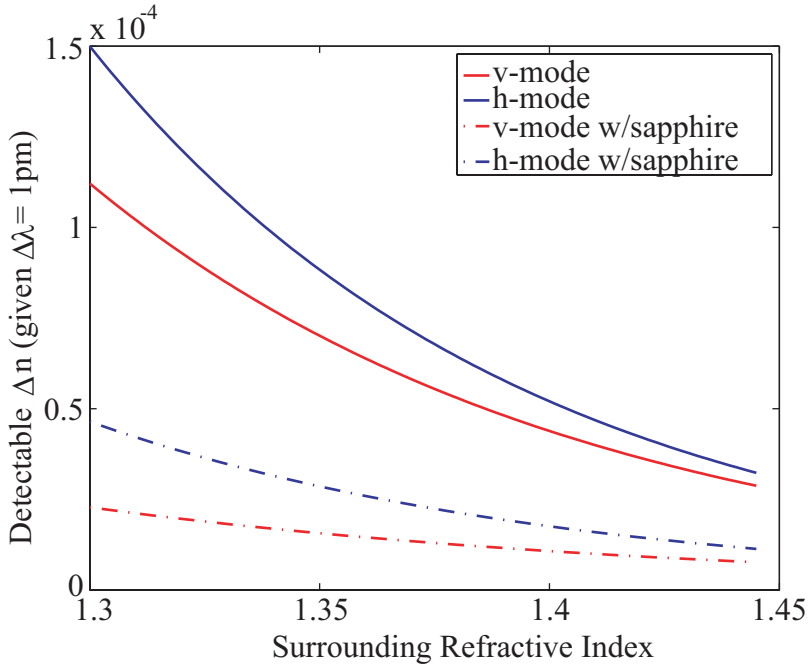

Figure 7.3: Graph showing the detectable change in SRI vs. SRI for a given detector resolution.

An additional advantage to using the sapphire buffer is an increased response to changes in SRI. Figure 7.2 shows this increase in sensitivity for the vertical mode. The sensitivity to changes in SRI can be quantified by taking the derivative of the change in Bragg wavelength with respect to the surrounding refractive index. This process yields a detectable change in SRI (Δn) for a given detector resolution ($\Delta\lambda$). Figure 7.3 shows the sensitivity for both the horizontal (h-mode) and vertical (v-mode) modes for both the uncoated and sapphire coated gratings. The increase in sensitivity is most likely due to more of the field being pulled up towards the higher index sapphire and creating a larger overlap with the surrounding media. The sensitivity increases by about a factor of two when compared to the non-sapphire coated grating. The wavelength shifts are comparable to other FBG refractive index sensors [66, 67, 68]. The SR-FBG has a sensitivity to changes in SRI of $\sim 10^{-5}$ assuming a wavelength resolution of 1 pm.

7.5 Sensor Fabrication

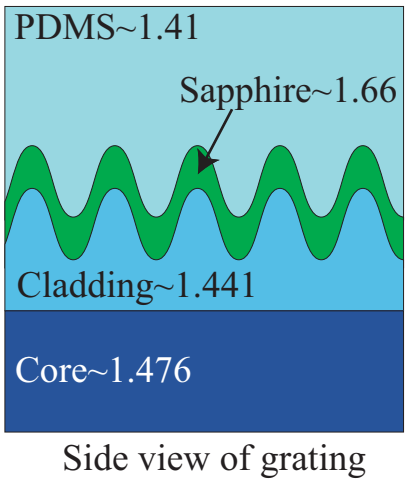

Figure 7.4: Drawing of the side view cross section of the completed VOC sensor coated with sapphire and PDMS.

Figure 7.4 shows a cross section of the VOC sensor and Figure 7.5 shows the additional fabrication steps. The completed sensor consists of a SR-FBG that is 1.5 cm long with ∼80 nm of evaporated sapphire and ∼2 μm of spun on PDMS. The copolymer is mixed in a 10:1 base to curing agent ratio (by weight) and degassed for approximately 45 minutes before application to the grating region of the fiber. The SR-FBG is mounted to a silicon wafer and the PDMS is spun on for 1 minute at 4000 rpm to create the sensing layer on the grating surface. The wafer is baked at 110°C for 1.5 hours and stored at room temperature for an additional 24 hours to promote the cross linking of the polymer.

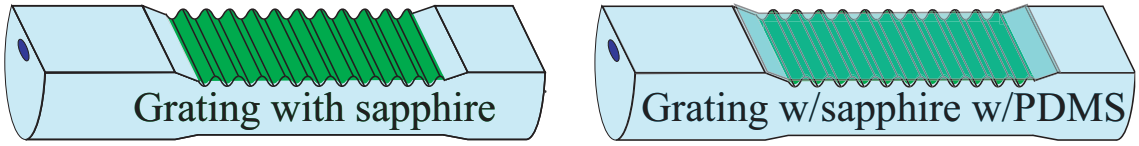

Figure 7.5: Drawing of the two additional steps to complete the VOC sensor.

7.6 Experimental Verification

To test the sensor the reflection spectrum from the grating is monitored using a Micron Optics sm125 sensing interrogator while changing VOC concentrations. Figure 7.6 shows the reflected horizontal and vertical modes of the completed sensor. The insertion loss of the completed sensor is less than 1 dB. Either reflection peak could be monitored for changes in wavelength; however, based on Fig. 7.3 it is found that the vertical mode is slightly more sensitive to changes in SRI.

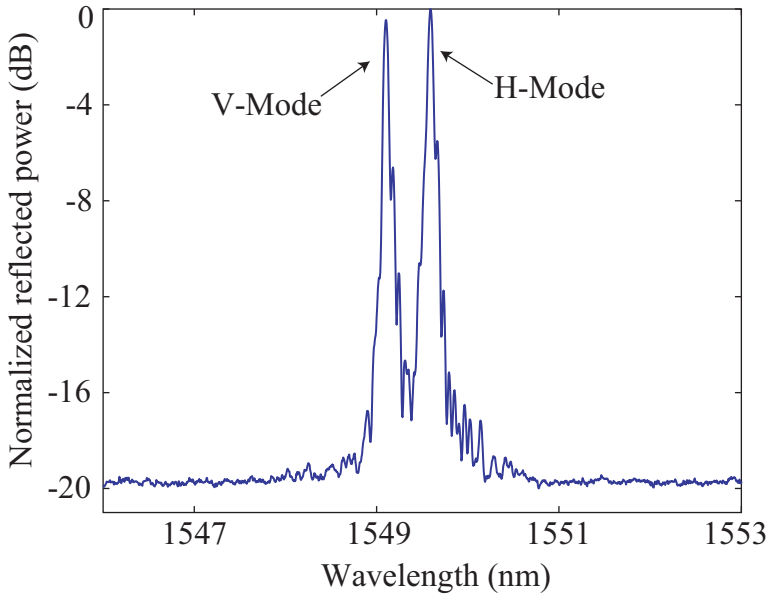

Figure 7.6: Reflection spectrum from the SR-FBG with the ∼80 nm of deposited sapphire and ∼2 μm of spun on cured PDMS.

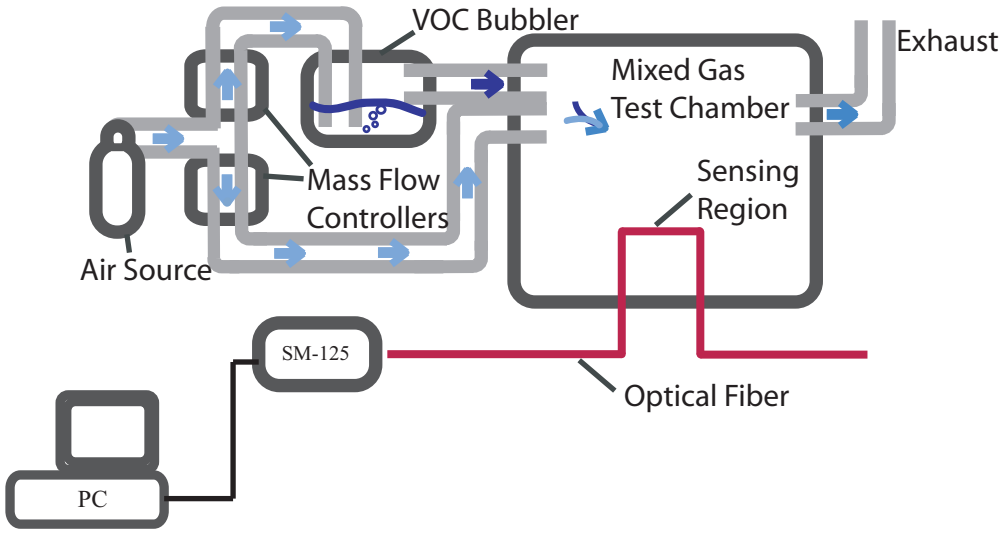

Figure 7.7: Schematic showing the experimental setup used to test the sensor's response to gas VOC concentration levels.

The sensor is tested for response to gas VOCs. Response is recorded for several gas-phase concentrations of dichloromethane (obtained from Fisher Scientific) and acetone (obtained from Mallinckrodt Chemicals). Dichloromethane is chosen for the experiment because of its reported high solubility in PDMS [73] and acetone is chosen to demonstrate the directionality of the Bragg wavelength shift. As explained earlier, the PDMS changes refractive index to more closely match the refractive index of the absorbed analyte. Dichloromethane has a slightly higher index than the PDMS resulting in a longer wavelength shift, while acetone has a lower index than the PDMS causing the Bragg wavelength to shift to shorter wavelengths.

Figure 7.7 shows the setup used to test the response of the sensor to changes in VOC concentration. The concentration of VOC, in dry air as a carrier gas, is regulated by a pair of mass flow controllers. The two mass flow controllers, one for air only, and one for an air/VOC mixture varies in flow contribution to create various mixtures but as a pair maintain a total flow of 10 liters/min. The air/VOC mixture is created through use of a bubbler, where temperature is monitored to calculate vapor pressure and concentration levels. Various flow ratios of analyte/air concentration and air only are flowed into a plastic 3.712 liter test chamber containing a small mixing fan and the sensor. The temperature in the chamber is also monitored so that any shifts in Bragg wavelength due to temperature fluctuations can be subtracted from the total change in wavelength.

Figure 7.8 and Figure 7.9 show the shifts in the Bragg wavelength versus time for dichloromethane vapor and acetone vapor respectively. The arrows on the graph indicate the time when the concentration level of the VOC is increased inside of the mixing chamber. After each increase in VOC concentration the Bragg wavelength shifts and settles within a matter of seconds indicating the fast response time of the sensor. Also when the VOC is evacuated from the chamber, the Bragg wavelength shifts back to its original wavelength indicating that the sensor can be used repeatedly.

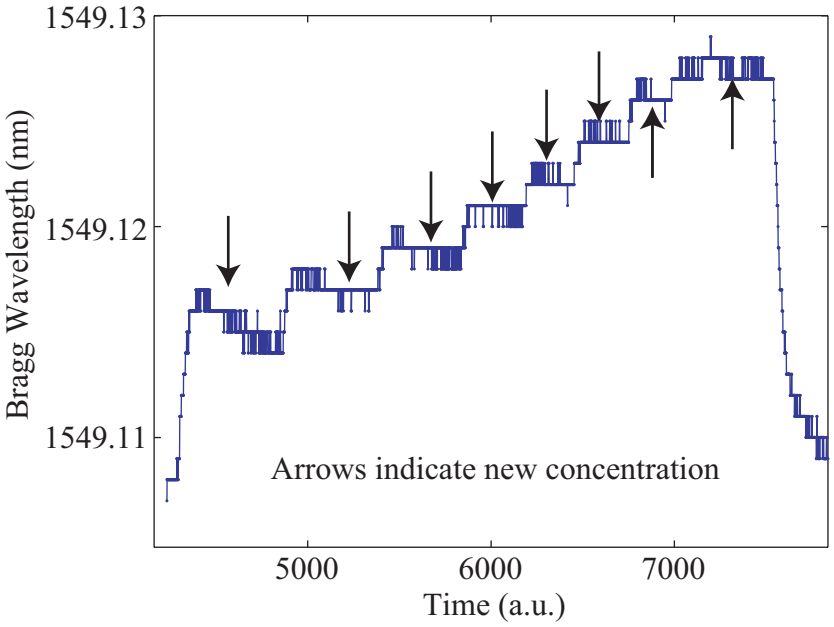

Figure 7.8: Graph showing the shift in Bragg wavelength to longer wavelengths versus time as new concentration levels were introduced into the gas chamber. The arrows indicate the time when the concentration level increased.

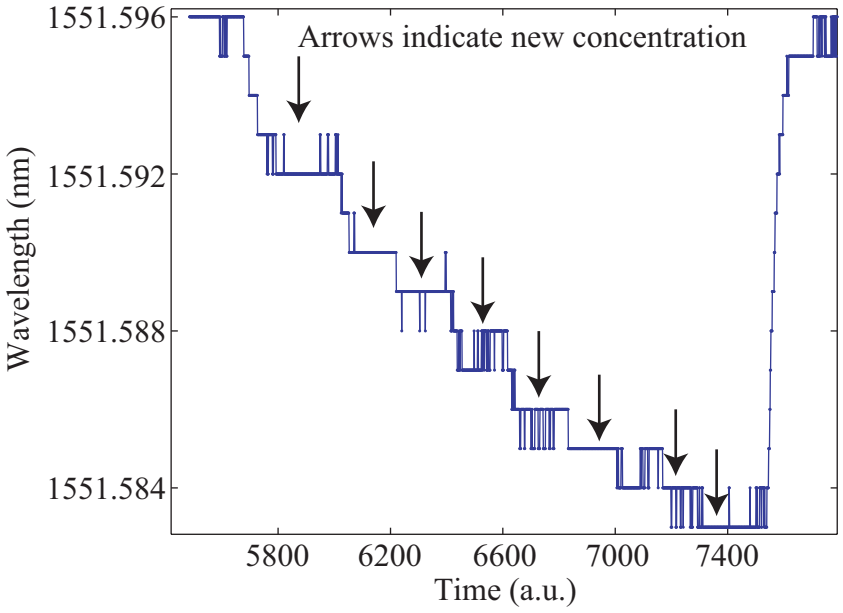

Figure 7.9: Graph showing the shift in Bragg wavelength to shorter wavelengths versus time as new concentration levels were introduced into the gas chamber. The arrows indicate the time when the concentration level increased.

Figure 7.10 shows the Bragg wavelength shift in picometers (pm) as a function of VOC concentration in parts per million (ppm). The lines on the graphs are linear fits to the data for both the dichloromethane and acetone experiments. The response is linear as is expected for small changes in SRI. The slope of the fitted line for the dichloromethane is 2.38x10^{-4} pm/ppm and the slope of the fitted line for the acetone is -1.65x10^{-4} pm/ppm. The resolution of the sm125 interrogator is 1 pm, therefore, the sensors sensitivity to dichloromethane is ∼4000 ppm and its sensitivity to acetone is ∼6000 ppm. These sensitivities could be improved upon by optimizing the PDMS thickness on the grating such that the maximum amount of field interacts with the PDMS while at the same time isolating the field from the environment above the sensing layer. The key feature is that different chemical species are identified by their respective wavelength shifts.

Multiple tests show that the results are repeatable. After each experiment the VOCs are evacuated from the test chamber and the Bragg wavelength shifts back to its original wavelength indicating that the sensor does not experience any hysteresis.

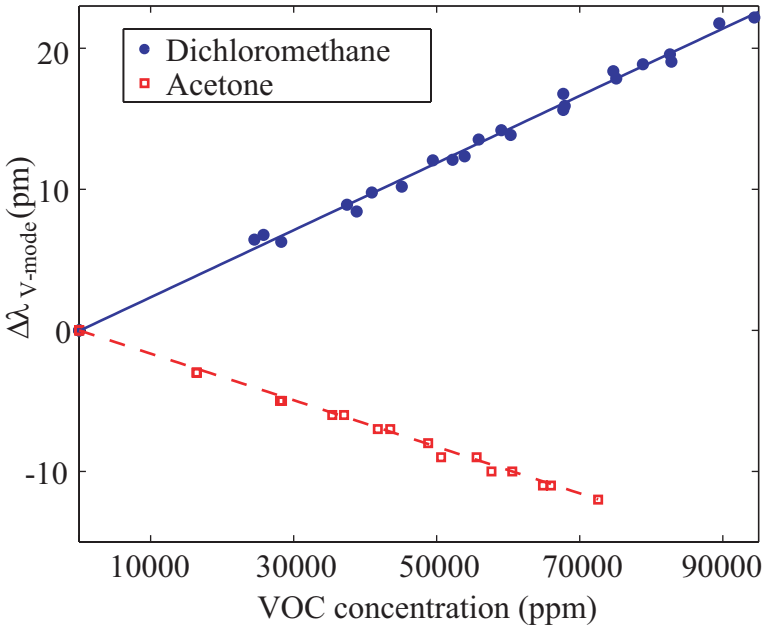

Figure 7.10: Graph of the Bragg wavelength shift as a function of VOC concentration for both dichloromethane and acetone.

7.7 Summary

The VOC gas response in Figure 7.10 highlights the sensing potential for the SR-FBG chemical sensor. It is possible to know concentrations of various VOCs real-time in small areas. Additionally, because the Bragg wavelength shifts to longer or shorter wavelengths depending on the absorb analyte, chemical identification is also a possibility. The PDMS/SR-FBG sensor exhibits rapid response times to changes in VOC concentration when compared to existing optical fiber chemical sensor technology. Also, because the Bragg wavelength returns to its original wavelength after the VOC is evacuated, the sensor can be repeatedly used saving the user time and money.

Chapter 8

Multi-Dimensional Bend Sensor

In addition to the sensor applications already discussed in this dissertation, SR-FBGs can also be used to measure bend in two dimensions. Bending and curvature are important variables to measure in many engineering applications. Specifically it is often necessary to measure the bend to assess structural integrity [74]. The bending characteristics can also be used to deduce information about the shape of a particular object.

For many applications it is necessary to obtain the bending information in two or three dimensions. Several papers are published on using optical fibers to obtain the multi-dimensional information, but they often employ specialty mutli-core fiber or complex interrogation schemes [75, 76].

Due to the unique shape of the D-fiber and the location of the SR-FBG on the flat surface of the fiber multi-dimensional bend sensing is possible. Because the grating and the core of the D-fiber are asymmetrically located relative to the geometric center of the fiber, strain is induced at and along the grating thus changing the Bragg wavelength and the Bragg reflectivity when the fiber is bent [74]. By monitoring the shift in the Bragg wavelength and the change in Bragg reflectivity a simple two dimensional bend sensor is realized.

8.1 Principle of Operation

The strain at the grating can be calculated by,

$$\epsilon = \frac{1}{R} d, R \neq 0, \tag{8.1}$$

where ϵ is the strain, R is the radius of bending curvature, and d is the distance the grating is away from the neutral axis or geometrical center of the fiber.

Most standard FBGs are written in the core of a circular cladding fiber. Because the FBG is locate at the geometrical center of the fiber no strain is experienced at the grating and no sensitivity to bend is demonstrated. On the other hand a SR-FBG is fabricated using a D-shaped cladding fiber above the geometrical center of the fiber. Because the grating is above the center of the fiber the grating experiences strain as the fiber is bent according to Eq. 8.1. If the strain is uniform along the grating then the Bragg wavelength shifts due to a uniform change in grating period. If the strain is nonuniform then the the Bragg spectrum widens and the peak reflectivity decreases due to the nonuniform change in the grating period which creates a grating chirp [77].

8.1.1 Vertical and Horizontal Bending

Figure 8.1 illustrates the grating position with respect to the neutral axis of the fiber as the fiber is bent in both the vertical and horizontal directions. As illustrated, when the fiber is bending in the vertical direction the grating is located above the neutral axis of the fiber and thus experiences strain. On the other hand, when the fiber is bending in the horizontal direction the grating is along the neutral axis of the fiber and therefore experiences no strain and thus no shift in the Bragg wavelength.

In order to create a multi-dimensional bend sensor strain must be induced at the SR-FBG when bending in both the vertical and horizontal direction. To create strain when bending in the horizontal direction the fiber is attached at both ends of a hollow, flexible tube. By fixing the fiber at both ends the grating experiences uniform tensile strain when bending and the Bragg wavelength shifts. The uniform tensile strain is given as,

$$\epsilon_{tensile} = \frac{\Delta l}{l_0}, \tag{8.2}$$

where Δl is the fiber elongation and l_0 is the original length of the fiber between the two fixed points.

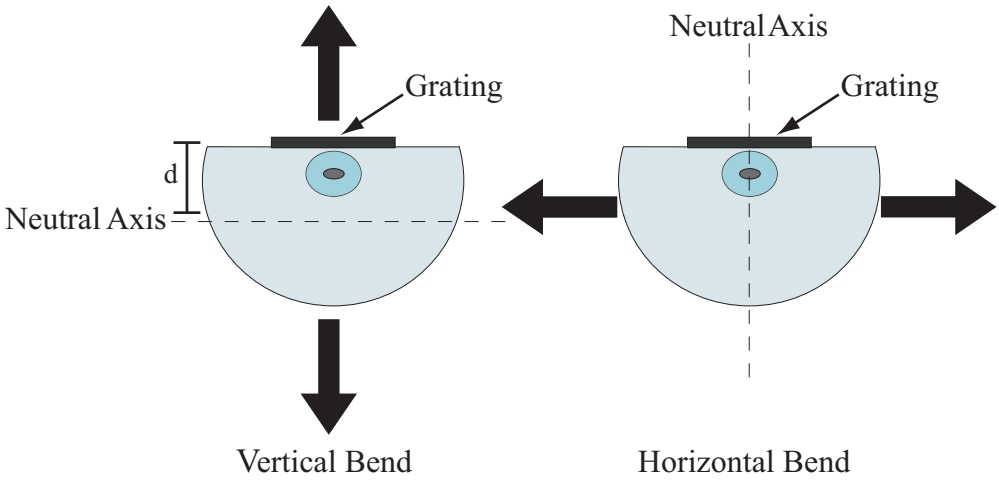

Figure 8.1: Illustration of the grating position with respect to the neutral axis of the fiber for both vertical and horizontal bends.

8.1.2 Determining Bend Direction

Distinguishing between the two directions of bend is possible because the grating experiences nonuniform strain when bending in the vertical direction and uniform tensile strain when bending in the horizontal direction. Because the grating is along the neutral axis of the fiber when bending in the horizontal direction, the strain due to horizontal bending, ϵ_{horz}, can be given as,

$$\epsilon_{horz} = \epsilon_{tensile}, \tag{8.3}$$

assuming that the fiber is fixed at both ends. The uniform tensile strain only causes the wavelength to shift.

The nonuniform strain experienced when bending the fiber in a vertical direction will not only cause the Bragg wavelength to shift but also causes the peak reflectivity to decrease. The strain distribution along the grating during a vertical bend can be approximated using,

$$\epsilon_{nonuniform}(x) \approx \frac{3z}{l^3}(l-x)d, \tag{8.4}$$

where again ϵ is the strain, x is the position on the grating, z is the end point displacement in the vertical direction, l is the length of the grating, and d is the

distance the grating is above the neutral axis of the fiber [77]. Therefore when bending the fiber in the vertical direction the total strain experienced by the grating, ϵ_{vert}, is given as,

$$\epsilon_{vert} = \epsilon_{tensile} + \epsilon_{nonuniform}, \tag{8.5}$$

To better demonstrate why the peak reflectivity decreases and the Bragg wavelength shifts Figure 8.2 illustrates the relationship between vertical deflection, nonuniform strain, and grating chirp. Figure 8.2(a) shows the fiber bending to three different positions. By bending the fiber further in the vertical direction Figure 8.2(b) shows that the strain gradient increases along the grating according to Eq. 8.4. The strain gradient creates a larger distribution in the grating period as demonstrated in Figure 8.2(c). Larger distributions in the grating period decrease the overall reflectivity by creating larger grating chirp. In the vertical bending situation the Bragg wavelength also shifts according to the average grating period plus the additional shift due to tensile strain assuming the fiber is fixed at both ends.

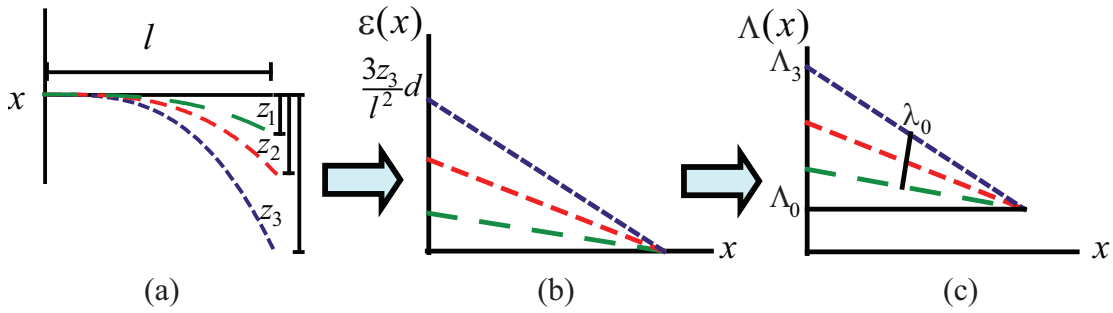

Figure 8.2: Illustration of the (a) the fiber bending vertically, (b) strain gradient produced, (c) and resulting non-uniform grating period when bending the fiber in a vertical direction.

Even though both horizontal and vertical bending directions cause the Bragg wavelength to shift they shift at different rates due to the different strain components. The different shift rates coupled with the changes in peak reflectivity make it possible to distinguish between the two dimensions of bend.

8.2 Experimental Setup

Figure 8.3 shows a drawing of the grating inserted into a tube and fixed at both ends with supper glue. The fiber is first inserted into a bendable tube to make it easier to handle. The anchor screws are used to hold the tube in place and to displace one end.

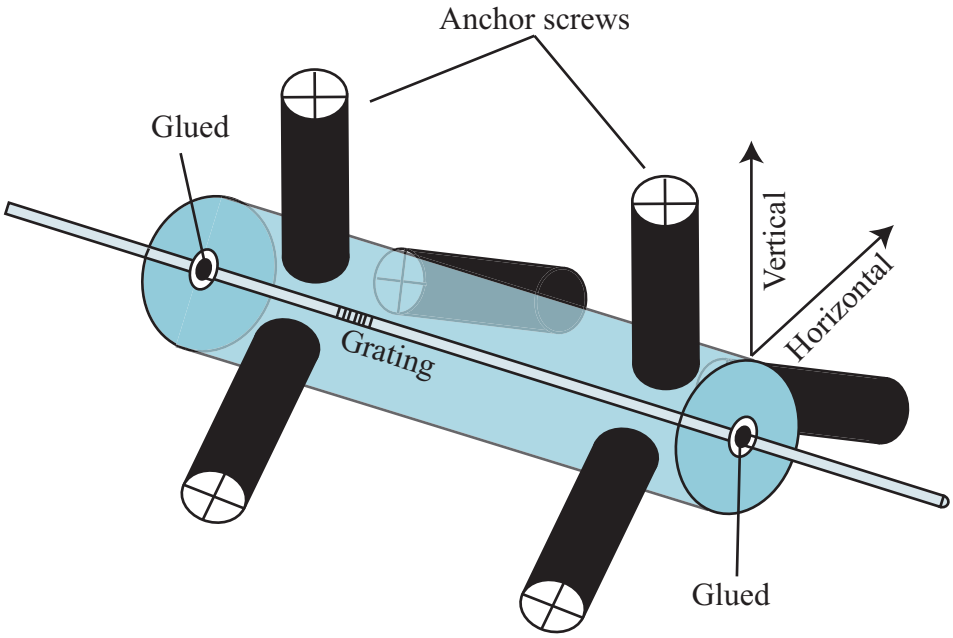

Figure 8.3: Illustration of the fiber inserted into a bendable tube and fixed at both ends with super glue.

8.2.1 Fiber Calibration

In order to determine the rates at which the Bragg wavelength shifts or decreases in reflectivity the fiber is packaged and fixed according to Figure 8.3. The tube and fiber are fixed into place at one end to an optical table and to micrometers on the other end for the purpose of creating displacement in two dimensions. The end of the fiber that is attached to the micrometers is initially displaced in both the horizontal and vertical direction so that bend direction can later be determined. This

new position is defined as the prebent resting position at $x = 0$ mm and $y = 0$ mm. A Micron Optics interrogator is used to track the peak wavelength and peak reflectivity. Figure 8.4 shows a photograph of the experimental setup.

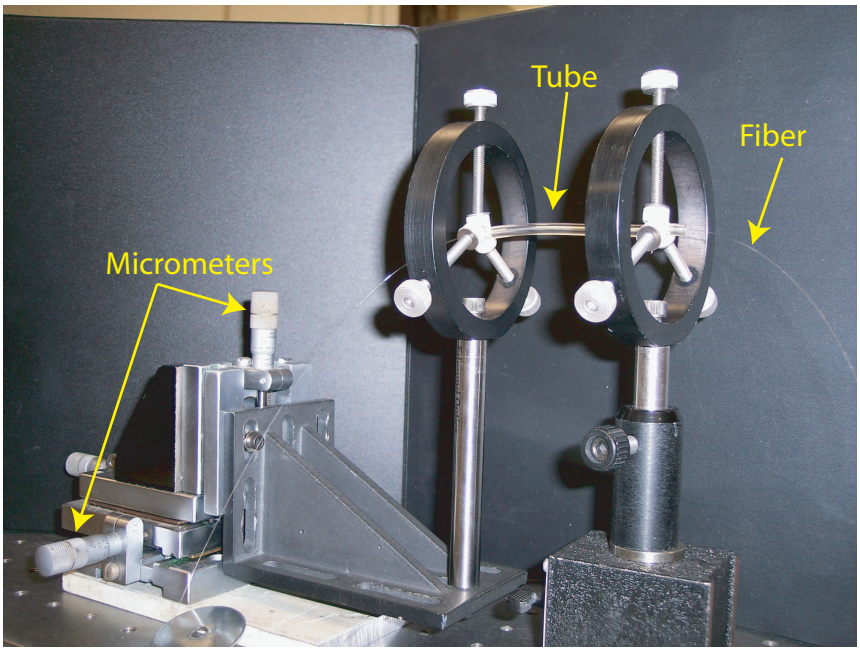

Figure 8.4: Setup used to calibrate and test the two dimensional bend sensing capabilities of the SR-FBGs.

By moving one end of the fiber through full vertical and horizontal displacement the rate at which the Bragg wavelength shifts or the peak reflectivity changes can be determined. These rates are determined by graphing the wavelength of the Bragg peak and the reflected power of the Bragg peak with respect to the micrometer displacement. The rates are then the slopes of the fitted data.

Figure 8.5 shows the reflection spectra from the grating when the end of the fiber is displaced in the vertical direction ± 5 mm from the prebent resting position. The red dashed spectrum on the graph is the reflection spectrum from the resting position. Because the tube is prebent the spectrum starts out chirped, due to the strain gradient, and the peak reflection power is lower than it would have otherwise

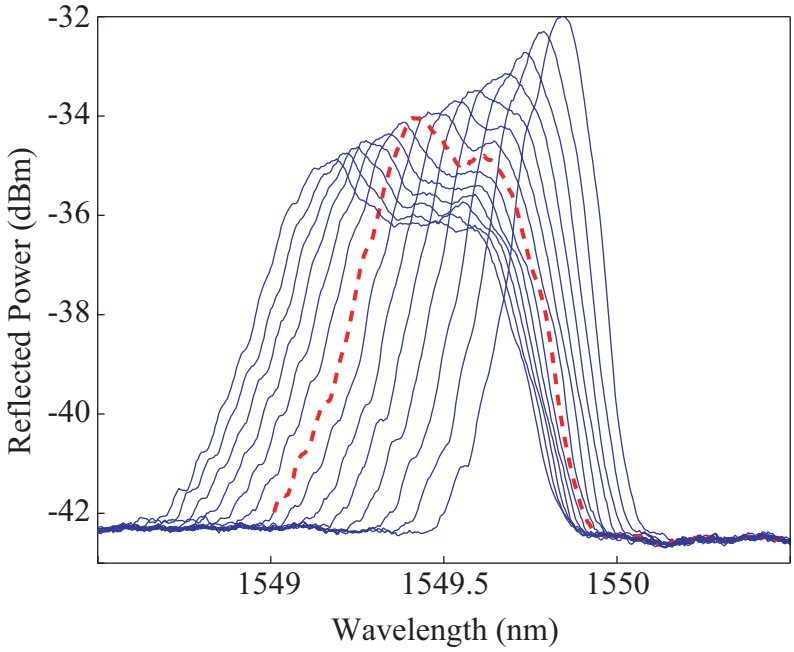

Figure 8.5: Graph showing the reflection spectra from the grating as the end of the fiber is displaced in the vertical direction. The red dashed spectrum is the reflection spectrum from the $y = 0$ mm prebent resting position.

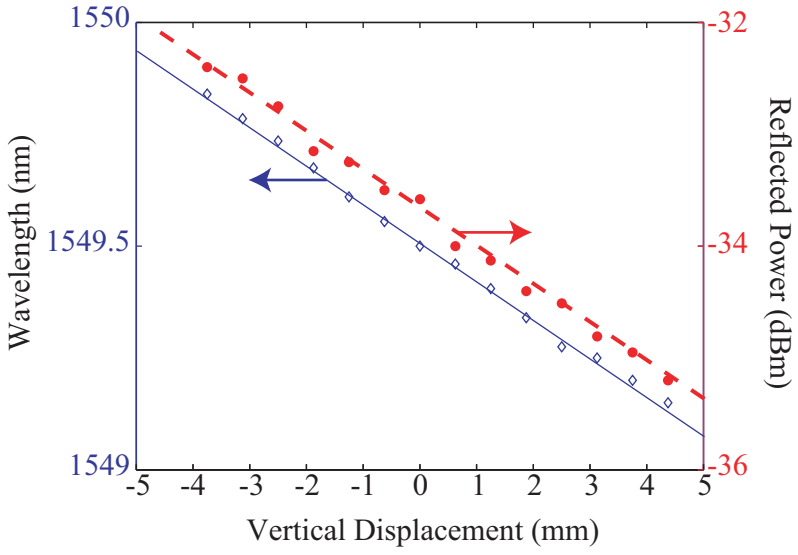

Figure 8.6: Bragg wavelength shift and change in reflected power for vertical displacement of the tube end.

been. The figure shows that as the end of the fiber is displaced the reflection power either decreases or increases and the peak wavelength shifts to lower or higher wavelengths. Figure 8.6 shows the shifts in Bragg wavelength and peak reflected power for vertical bending of the tube. The dots and diamonds on the graph are the collected data and the solid and dashed lines are linear fits to the data.

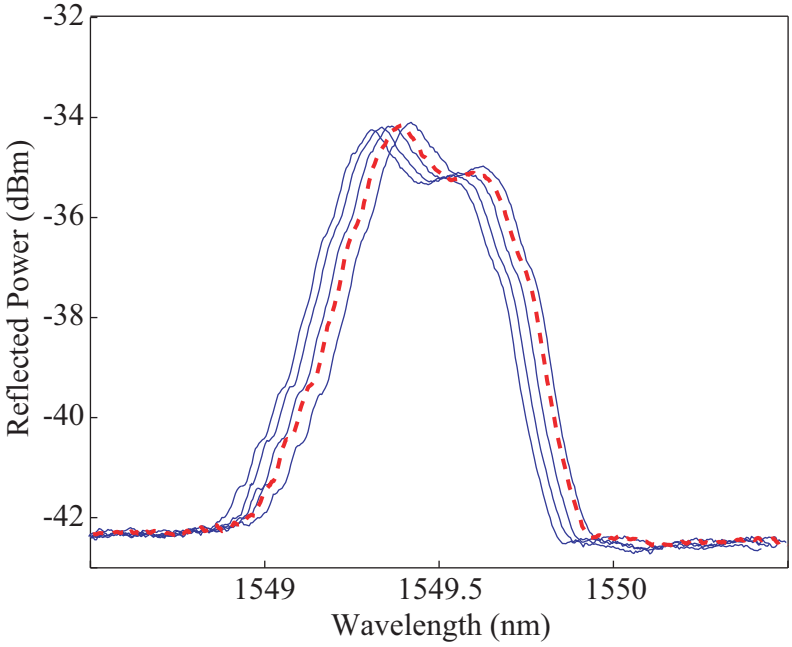

Figure 8.7: Graph showing the reflection spectra from the grating as the end of the fiber is displaced in the horizontal direction. Not all of the spectra from the calibration test are shown so that it is easier to see the shift in the Bragg wavelength. The red dashed spectrum is the reflection spectrum from the $x = 0$ mm prebent resting position.

Figure 8.7 shows the reflection spectra from the grating when the end of the fiber is displaced in the horizontal direction ± 5 mm from the prebent resting position. Again the red dashed spectrum on the graph is the reflection spectrum from the resting position. Not all of the spectra from the calibration test are shown so that it is easier to see the small shift in the Bragg wavelength. The figure shows that as the end of the fiber is displaced the reflection power stays fairly constant

and the peak wavelength shifts slightly to lower or higher wavelengths. Because the fiber only experiences uniform tensile strain when displaced in the horizontal direction only wavelength shifts should be expected. Figure 8.8 shows the shifts in Bragg wavelength and peak reflected power for horizontal bending of the tube. The reflected power changes slightly most likely due to the fiber not being aligned perfectly with the defined vertical and horizontal directions. The dots and diamonds on the graph are the collected data and the solid and dashed lines are linear fits to the data.

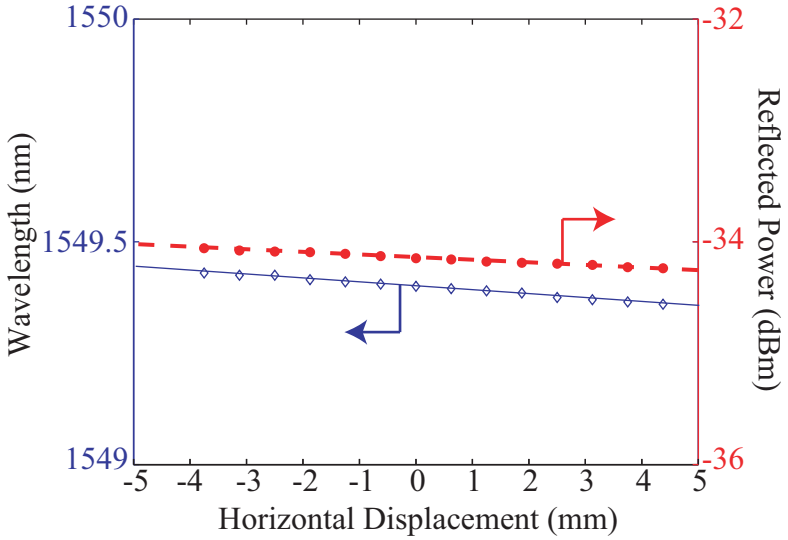

Figure 8.8: Bragg wavelength shift and change in reflected power for horizontal displacement of the tube end. The inset shows some of the recorded reflection spectra.

The sensitivity matrix for the system is defined as,

$$\begin{bmatrix} \Delta\lambda \\ \Delta R \end{bmatrix} = \begin{bmatrix} A & B \\ C & D \end{bmatrix} \begin{bmatrix} \Delta x \\ \Delta y \end{bmatrix}, \tag{8.6}$$

where $\Delta\lambda$ is the change in Bragg wavelength, ΔR is the change in reflected power, Δx is the tube end displacement in the horizontal direction, and Δy is the tube end displacement in the vertical direction. The A and B coefficients are the slopes of the linear fits to the wavelength change as a function of horizontal and vertical displacement respectively. The C and D coefficients are the slopes of the linear fits

to the reflected power change as a function of horizontal and vertical displacement respectively. These coefficients are experimentally determined to be A=-0.008862 nm/mm, B=-0.08557 nm/mm, C=-0.02236 dB/mm and D=-0.35 dB/mm.

8.2.2 Comparison to a Standard FBG

To show the difference between the SR-FBG and a standard FBG to changes in bend the same calibration experiment is performed on a commercially written FBG in SMF-28 circular cladding fiber. The commercial grating is inserted into a tube of the same length as before and fixed at both ends with glue. Again the setup of Figure 8.4 is used and the tube and fiber are prebent to the same location as the D-fiber calibration experiment.

Figure 8.9 shows the shifts in the Bragg peak wavelength and the changes in reflection power as the tube is deflected in the vertical direction. The inset of the figure shows the reflection spectra. The red dashed spectrum is the reflection spectrum at the pre-bent zero deflection point. Because the grating is written in the core at the geometrical center of the SMF-28 fiber, nonuniform strain is not experienced and the grating does not chirp. The only strain experienced as the end of the fiber is displaced is uniform tensile strain because the fiber is fixed at two ends. The peak wavelength shifts but does not change reflection power. The linear fit to the wavelength shift has a slope of -0.2 nm/mm. The change in peak power is negligible as the end of the tube is deflected.

Figure 8.10 shows the shifts in the Bragg peak wavelength and the changes in reflection power as the tube is deflected in the horizontal direction. Again the inset of the figure shows the reflection spectra, and again the red dashed spectrum is the reflection spectrum at the prebent zero deflection point. The graph is almost identical to the graph for the vertical deflection test because of the symmetrical shape of the SMF-28 fiber. The linear fit to the wavelength shift has a slope of -0.21 nm/mm and the change in peak power is negligible.

Because the two bending directions result in almost identical responses when using the symmetrical SMF-28 fiber the sensitivity matrix becomes singular.

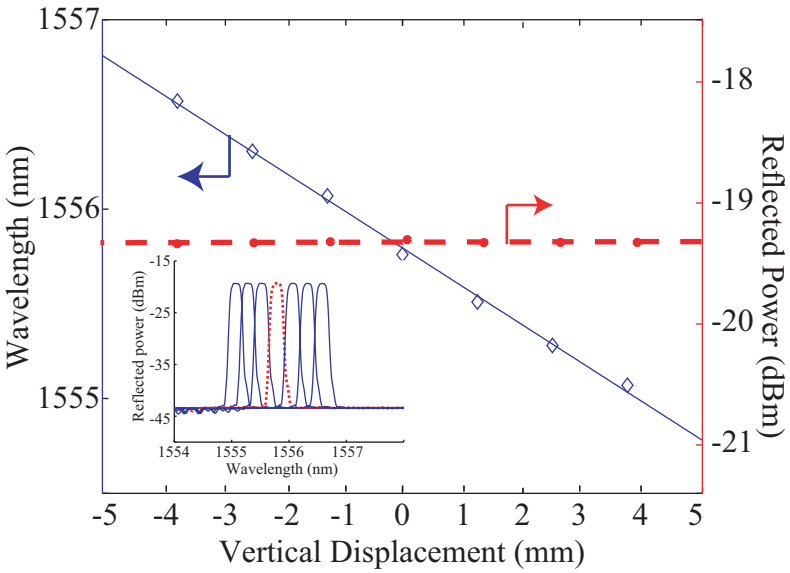

Figure 8.9: Bragg wavelength shift and change in reflected power for vertical displacement of the tube end of a commercial FBG. The inset shows the reflection spectra.

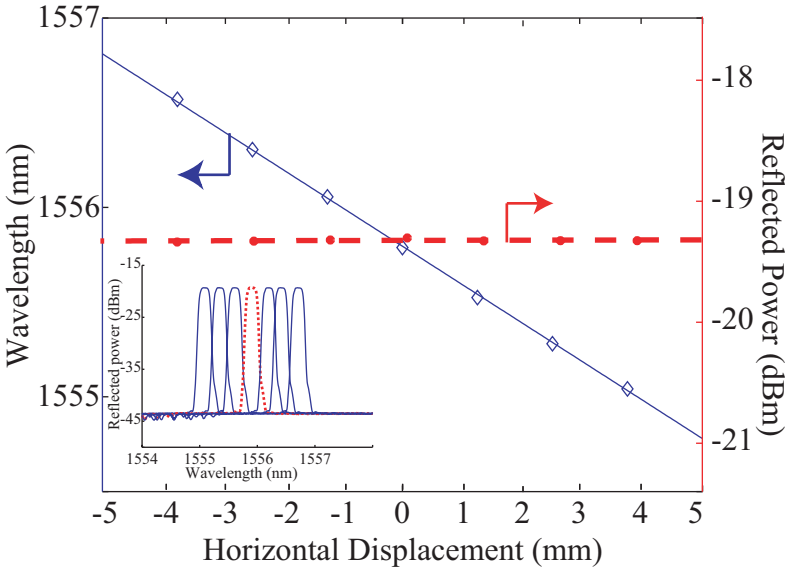

Figure 8.10: Bragg wavelength shift and change in reflected power for horizontal displacement of the tube end of a commercial FBG. The inset shows the reflection spectra.

A singular matrix means that the inverse does not exist and the commercially written FBG could not be used as a multi-dimensional bend sensor without further modification [78].

8.3 Multi-Dimensional Experiment Results

By monitoring changes in the Bragg wavelength and peak reflectivity along with the inverse of the sensitivity matrix, the tube end displacement is predicted in two dimensions. The inverse of the sensitivity matrix is given as,

$$\begin{bmatrix} \Delta x \\ \Delta y \end{bmatrix} = \begin{bmatrix} A & B \\ C & D \end{bmatrix}^{-1} \begin{bmatrix} \Delta\lambda \\ \Delta R \end{bmatrix}. \tag{8.7}$$

Again the setup of Figure 8.4 is used along with the sensing interrogator. Table 8.1 shows the results by comparing the actual tube end displacement with the predicted tube end displacement as calculated using Eq. 8.7 and the observed Bragg wavelength shift and reflected power.

Overall the predicted displacement is in good agreement with the actual displacement values showing that two dimensional bend sensing can be realized with a D-fiber and a SR-FBG.

Table 8.1: Comparison of actual displacements vs. measured displacements.

Actual Displacement- horiz. (mm), vert. (mm)	**Predicted Displacement horiz. (mm), vert. (mm)**	**Percent Difference (%)**
+5.0, 0.0	+5.33, -0.026	+6.4, n/a
+5.0, +2.5	+5.48, +2.47	+9.2, -1.2
+5.0, -2.5	+4.89, -2.49	-2.2, -0.4
0.0, -5.0	+0.80, -5.05	n/a, +1.2
0.0, -5.0	+0.80, -5.05	n/a, +0.9
-2.5, +2.5	-3.0, +2.53	-18.2, +1.2
-2.5, 0.0	-2.29, +0.003	-8.7, n/a
-2.5, -2.5	-2.16, -2.52	-14.5, +0.8

8.4 Error Assessment

By examining the displacement that created the largest percent difference between the actual and predicted value the major error component can be determined. The displacement with the largest percent difference is (-2.5, +2.5). Using the sensitivity matrix theoretical values are found for the change in Bragg wavelength and the change in the reflected power. The change in wavelength and change in reflected power are calculated to be,

$$\begin{bmatrix} \Delta\lambda \\ \Delta R \end{bmatrix} = \begin{bmatrix} -.008862\frac{nm}{mm} & -0.08557\frac{nm}{mm} \\ -0.02236\frac{dB}{mm} & -0.3499\frac{dB}{mm} \end{bmatrix} \begin{bmatrix} -2.5mm \\ 2.5mm \end{bmatrix} = \begin{bmatrix} -0.1917nm \\ -0.8188dB \end{bmatrix}. \quad (8.8)$$

The measured values for the change in wavelength and the change in reflected power are found to be,

$$\begin{bmatrix} \Delta\lambda \\ \Delta R \end{bmatrix} = \begin{bmatrix} -0.190nm \\ -0.819dB \end{bmatrix}. \quad (8.9)$$

The difference in the calculated and measured value of $\Delta\lambda$ is less than 1% and shows that the major source of error comes from the limited resolution of the interrogator. For these experiments the interrogator is used such that the full wavelength spectrum is saved. In this mode the interrogator only saves wavelengths every 5 pm meaning that large displacement errors are introduced whenever the theoretical wavelength value falls in the middle of what the interrogator saves. The error could be overcome by orienting the fiber differently so that the sensitivity to horizontal displacement increased such that it would be greater -0.010 nm/mm. The error would also decrease over larger deflections in the horizontal direction.

Other factors that lead to errors in the predicted displacement values are errors in the original line fits used to create the sensitivity matrix and experimental misalignments.

8.5 Summary

This chapter presents a simple method to use the SR-FBG as a multi-dimensional bend sensor. The grating is inherently sensitive to bend due to the

asymmetric shape of the D-fiber. The core and the grating are both located above the geometrical center of the cladding meaning that nonuniform strain is induced when the fiber is bent in the vertical direction. The nonuniform strain causes the grating to chirp and reduces the grating reflectivity.

To detect bend in the horizontal direction the fiber is fixed at both ends inside of a hollow tube thus creating uniform tensile strain when bending. The uniform tensile strain causes the grating period to change and the Bragg wavelength will shift. Therefore, both vertical and horizontal bend can be detected by monitoring the Bragg wavelength shift and the peak reflected power.

Chapter 9

Vernier Sensors: Super Structured and Fabry-Pérot SR-FBGs

For the majority of this work, only uniform Bragg gratings have been considered in the fabrication and application of sensing devices. As discussed in Chapter 2 and Appendix B, non-uniform gratings can be fabricated and often find use in many applications. For example, chirped gratings are often employed as dispersion compensation elements in telecommunication applications. Apodized gratings are also used in filter applications where the side lobe suppression ratio is critical.

Two additional types of non-uniform Bragg gratings are the super-structured and Fabry-Pérot fiber Bragg gratings (SS-FBGs and FP-FBGs). These configurations use regions of gratings and regions of gaps (areas where no gratings exists) to alter the reflection and transmission properties along the length of the fiber. The super-structured (sometimes referred to as sampled) fiber Bragg grating generates multiple reflection peaks, or reflection channels dependent upon the Fourier components of the sampled grating. On the other hand, the FP-FBG creates multiple transmission peaks inside of the transmission stop band that is produced from a uniform FBG.

In this chapter both the SS- and the FP-FBG are investigated for sensing applications. Due to the multiple channels that are produced in either reflection or transmission, a Vernier type device is proposed that increases the sensors resolution and sensitivity in many important applications. The theory behind both configurations is discussed and simulations are performed to show the feasibility of such devices. Due to the holographic fabrication steps of the SR-FBG, only minor changes in the fabrication process are required to create the structured gratings.

9.1 The Vernier Scale

The innovation of the sensor is achieved by using a concept based on a Vernier scale, which is very common in manual micrometers. A Vernier scale has two sets of lines in which one set has one more line than the other and slightly different spacing. Figure 9.1(a) shows that for any relative positioning of the two scales only one set of lines are aligned with each other. Figure 9.1(b) illustrates that if the bottom scale is shifted by a small amount then a different set of lines is aligned. In this case, a small shift of Δ causes the second to last set of lines to be aligned.

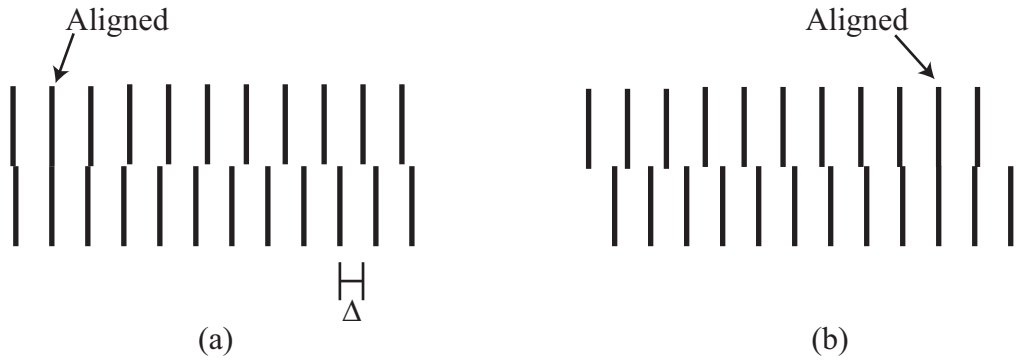

Figure 9.1: A Vernier scale that consists of two sets of lines in which the bottom set has one more line than the top set. With no shift (a) shows that the second two lines are aligned and (b) shows that with a shift of Δ the second to last set are aligned.

The Vernier scale can be applied to the innovative sensor design by treating each line as a reflection or transmission peak. The top set of lines corresponds to the reflection or transmission peaks of a fixed structured grating while the bottom set of lines corresponds to the reflection or transmission peaks of the sensing structured grating. As an environmental variable causes a small shift in the sensing peaks, only the peak that aligns with the fixed peak is transmitted. In this way very small changes in an environmental variable causes large changes in the output from the gratings and thus improved resolution and sensitivity.

9.2 Analysis of Structured Gratings

Structuring gratings is not a new a idea and some of the initial work with structured gratings in optical fiber can be found in [79]. Other work with structured gratings can also be found in the semiconductor laser community with buried gratings inside of the resonator cavity [80]. Structured fiber Bragg gratings are used for multi-channel multiplexing and demultiplexing, mutli-channel dispersion compensation, metrology, repetition rate multiplication, and as comb filters [68, 81].

Using these types of gratings for sensor work has not been significantly discussed in the literature. The following sections provide the necessary analysis and theory to show the novelty of a sensor created using structured gratings.

9.2.1 Super-Structured Fiber Bragg Gratings

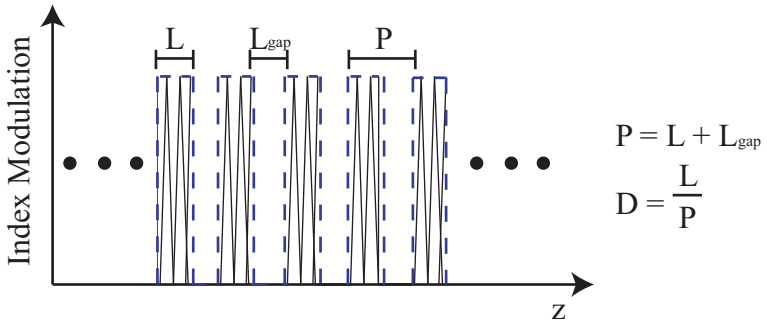

Figure 9.2: Diagram of a super structured grating. The dashed lines represent the long period super structure.

The underlying principle behind the SS-FBG is that the grating itself is modulated, either in amplitude or phase, with a long periodic structure. Figure 9.2 shows a schematic of an amplitude modulated SS-FBG where regions of sub-gratings and regions of no gratings exist. The period of the super-structure, P, is defined as the sum of the length of one sub-grating, L, and the length of one non-grating region, L_{gap}. The duty cycle, D, is defined as the ratio of the length of the sub-grating to the period of the super-structure. By varying the duty cycle of the structured grating

various reflection and transmission spectra can be achieved and tailored to a specific application.

The transfer matrix formalism of coupled mode theory creates an extremely convenient method to simulate many different SS-FBGs numerically and gain intuition into the resulting reflection spectra. For example, Figure 9.3(a)-(d) shows the reflection spectra for SS-FBGs with 100 μm subgratings and varying duty cycles. The total grating length is fixed at 1.5 cm independent of the duty cycle. From these simulations it is found that the resonant spacing and the maximum reflectivity is dependent on the duty cycle.

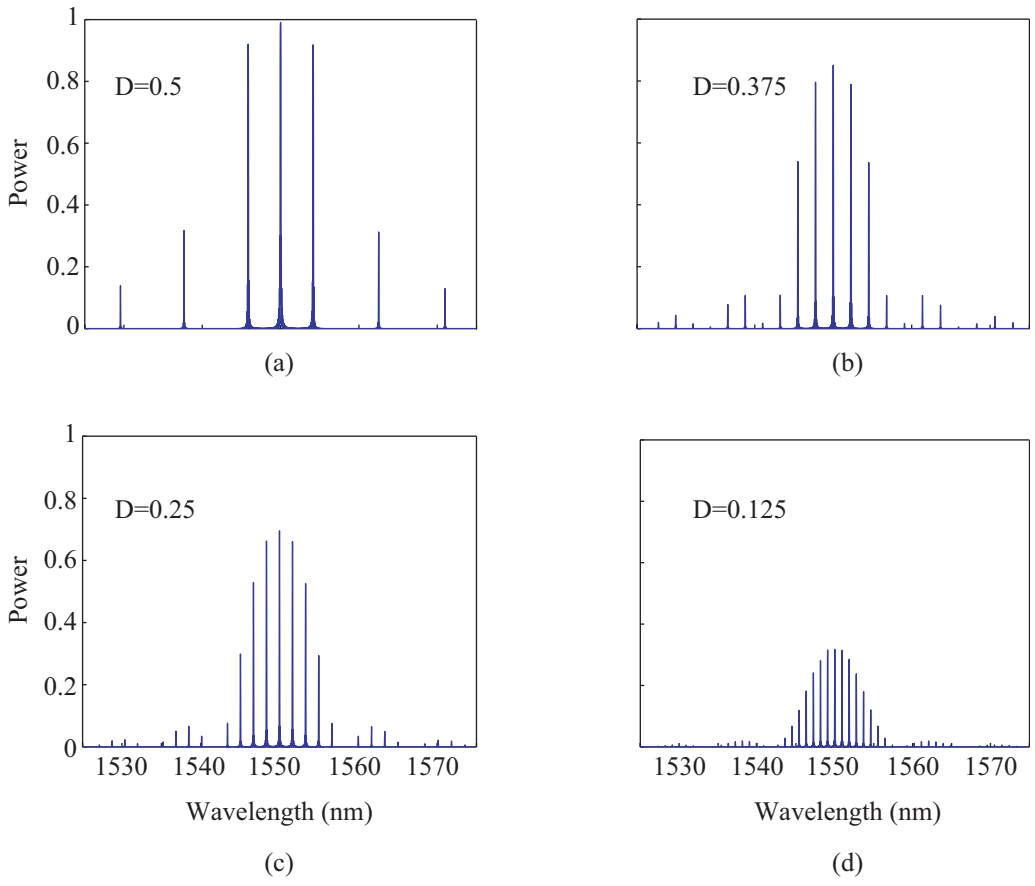

Figure 9.3: Simulated reflection spectra for SS-FBGs with (a) a 50% duty cycle, (b) a 37.5% duty cycle, (c) a 25% duty cycle, and (d) a 12.5% duty cycle.

Figure 9.4 shows that upon further inspection the reflection spectrum from the the structured grating corresponds to the envelope of the reflection spectrum from a single 100 μm long subgrating. Likewise, the maximum reflectivity from the structured grating corresponds to the reflectivity of all the grating pieces concatenated together without any gaps. The FWHM of each resonant peak is also on the same order as the FWHM from a uniform FBG.

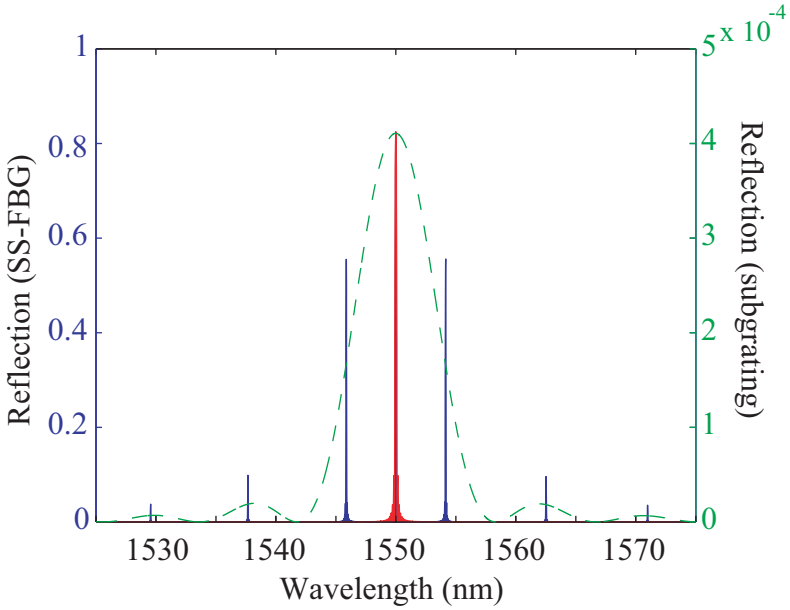

Figure 9.4: Graph showing that the SS-FBG reflection spectrum corresponds to an envelope from a single subgrating (dash line) and that the maximum reflectivity corresponds to the reflectivity of all the subgratings concatenated together.

While the transfer matrix method gives a good general intuition as to the wavelength location of each resonant peak an analytical expression for the peak separation can be determined using Fourier methods due to the periodic nature of the sampling function. The Fourier analysis of the grating super structure can be found in Appendix C. The resulting resonant peak separation is analytically found to be [82]

$$\Delta\lambda = \frac{{\lambda_B}^2}{2n_{eff}P}. \tag{9.1}$$

The main intuition to gain from the transfer matrix method and the Fourier analysis for SS-FBGs is:

1. SS-FBGs produce resonant peaks in the reflection spectrum.
2. Smaller duty cycles correspond to closer spaced resonant peaks.
3. The resonant peak wavelengths correspond to the envelope of the reflection spectrum from a single subgrating used to create the super structured grating.
4. The resonant peak wavelength spacing is inversely proportional to the super structure period.
5. The maximum reflectivity from the SS-FBG corresponds to the reflectivity of all the grating pieces concatenated together without any gaps.
6. The FWHM of each resonant peak is close to the FWHM of a single uniform FBG.

9.2.2 Fabry-Pérot Fiber Bragg Gratings

Unlike SS-FBGs which create resonant peaks in the reflection spectrum, FP-FBGs can be used to create extremely narrow transmission windows inside of the normal uniform grating stop band. Similar to a Fabry-Pérot cavity, the separation between these transmission peaks depends on the gap width and the width of the stop band depends on the reflectivity of the individual gratings.

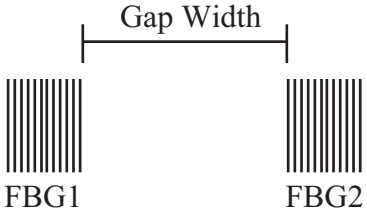

Figure 9.5: Schematic showing a FP-FBG.

Figure 9.5 shows a diagram of FP-FBG. The FP-FBG consists of FBG, followed by a section of fiber with no grating, followed by another FBG. The two FBGs act as wavelength specific mirrors to create the cavity. Figure 9.6(a) shows a simulated transmission spectrum from a FP-FBG. Figure 9.6(b) shows the same spectrum zoomed in around two of the transmission peaks within the grating stop band.

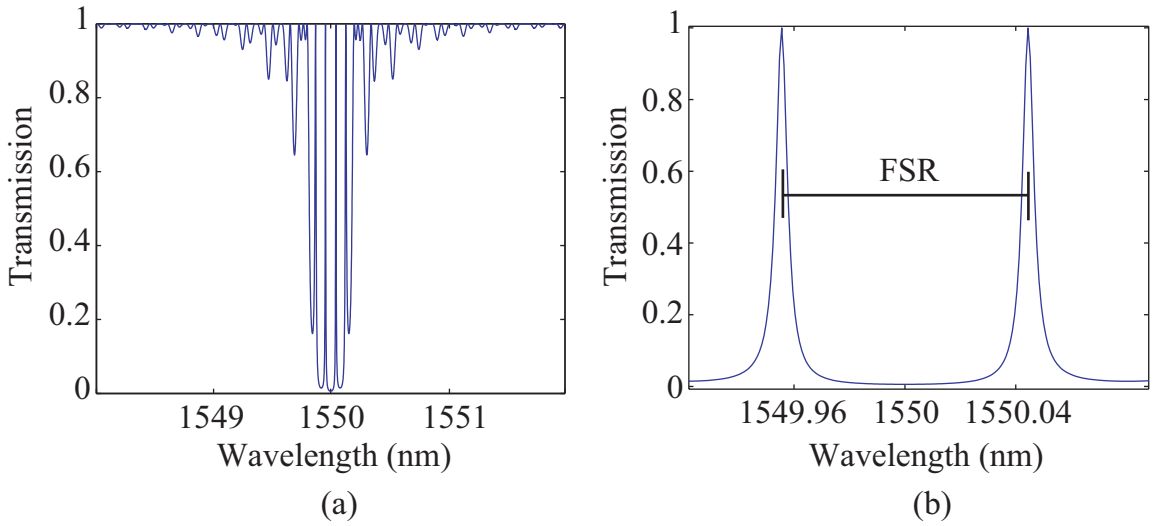

Figure 9.6: (a) Simulated transmission spectrum of FP-FBG. (b) Same spectrum zoomed in around two of the transmission peaks.

For a traditional Fabry-Pérot cavity the free spectral range (FSR), or the distance between transmission peaks, is given as

$$FSR = \frac{\lambda^2}{2n_{eff}L}. \tag{9.2}$$

However, traditional Fabry-Pérot cavities use two discrete mirrors to form the cavity creating a distance, L, that is well defined. In a FP-FBG, the end mirrors are formed using FBGs which act as distributed reflectors along the length of the fiber. Because the mirror is distributed, the exact cavity length is not as easily obtained. An effective cavity length of the FP-FBG needs to be used in order to more effectively calculate the mode spacing. Barmenkov [83] analytically shows that the effective grating length

can be calculated as

$$L_{eff} = L_{grating}\frac{\sqrt{R}}{2\text{atanh}(\sqrt{R})}, \tag{9.3}$$

where R is the the reflectance from one of the FBGs. Assuming the two FBGs are identical then the effective cavity length is $L = L_{gap} + 2L_{eff}$. In most instances it is sufficient to consider the effective cavity length as the center to center distance of the two FBGs [84]. As with other optical cavities, the finesse of the FP-FBG transmission peaks is dependent on the reflectivity of the two cavity mirrors, or in this case the two FBGs. Assuming the two gratings have the same reflectance, then the finesse of the FP-FBG is given as

$$F = \frac{\pi\sqrt{R}}{1-R}, \tag{9.4}$$

where R is the maximum reflectance of the grating. The FWHM of the transmission peaks inside of the grating stop band is defined as

$$\Delta\lambda_{FWHM} = \frac{FSR}{F}. \tag{9.5}$$

Substituting Eq. 9.2 and Eq. 9.4 into Eq. 9.5 gives the FWHM of the transmission peaks as

$$\Delta\lambda_{FWHM} = \frac{\lambda_B^2}{2\pi n_{eff} L}\frac{1-R}{\sqrt{R}}. \tag{9.6}$$

Figure 9.7 shows the transmission spectra of a FP-FBG with varying finesse. The finesse is varied by varying the grating strength, i.e. the change in the effective index of the guided mode. As expected the higher finesse cavities create sharper, narrower peaks in the spectrum. Unlike a traditional Fabry-Pérot cavity the higher finesse also increases the FSR. The increase in FSR is expected for a cavity with FBG mirrors and can be understood by examining Eq. 9.3 and Eq. 9.2. As the FBG mirrors increase in reflectivity their effective length decreases thus decreasing the overall cavity length and increasing the FSR.

From this analysis the important intuition to gain about FP-FBGs is:

1. FP-FBGs produce transmission peaks inside the stop band of a FBG.

2. The FSR of the peaks inside the stop band is dependent on the effective cavity length and thus on the reflectivity of the gratings.

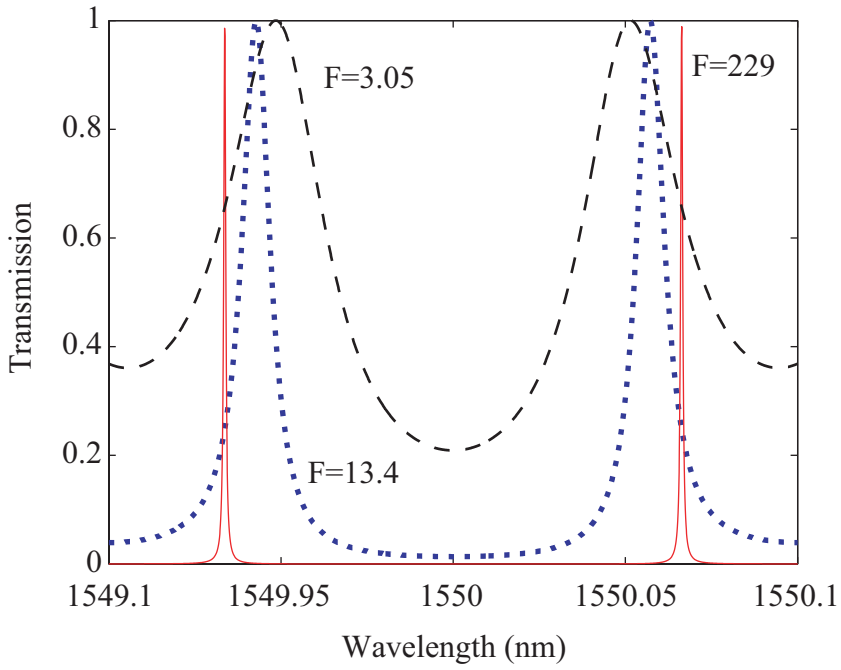

Figure 9.7: Simulated transmission spectra of a FP-FBG with varying finesse.

3. The finesse of the cavity is dependent on the reflectivity of the gratings.

4. The bandwidth of the stop band where the transmission peaks reside is the bandwidth of one of the FBG mirrors (assuming both are identical).

5. The maximum reflectivity of the FP-FBG corresponds to the maximum reflectivity of the two FPGs concatenated together without a gap.

9.3 Proposed Vernier Sensing Layouts

The previous sections analyzed the reflection and transmission properties of structured fiber Bragg gratings. This section proposes possible sensor configurations that utilize the unique reflection and transmission spectra of the structured gratings. The sensors combine the benefits of the structured gratings with the Vernier effect. The Vernier effect is essentially the transmission through two periodic spectra with slightly different channel spacing or free spectral ranges. One of the structured gratings is fixed while the other grating is the sensing head which sweeps due to the intended environmental variable. The relationship between the wavelength shift and

the intensity variation depends on the difference between the FSR of the two structured FBGs. Thus, the sensitivity of the sensor system can be varied by controlling the FSR of the variable grating. The periodic nature of both SS- and FP-FBGs make these type of gratings ideal for such a sensing layout.

Unlike most of the other sensors presented in this work where the measurand is sensed by tracking changes in the Bragg wavelength, the proposed Vernier sensors would detect the environmental variable by observing a difference in the transmitted power. Monitoring of intensity variations is typically significantly faster and more accurate, resulting in a dramatic improvement in FBG sensing systems.

9.3.1 A SS-FBG Vernier sensor

Because the resonant peaks from a SS-FBG present themselves in the reflection spectrum, a simple serial connection of the sensing and fixed gratings will not result in a Vernier effect. In order to create a Vernier sensor using SS-FBGs a slightly more complex configuration needs to be used.

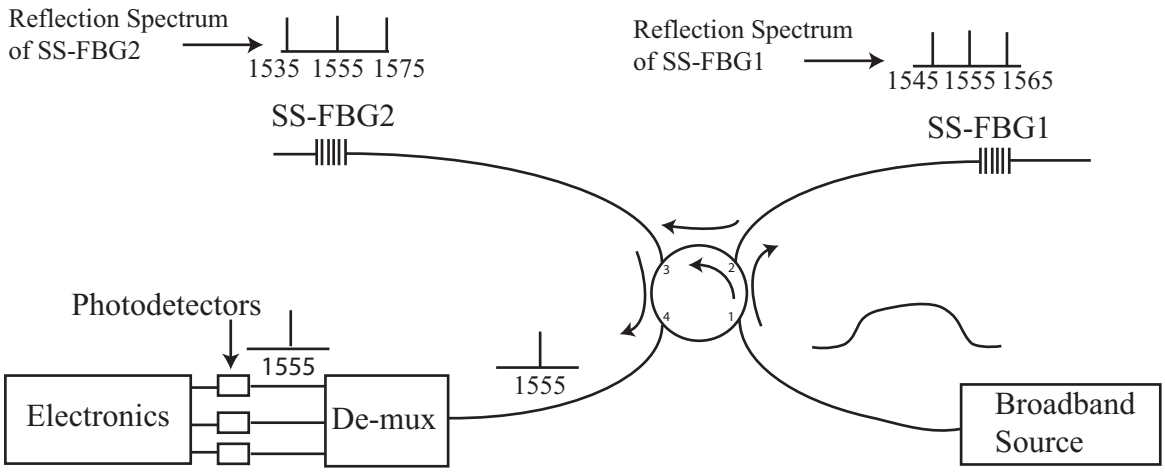

Figure 9.8: Schematic showing a possible interrogation configuration of a SS-FBG Vernier sensor.

Figure 9.8 shows a diagram of a possible sensing configuration that would produce the desired Vernier effect with SS-FBGs. The configuration consists of a

broadband light source that is coupled through an optical circulator to one of the SS-FBGs. The reflection spectrum from this grating becomes the transmitted light to the next grating as it passes through the next port on the circulator. The Vernier effect will be manifest if any of the peaks from the first grating align with any of the peaks from the second grating's reflection spectrum. The peaks that are co-located are reflected from the second grating and pass to the final port of the circulator to a demultiplexer and an array of photodetectors. A differential signal is then calculated and correlated back to the sensing variable.

In order to evaluate the feasibility of such a sensing scheme, the SS-FBG Vernier sensor is compared theoretically to the VOC sensor of Ch. 7. For simulation the first SS-FBG consists of an ∼1.5 cm long grating that is structured with 100 μm long subgratings and 800 μm long gaps. The channel spacing for such a grating is ∼0.9 nm and the maximum reflectivity is ∼0.38. The second SS-FBG is the same as the first grating except that the gaps are 700 μm long corresponding to a channel spacing of ∼1.05 nm and a maximum reflectivity of ∼0.4. Both gratings are simulated with a change in effective index equal to $2\text{x}10^{-4}$.

Figure 9.9 shows a progression of the simulation. The figures in the left column show the reflection spectra from both of the SS-FBGs. The figures on the right show the spectra that make it to the demultiplexer due to the Vernier effect assuming a 100 μW source. The figures in the right column also show the wavelengths over which integration is performed representing the de-mux and photodetectors of the proposed interrogation layout.

Figure 9.10 shows the differential signal between P1 and P2 as a function of VOC concentration in parts per million. The differential signal is defined as the power difference between two photodetectors normalized to the sum of their powers [85]. In order to achieve the highest possible sensitivity, the sensor should operate in the linear region of the differential signal. The solid line on Fig. 9.10 is a linear fit over that region.

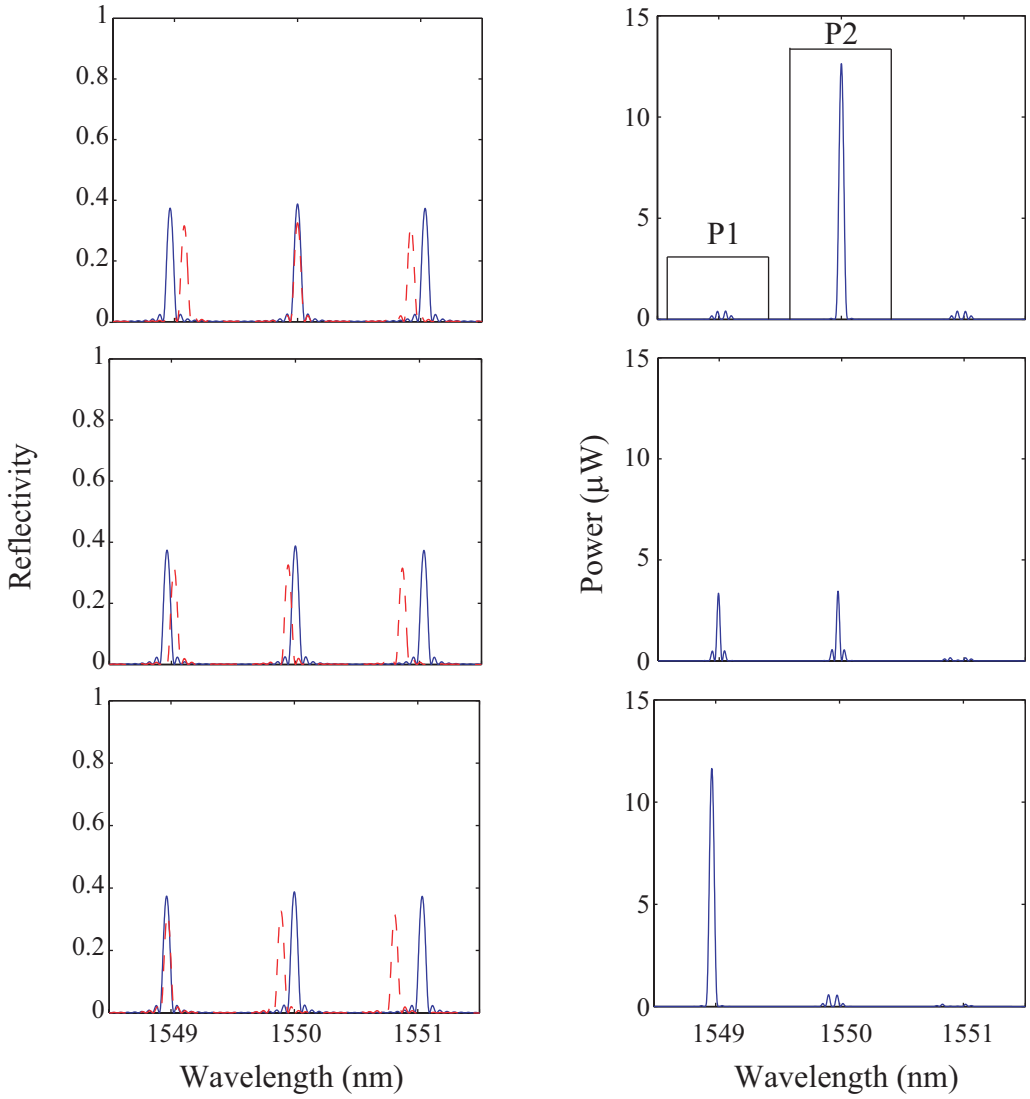

Figure 9.9: Graphs showing instances in the SS-FBG Vernier sensor simulation. The graphs on the right show both reflection spectra from the two gratings and the graphs on the right show the spectra that make it to the demultiplexer due to the Vernier effect.

A minimum detectable change in concentration can be defined as a figure of merit in order to compare the Vernier based sensor to the VOC sensor of Ch. 7. The minimum detectable change in concentration of dichloromethane using standard peak wavelength shift interrogation is found to be ∼4000 ppm from experiments in Ch. 7. Since the Vernier sensor is based on detectable power and not wavelength shift, the minimum detectable change in concentration (MDCC) can be defined as

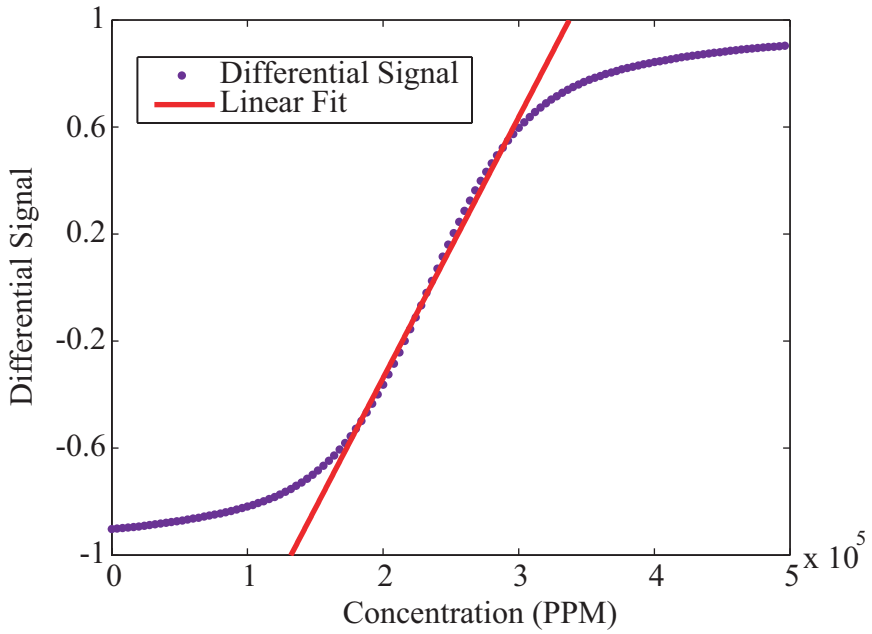

Figure 9.10: Graph showing the differential signal. The solid line is a linear fit to the linear region of the graph.

the change in VOC concentration that corresponds to a siganl-to-noise ratio of one [85]. The MDCC is defined as

$$MDCC = \frac{\delta p}{m}, \tag{9.7}$$

where m is the slope of the differential signal and δp is the differential signal noise. The differential signal noise can be expressed as [85]

$$\delta p = \frac{2\sqrt{(\delta P_1 \times P_2)^2 + (\delta P_2 \times P_1)^2}}{(P_1 + P_2)^2}, \tag{9.8}$$

where P_1 and P_2 are the powers of the two detected signals and δP_1 and δP_2 are the respective noises. Using data collected from [85], δP_1 and δP_2 are measured to be 0.12 nW and 0.14 nW for their equipment.

Using the modeled data along with the measured noise data the differential signal noise, δP is calculated to be 4.7x10^{-4}. The slope of the differential signal is found from the linear fit of Fig. 9.10 to be 9.75x10^{-6} ppm^{-1}. Using Eq. 9.7 the expected MDCC is calculated to be ~40 ppm or nearly two orders of magnitude smaller when compared to the non-Vernier based VOC sensor. The MDCC could be decreased even further if more power is available from the source.

It is noted that this dramatic increase in sensitivity is only valid over a small range in chemical concentration where the differential signal is linear. It could be possible to extend this range by more closely designing the gratings such that a cascade effect in the differential signal is experienced.

Most of the foreseeable problems that could occur when trying to implement the SS-FBG sensing scheme result from the relatively large width of the individual resonant peaks. Because the FWHM of the resonant peaks is on the same order as a uniform FBG (∼0.2 nm) some of the resolution is compromised. Also because of the sidelobes that exist on each resonant peak possible variations in power could occur creating undesirable fluctuation in the detected power.

9.3.2 A FP-FBG Vernier Sensor

In order to overcome some of the problems that are found when using SS-FBGs, this section presents a Vernier sensing scheme based on the FP-FBG. Because the FP-FBG creates transmission peaks inside of the grating stop band a simple series connection of the fixed and sensing grating can be made. Also due to the much higher reflectivity of the two individual gratings when compared to a subgrating from a SS-FBG, the individual transmission peaks are much narrower. The narrower peaks should lead to an even smaller minimum detectable change in concentration.

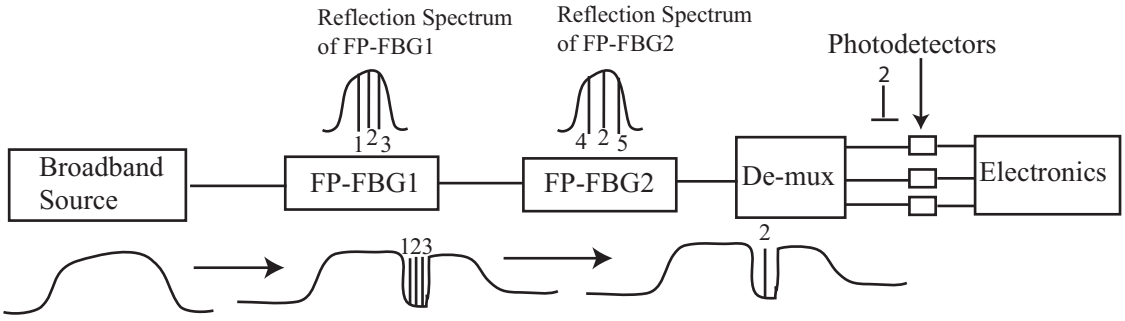

Figure 9.11: Diagram showing a possible interrogation setup for a FP-FBG Vernier sensor.

The interrogation of the FP-FBG Vernier sensor is similar to the interrogation scheme of the previous section. Figure 9.11 shows a diagram of the proposed sensor system. Again a broadband light source is used to illuminate both the fixed and the sensing gratings. Because the FP-FBGs produce transmission peaks a serial configuration is sufficient, eliminating the need for an optical circulator. To protect the light source from the Bragg grating reflections, an isolator is placed between the light source and the first FP-FBG. As with the previous sensor configuration, a demultiplexer, a series of photodiodes, and the necessary electronics are also employed to detect and create a differential signal.

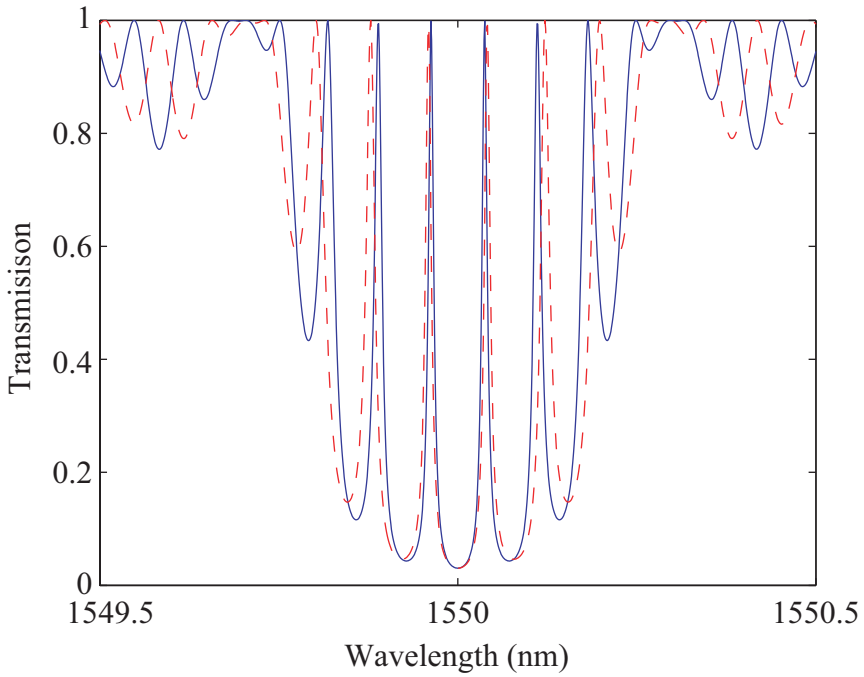

Figure 9.12: Simulated transmission spectra for both the FP-FBGs.

The transmission peaks from a FP-FBG reside within the stop band of the uniform gratings that are used as cavity mirrors. The total available bandwidth is only around 0.2 to 0.5 nm when uniform gratings are used and is therefore much less than the bandwidth from a SS-FBG. Using chirped FBG, or short strong gratings as the cavity mirrors increases the usable bandwidth dramatically [86]. While it is

more difficult to to create a chirped SR-FBG for such an application, the SR-FBG does lend itself to being very efficient for short grating lengths due to the high index contrast. Figure 9.13 shows the transmission spectrum from a 500 μm long uniform SR-FBG created with photoresist. The ultra-short grating produces a reflected signal that is greater than 98% and has a 3 dB bandwidth of nearly 5 nm.

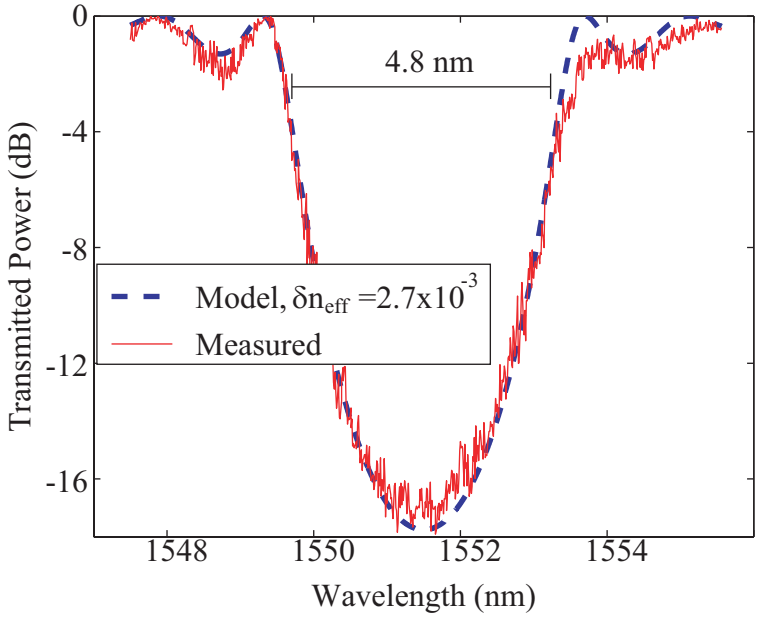

Figure 9.13: Measured and modeled transmission spectra for an ultra-short 500 μm long uniform SR-FBG.

As previously shown with the SS-FBGs, in order to evaluate the effectiveness of the FP-FBG Vernier sensor, computer simulations are performed and compared to the VOC sensor of Ch. 7. In the simulation two FP-FBG are used. The first FP-FBG consists of a cavity length of 8 mm and two uniform FBG cavity mirrors each 3 mm long. This cavity spacing corresponds to a FSR of ~75 pm. The second FP-FBG consists of a cavity length of 9 mm and two uniform FBG cavity mirrors each 3 mm long. The second cavity length corresponds to a FSR of ~69 pm.

Figure 9.12 shows the transmission spectra for the two FP-FBGs. Figure 9.14 shows a progression of the simulation. The figures in the left column show

the transmission spectra from both of the FP-FBGs zoomed in around two of the Fabry-Pérot peaks. The figures on the right show the spectra that make it to the demultiplexer due to the Vernier effect assuming a 100 μW source.

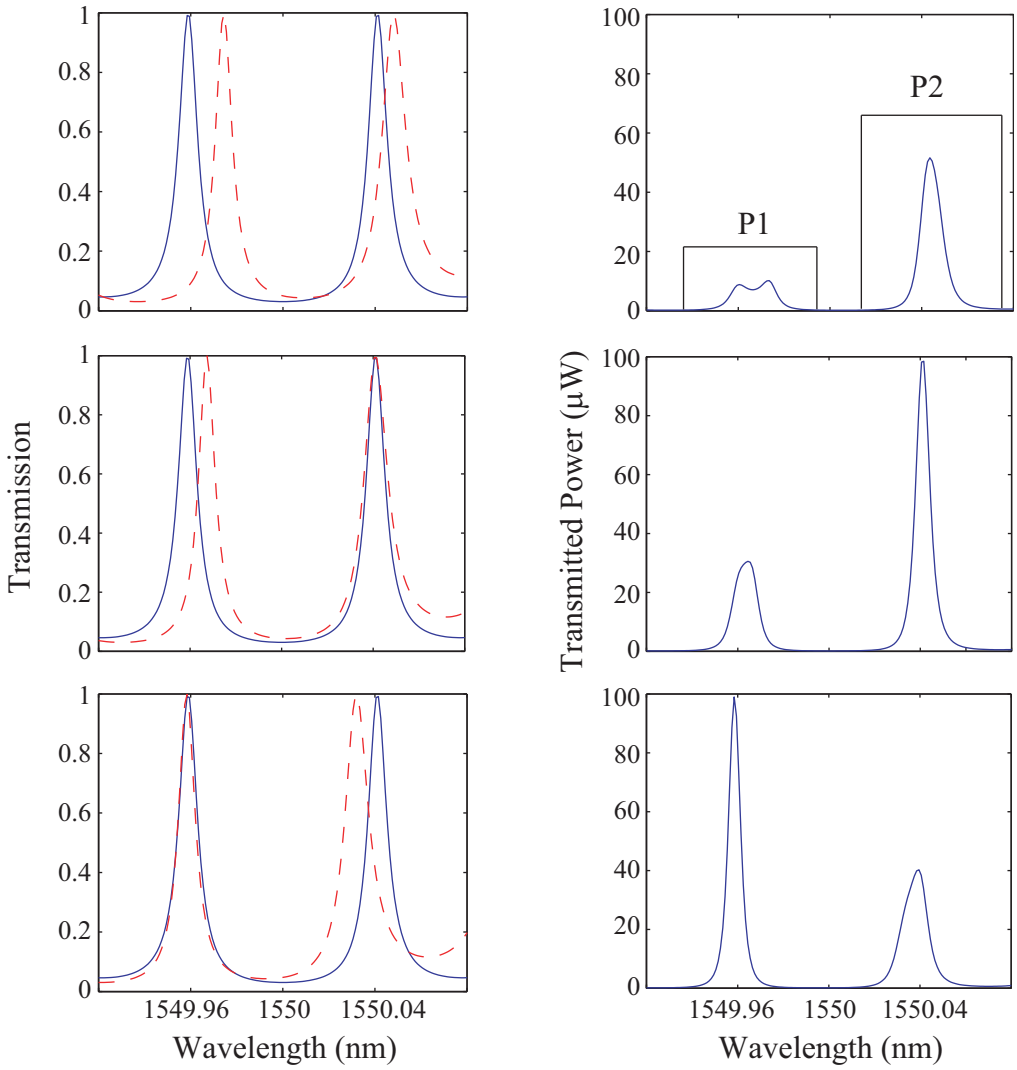

Figure 9.14: Graphs showing instances in the FP-FBG Vernier sensor simulation. The graphs on the right show both transmission spectra from the two gratings and the graphs on the right show the spectra that arrive at the demultiplexer due to the Vernier effect.

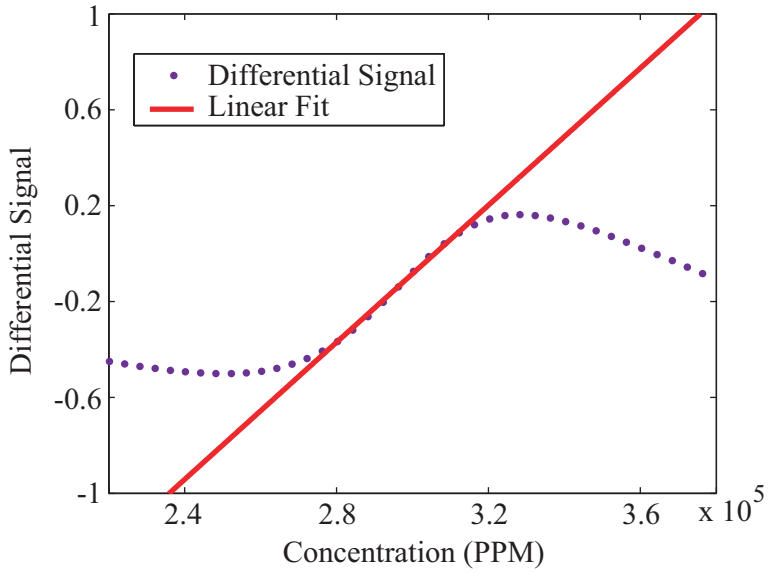

Figure 9.15: Graph showing the differential signal. The solid line is a linear fit to the linear region of the graph.

Figure 9.15 shows the differential signal between P1 and P2 as a function of VOC concentration in parts per million. Again, in order to achieve the highest possible sensitivity, the sensor should operate in the linear region of the differential signal. The solid line on Fig. 9.15 is a linear fit over that region.

Using Eq. 9.8 and Eq. 9.7 it is again possible to calculated a MDCC and compare it to the MDCC of the VOC of Ch. 7. The differential signal noise is calculated to be 1.64x10^{-4} with an input power of 100 μW. The slope of the linear fit in Fig. 9.15 is found to be 1.43x10^{-5} ppm^{-1}. Using Eq. 9.7 the MDCC is calculated to be $\sim$10 ppm representing a 4x improvement over the SS-FBG Vernier sensor of the previous section.

An obvious limitation to the FP-FBG Vernier sensor is the even smaller linear operating range of the differential signal. The available bandwidth versus resolution are design variables that must be considered when deciding on the FP-FBG or SS-FBG Vernier sensor configurations, however, both offer considerable resolution gains over a traditional peak tracking interrogation scheme.

9.4 Fabrication of Structured SR-FBGs

Because the grating pattern for SR-FBGs is produced holographically, a simple masking step may be applied to create structured gratings. Furthermore, because the long period features of a structured grating are rather large (>50 μm), the fabrication of a mask can be performed with simple laser printing. The use of laser printing for a mask eliminates the need to use expensive mask making equipment and procedures.

The mask is first created in Adobe Illustrator, or any other graphical program. The mask consists of stripes of black followed by clear regions. The photoresist used in the fabrication of the SR-FBG is a positive resist, meaning that areas that are exposed to UV light are washed away during the developing process. Once the mask has been designed it is printed using a high quality laser printer onto a transparent sheet. For this work the mask pattern is then transferred from the transparent sheet onto a photomask chrome plate for durability. Successful structured gratings can also be fabricated just from the transparent sheet.

To create the periodic structure a UV lamp is used to expose the photoresist on the flat surface of the D-fiber through the structured mask. This step replaces the pre-exposure step of Ch. 3 that is used when fabricating a uniform SR-FBG. Once the photoresist is exposed with the structured pattern the fabrication process remains the same as found in Ch. 3.

Two SS-FBGs are fabricated using the above mentioned process. The first SS-FBG is designed to have 100 μm long subgratings with a 50% duty cycle. The total grating length is 1.5 cm. The second SS-FBG is designed to have 150 μm long subgratings with 500 μm long gaps representing a duty cycle of $\sim$23%. Again the total grating length is 1.5 cm. Figure 9.16(a) shows an optical image from the first SS-FBG. Red light is coupled into the fiber to better show the regions where grating exists on the surface of the D-fiber. Figure 9.16(b) shows the measured reflection spectrum from this grating. The expected channel spacing from Eq. 9.1 is calculated to be 4.2 nm. The measured channel spacing from the reflection spectrum is found to be 4.13 nm.

Figure 9.17(a) shows an optical image from the second SS-FBG. Red light is again coupled into the fiber to better show the regions where grating exists on the surface of the D-fiber. Figure 9.17(b) shows the measured reflection spectrum from this grating. The expected channel spacing from Eq. 9.1 is calculated to be 1.26 nm. The measured channel spacing from the reflection spectrum is found to be 1.2 nm.

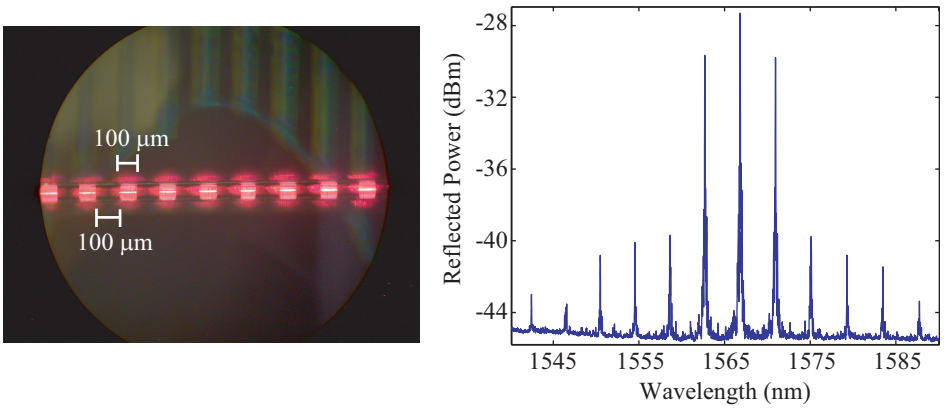

Figure 9.16: (a) Optical photograph of a SS-FBG on the flat surface of a D-Fiber. (b) The measured reflection spectrum from the SS-FBG.

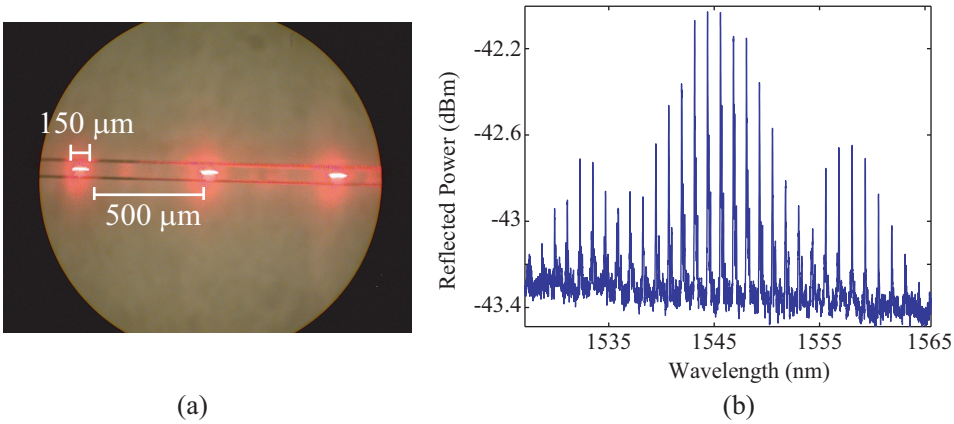

Figure 9.17: (a) Optical photograph of a SS-FBG on the flat surface of a D-Fiber. (b) The measured reflection spectrum from the SS-FBG.

FP-FBGs are also successfully fabricated using the masking technique. Figure 9.18 shows the measured and modeled transmission spectra for a FP-FBG created from two 1 mm long gratings with a 3.5 mm long gap. The measured spectrum is captured while launching vertically polarized light into the the fiber. It is expected that the measured Fabry-Pérot peaks extend to the top of the spectrum but are not visible due to the limited resolution of the OSA.

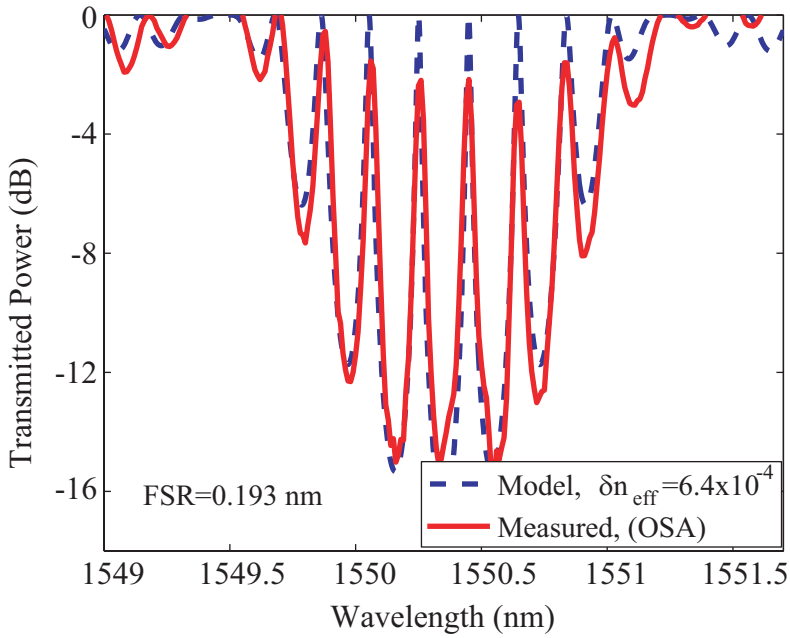

Figure 9.18: Measured and modeled transmission spectra from a FP-FBG.

9.5 Summary

Structured gratings create periodic peaks in the reflection or transmission spectra that can be used to create a Vernier effect. By utilizing the Vernier effect a dramatic increase in sensor resolution is achievable. The SR-FBG lends itself to being a structured grating by a simple change in the fabrication process.

A theoretical approach shows that a Vernier sensor decreases the minimum detectable concentration of VOCs by several orders of magnitude when compared to

a more traditional peak tracking interrogation. The MDCC could be lowered even further by using a more powerful broadband source thus increasing the signal to noise ratio. Another advantage of the Vernier sensor is the adjustable sensitivity that can be obtained by adjusting the FSR of the structured gratings.

Fabrication of the structured gratings is shown to be straightforward. Laser printing is used to create the necessary structured masks eliminating the need for costly mask making procedures. The channel spacing of the fabricated gratings match the theoretical model well.

Chapter 10

Conclusion

Optical sensing provides an attractive alternative to traditional electro-mechanical sensors in many environments. Perhaps the most common optical sensor is the fiber Bragg grating which reflects light at a specific wavelength while allowing all other wavelengths of light to be transmitted through the grating. Changes in the surrounding environment such as temperature, strain, and pressure cause the reflected wavelength to shift. Characterization of this wavelength shift allows the FBG to be used as an accurate environmental sensor.

While the traditional UV written FBG has provided the engineer with a valuable sensing option, there are certain inherent limitations that restrict its operation in some environments. To overcome these limitations this work has presented a new type of FBG that uses D-fiber and a surface etch to create a surface relief grating. Because the surface relief grating is a physical change in the topography of the D-fiber new sensors are realized that were not possible with a traditional UV written FBG.

10.1 Contributions

As explained in the introductory chapter, this research has built on the initial surface relief fiber Bragg grating work and has refined many of the processes while at the same time creating many new sensor options. Research from this work has resulted in the publication of seven peer reviewed journal articles, ten conference publications and/or talks, and one provisional patent. A summary of the major contributions of this work is as follows:

- Refining of the fabrication process for SR-FBG such that photoresist adhesion to the optical fiber is greatly increased.
- Discovering the importance of not fabricating the grating on the transition regions of etch to unetched fiber in order to maintain a symmetric reflection spectrum.
- Adding a pre-exposure step to the fabrication process in order to predefine the grating region.
- Adapting the transfer matrix method to SR-FBG simulation in order to quickly and accurately model complicated grating structures.
- Explaining the polarization dependence of SR-FBG through experimental and theoretical techniques.
- Fabricating SR-FBGs using rotated core D-fiber to minimize the polarization dependence.
- Creating a fully packaged high temperature sensor that has collected real data from industry field tests.
- Demonstrating the temporal thermal response of the SR-FBG at high temperatures.
- Integrating a chemical sensing material (PDMS) with the SR-FBG to create a volatile organic compound chemical sensor.
- Using the SR-FBG as a multi-dimensional bend sensor.
- Showing theoretically that structured SR-FBGs can use the Vernier effect to greatly increase a sensors sensitivity.
- Fabricating structured SR-FBGs using a simple mask technique created from a laser printer.

10.1.1 Increasing Photoresist Adhesion

Prior to this work, adhesion of the photoresist to the silicon dioxide cladding of the D-fiber created the most uncertainty in the fabrication process. Poor adhesion of the photoresist layer leads to uncertainty in the reflection properties of the grating due to a certain randomness in the overall grating structure. Uncontrollable features in the resulting reflection spectrum are undesirable because they bring into question the value of the Bragg wavelength and hence characterization of the sensing variable is nearly impossible.

To overcome the adhesion problem a well defined cleaning and fiber preparation protocol is now observed. It is found that three important steps need to be followed in order to dramatically increase the photoresist adhesion. First the fiber needs to undergo a short plasma etch in order to roughen the fiber surface. Second, the fiber must be cleaned thoroughly in a bath of sulfuric acid in order to remove any contaminants that are on the fiber surface. Lastly the fiber must go through a longer than normal dehydration bake in order to remove any moisture prior to photoresist application. Stringently following these steps has led to a significant increase in SR-FBG yield and reflection spectra that are suitable for sensing applications.

10.1.2 Improving the Non-symmetric SR-FBG Reflection Spectrum

During the initial stages of this work undesirable features on the long wavelength side of the Bragg wavelength were present in the reflection spectra of many SR-FBGs. Again these features were undesirable as it made characterization of the sensing variable difficult.

It was hypothesized that these features were the result of fabricating the grating on the transition regions of the D-fiber that went from being etched to unetched. It was hypothesized that if the gratings overlapped these regions than two things would occur. (1) The effective index of the guided mode would no longer be constant as it propagated the length of the grating. In effect part of the grating would be chirped resulting in a reflection spectrum that would be wider than the expected spectrum from a uniform grating. (2) Because only part of the grating had been

chirped and there is a change from uniform to non-uniform grating, a Fabry-Pérot cavity would form causing fringes to appear on the long wavelength side of the main Bragg peak.

The hypothesis was validated by modeling the situation using the transfer matrix method. To show experimental validation a uniform UV FBG was written in the D-fiber core. Initially the reflection spectrum was symmetric as would be expected from a uniform grating. The FBG was then etched in HF acid allowing part of the grating region to be on the transition from etched to unetched fiber. The resulting reflection spectrum showed the same fringes on the long wavelength side of the main Bragg peak that existed with many SR-FBGs confirming the hypothesis.

10.1.3 Pre-patterning the Grating Region

To overcome the undesirable fringes on the long wavelength side of the Bragg peak, the fabrication process had to be altered. A simple masking technique was developed that consisted of creating a mask using a glass slide, black tape, and a UV lamp. Because the photoresist used in this work is positive resist the black tape would define the grating region. The glass slide with the black tape is now placed on top of the fiber in the region of the desired SR-FBG and the mask and fiber are exposed using the UV lamp. This step now defines the grating region before being exposed to the two beam interference pattern and ensures that gratings will not be fabricated on the transition regions.

10.1.4 Using the Transfer Matrix Method to Model SR-FBGs

In the initial development of SR-FBGs the computer simulation was performed by direct numerical integration of the coupled-mode equations. During these early stages this numerical method was critical in the validation of the expected spectral response of the gratings, however, the method was very slow which led to limitations on the complexity of the grating structure.

To overcome this limitation, the transfer matrix method was adapted for SR-FBGs and implemented in MATLAB. The primary adaptation was in the calculation of the coupling coefficient by performing an overlap integral of the grating region with the guided mode of the D-fiber found using the software package BeamPROP. The transfer matrix method has provided an invaluable tool for the fast simulation and verification of many different grating structures.

10.1.5 Explaining the Polarization Dependence of SR-FBGs

Because the core of the D-fiber is elliptical, two polarization states exist for the guided fundamental mode. These two polarization states have slightly different propagation constants and thus should produce Bragg reflections at two different wavelengths. This work has shown that while this is certainly the case, the reflection strengths from the two polarization states are not equal. The polarization dependence is shown both theoretically and experimentally to be the result of the air-cladding interface and the asymmetric waveguide structure. The strongest reflection occurs for light that is polarized parallel to this interface for both horizontal and vertical core D-fiber.

10.1.6 Minimizing the Polarization Dependence Using Rotated Core fiber

By rotating the core orientation with respect to the flat surface of the D-fiber, the transverse electric field for the two polarization states can have components that are both parallel and perpendicular to the air-cladding interface thus reducing the polarization dependence. Reducing the polarization dependence is essential in creating sensors that use both polarization states such as detecting strain in both the transverse and longitudinal directions.

A SR-FBG was fabricated using D-fiber with a 40° rotated core. The reflection strength was measured for both the polarization states and was found to be much more equal when compared to the non-rotated core fiber. Theoretically it was shown that if the fiber core was rotated to an angle of 45° then the reflection strength from the two polarization states would be equal.

10.1.7 Packaging for Industry Ready High Temperature Tests

For any optical fiber sensor to be used in real world tests, a suitable package must be developed. For this work two packaging methods were developed and demonstrated for the SR-FBG high temperature sensor. One option created a rigid probe package while the second option created a more flexible type probe.

During the packaging process it is essential to preheat the stainless tubes before the insertion of the optical fibers. If the tubes are not preheated, then a material is deposited onto the fibers during temperature testing causing hysterisis that would not be present otherwise. By preheating the tubes the stainless steal is allowed to oxidize without deposition onto the optical fiber.

The two packaging schemes have proven to be very successful in creating sensors that are robust, easy to handle, and are reusable. The flexible probe package was successfully employed as an engine temperature probe on a small aircraft that flew from Florida to Wisconsin for an air show.

10.1.8 Demonstrating the grating Temporal Thermal Response

Using the fiber sensor integrated monitor (FSIM) along with a SR-FBG a rugged, high speed system was presented that showed both fast response time from the sensor and fast recording time from the interrogator. This system is able to be applied to more real time measurements as opposed to just quasi-static measurements. The main contribution was showing that the SR-FBG responds very quickly to thermal shocks at high temperatures.

10.1.9 Creating a Chemical Sensor with PDMS and a SR-FBG

Many recent papers have been published on the use of fiber Bragg gratings (FBGs) as fiber optic chemical sensors. The literature has demonstrated excellent sensitivity to changes in the surrounding refractive index (SRI) by monitoring shifts in the Bragg wavelength. Nevertheless, the research does not create a link between changes in SRI and chemical sensing. Without the ability to detect and classify specific chemicals, the FBG, by itself, is inadequate as a chemical sensor.

In order to create the link between changes in SRI and chemical sensing and overcome the limitations of the previous fiber optic based chemical sensors, a fiber optic chemical sensor was presented using a SR-FBG and a chemically selective sensing material. The primary contribution was combining the SR-FBG with a material that is (1) compatible with the optical properties of the SR-FBG and (2) exhibits good chemical selectivity. Polydimethylsiloxane (PDMS) satisfies both of these requirements because it has an index of refraction (n$\sim$1.41) that is lower than that of the optical fiber core, is optically transparent at the operating wavelength, and is only sensitivity to a specific class of chemicals, namely volatile organic compounds. The sensor has a minimum detectable concentration of 4000 parts per million for dichloromethane and about 6000 parts per million for acetone.

10.1.10 Using the SR-FBG as a Multi-dimensional Bend Sensor

The SR-FBG was shown to be able to measure bend in two dimensions due to the unique positioning of the grating above the central axis of the optical fiber. Unlike traditional FBGs that are fabricated along the central axis, the SR-FBG experiences strain as the fiber is bent. Due to two unique strain components the Bragg wavelength shifts and the maximum reflectivity decreases making it possible to correlate these changes to bend direction.

10.1.11 Theoretical Demonstration of a Vernier SR-FBG Sensor

Due to the holographic fabrication and masking steps in the fabrication of SR-FBGs, only minor changes to the fabrication process are required to create structured gratings. Structured gratings are desirable because they create multiple peaks in the reflection or transmission spectra that can be used to create a Vernier based sensor. Unlike most of the other sensors presented where the environmental variable is measured by tracking the Bragg wavelength, a Vernier based sensor would detect the environmental variable by monitoring the difference in the transmitted power of the multiple peaks from the structured grating. This work used this idea

to theoretically show that the sensitivity of a sensor could be greatly increased using the Vernier effect.

To demonstrate the effect, the previous volatile organic compound sensor was simulated as a Vernier device. Using conservative numbers for the source power it was shown that the minimum detectable signal for dichloromethane decreases to 10-40 parts per million depending on the type of structured grating that is used.

10.1.12 Fabricating Structured SR-FBGs

The final contribution of this work is the demonstration of fabricated structured SR-FBGs. The only fabrication step that is altered is the mask that is used to predefine the grating region on the surface of the D-fiber. Furthermore, it was shown that these masks could be created using a quality laser printer eliminating the need for expensive mask making equipment and processes.

10.2 Future Work

There is still much work that can be done to develop the full potential of the SR-FBG not only as a sensing device, but also as a device that could be used for filtering or other telecommunication applications. The most obvious next step is to demonstrate the increased sensitivity that would come when using the structured gratings in a Vernier sensor configuration. The theoretical leap of nearly two orders of magnitude would be a significant step forward for the actual implementation of FBGs as chemical sensors.

Another future application of the SR-FBG would be as a steep turn on filter. Because the grating modulation is a result of the high contrast air-cladding interface very steep edges to the grating stop band are realizable. If this path is to be followed further work should be done on etching the gratings deeper into the fiber using an ICP RIE or by etching the gratings into the core of the optical fiber. Initial work shows that the gratings can be fabricated in the core of the fiber by stopping the developing process with IPA instead of water. The water causes the photoresist to swell and not adhere properly in the core of the fiber.

Perhaps the most significant next step in the surface relief technology is the creation of the gratings using E-beam lithography instead of the two beam interference method. Using an E-beam to create the grating pattern gives the engineer the added freedom of easily creating a grating chirp or appodization profile that would be difficult to create other wise. Phase shifts in the grating structure could also be easily created in a similar manner to phase masks that are created using E-beam technology.

The E-beam could also be used to create multiple short gratings each with a different grating period. In this way gradient fields could be easily measured with the SR-FBG by monitoring the peak of each individual grating. Measuring a gradient field in this way would not be possible with standard UV written gratings because they would be too short to produce a detectable reflected signal. The high contrast SR-FBG on the other hand should work very well in such a situation.

In conclusion, this research has shown the diversity of sensing applications that can be met using a SR-FBG. The fabrication process has been refined and the simulation tools have be improved upon in order to make the SR-FBG a valuable sensor.

Bibliography

[1] S. R. Baker, H. N. Rourke, V. Baker, and D. Goodchild, "Thermal decay of fiber Bragg gratings written in boron and germanium codoped silica fiber," *J. Lightwave Technol.*, vol. 15, pp. 1470–1477, 1997. xxix, 66

[2] J. M. López-Higuera, Ed., *Handbook of Optical Fibre Sensing Technology.* Chichester, UK: Wiley, 2002. 1, 3

[3] R. Kashyap, *Fiber Bragg Gratings.* San Diego, CA: Academic, 1999. 2, 17, 66, 187

[4] K. H. Smith, "In-fiber optical devices based on d-fiber," Ph.D. dissertation, Brigham Young Univ., Provo, UT, Apr. 2005. 3, 8, 12, 14, 19, 180

[5] H. T. Stokes, *Solid State Physics.* Provo, UT: Brigham Young Univ., 2000. 7

[6] A. Othonos and K. Kalli, *Fiber Bragg Gratings: Fundamentals and Applications in Telecommunications and Sensing.* Boston: Artech House, 1999. 8, 10, 16, 18, 35, 179, 183, 184, 185, 187

[7] G. Meltz, W. W. Morey, and W. H. Glenn, "Formation of Bragg gratings in optical fibers by a transverse holographic method," *Opt. Lett.*, vol. 14, pp. 823–825, 1989. 9, 37, 65

[8] A. N. Cryssis, S. M. Lee, S. B. Lee, S. S. Saini, and M. Dagenais, "High sensitivity evanescent field fiber bragg grating sensor," *Photon. Tecnol. Lett.*, vol. 17, pp. 1253–1255, 2005. 11

[9] T. Erdogan, "Fiber grating spectra," *J. Lightwave Technol.*, vol. 15, pp. 1277–1294, 1997. 13

[10] D. L. Lee, *Electromagnetic Principles of Integrated Optics.* New York, NY: John Wiley & Sons, Inc., 1986, pp. 209–245. 13

[11] P. Giaccari, "Fiber bragg grating characterization by optical low coherence reflectometry and sensing applications," Ph.D. dissertation, Ecole Polytechnique Fédérale de Lausanne, Switzerland, Apr. 2003. 16, 185

[12] J. E. Roman and K. A. Winnick, "Waveguide grating filters for dispersion compensation and pulse compression," *J. Quantum Electron.*, vol. 29, p. 975, 1993. 17

[13] P. G. Verly, J. A. Wild, and R. L. Buron, "Synthesis of high rejection filters with fourier transform method," *Appl. Opt.*, vol. 28, pp. 2864–2875, 1989. 17

[14] L. A. Weller-Brophy and D. G. Hall, "Analysis of waveguide gratings: application of rouard's method," *J. Opt. Soc. Am. B*, vol. 2, pp. 863–871, 1985. 17

[15] M. Yamada and K. Sakuda, "Analysis of almost periodic distributed feedback slab waveguides via a fundamental matrix approach," *Appl. Opts.*, vol. 26, pp. 3474–3478, 1987. 17

[16] H. Nagata, N. Miyamoto, T. Saito, and R. Kaizu, "Reliable jacket stripping of optical fibers," *J. Lightwave Technol.*, vol. 12, pp. 727–729, 1994. 26

[17] H. Park, S. Lee, U. C. Paek, and Y. Chung, "Noncontact optical fiber coating removal technique with hot air stream," *J. Lightwave Technol.*, vol. 23, pp. 551–557, 2005. 26

[18] M. J. Matthewson, C. R. Kurkjian, and J. R. Hamblin, "Acid stripping of fused silica optical fibers without strength degradation," *J. Lightwave Technol.*, vol. 15, pp. 490–495, 1997. 26

[19] M. A. Jensen and R. H. Selfridge, "Analysis of etching induced birefringence changes in elliptic core fibers," *Appl. Opt.*, vol. 31, pp. 2011–2016, 1992. 27

[20] S. H. Cho, J. Park, B. Kim, and M. H. Kang, "Fabrication and analysis of chirped fiber bragg gratings by thermal diffusion," *ETRI Journal*, vol. 26, pp. 371–374, 2004. 35

[21] J. D. Freeze and R. H. Selfridge, "D-fiber holographic diffraction gratings," *Opt. Eng.*, vol. 32, pp. 3267–3271, 1993. 37

[22] B. A. Mello, I. F. Costa, C. R. A. Lima, and L. Cescato, "Developed profile of holographically exposed photoresist gratings," *Appl. Opt.*, vol. 34, pp. 597–603, 1995. 39

[23] E. Udd, W. Schulz, and J. Seim, "Measurement of multidimensional strain fields using fiber grating sensors for structural monitoring," in *SPIE Conference on Fiber Optic Sensor Technology and Applications*, R. O. Clause and J. W. B. Spillman, Eds., vol. Proc. SPIE 3986, 1999, pp. 24–34. 45

[24] K. H. Smith, B. L. Ipson, T. L. Lowder, A. R. Hawkins, R. H. Selfridge, and S. M. Schultz, "Surface-relief fiber bragg gratings for sensing applications," *Appl. Opt.*, vol. 45, pp. 1669–1675, 2006. 45

[25] R. B. Dyott, *Elliptical Fiber Waveguides*. Artech House, 1995. 46, 47

[26] C. Tsao, *Optical Fibre Waveguide Analysis*. Oxford, 1992. 46

[27] Y. Fujii and K. Sano, "Polarization transmission characteristics of optical fibers with elliptical cross-section," *Trans. Inst. Electron. and Commun.*, vol. 63, pp. 87–93, 1980. 46

[28] N. J. Cronin, *Microwave and Optical Waveguides*. Philadelphia: Institute of Physics Publishing, 1995. 49

[29] M. J. Li and S. I. Najafi, "Polarization dependence of grating-assited waveguide bragg reflectors," *Appl. Opt.*, vol. 32, pp. 4517–4521, 1993. 50

[30] L. A. Weller-Brophy and D. G. Hall, "Local normal mode analysis of guided mode interactions with waveguide gratings," *J. Lightwave Technol.*, vol. 6, pp. 1069–1082, 1988. 50

[31] R. W. Gruhlke and D. G. Hall, "Comparison of two approaches to the waveguide scattering problem: Tm polarization," *Appl. Opt.*, vol. 23, pp. 127–133, 1984. 50

[32] J. Yamauchi, M. Sekiguchi, O. Uchiyama, J. Shibayama, and H. Nakano, "Modified finite-difference formula for the analysis of semivectorial modes in step-index optical waveguides," *IEEE Photon. Tech. Lett.*, vol. 9, pp. 961–963, 1997. 50

[33] P. Verly and R. Tremblay, "Application of the effective-index method to the study of distributed feedback in corrugated waveguides: Tm polarization," *J. Opt. Soc. Am.*, vol. 70, pp. 1218–1221, 1980. 50

[34] G. Weitman and A. Hardy, "Reduction of coupling coefficients for distributed bragg reflection in corrugated narrow-rib waveguides," *IEE Pro. Optoelectron.*, vol. 144, pp. 101–103, 1997. 50

[35] *BeamPROP^{TM} User's Guide*, RSoft Inc., 200 Executive Blvd., Ossining, NY 10562, 2001. 52

[36] R. B. Dyott and P. F. Shrank, "Self-locating elliptically cored fibre with an accessible guiding region," *Electron. Lett.*, vol. 18, pp. 980–981, 1982. 59

[37] D. J. Markos, B. L. Ipson, K. H. Smith, S. M. Schultz, R. H. Selfridge, T. D. Monte, R. B. Dyott, and G. Miller, "Controlled core removal from a d-shaped optical fiber," *Appl. Opt.*, vol. 42, pp. 7121–7125, 2003. 60

[38] M. H. Cordaro, D. L. Rode, T. S. Barry, and R. R. Krchnavek, "Precision fabrication of d-shaped optical fibers," *J. Lightwave Technol.*, vol. 12, pp. 1524–1531, 1994. 60

[39] A. Othonos and K. Kalli, *Fiber Bragg Gratings: Fundamentals and Applications in Telecommunications and Sensing.* Artech, 1999. 65, 67

[40] T. Ergodan, V. Mizrahi, P. J. Lemaire, and D. Monroe, "Decay of ultraviolet-induced fiber Bragg gratings," *J. Appl. Phys.*, vol. 76, pp. 73–80, 1994. 66, 86

[41] G. Brambilla and H. Rutt, "Fiber Bragg gratings with enhanced thermal stability," *Appl. Phys. Lett.*, vol. 80, pp. 3259–3261, 2002. 66

[42] S. Pal, J. Mandal, T. Sun, K. T. V. Grattan, M. Fokine, F. Carlsson, P. Y. Fonjallaz, S. A. Wade, and S. F. Collins, "Characteristics of potential fiber bragg grating sensor-based devices at elevated temperatures," *Meas. Sci. Technol.*, vol. 14, pp. 1131–1136, 2003. 66

[43] A. Martinez, I. Y. Krushchev, and I. Bennion, "Thermal properties of fiber bragg gratings inscribed point-by-point by infrared femtosecond laser," *Electron. Lett.*, vol. 41, pp. 19–20, 2005. 66

[44] D. M. Hernández, V. P. Minkovich, and J. Villatoro, "High-temperature sensing with tapers made of microstructured optical fiber," *Photon. Tecnol. Lett.*, vol. 18, pp. 511–513, 2006. 66

[45] G. M. H. Flockhart, R. R. J. Maier, J. S. Barton, W. N. MacPherson, J. D. C. Jones, K. E. Chisholm, L. Zhang, I. Bennion, I. Read, and P. D. Foote, "Quadratic behavior of fiber bragg grating temperature coefficients," *Appl. Opt.*, vol. 43, pp. 2744–2751, 2004. 69, 89

[46] M. N. McLandrich, "Core dopant profiles in weakly fused single-mode fibers," *Electron. Lett.*, vol. 24, pp. 8–10, 1988. 72

[47] K. Shiraishi, Y. Aizawa, and S. Kawakami, "Beam expanding fiber using thermal diffusion of the dopant," *J. Lightw. Technol.*, vol. 8, pp. 1151–1161, 1990. 72

[48] A. H. Rose, "Annealing optical fiber: Applications and properties," *The American Ceramic Society Bulletin*, vol. 79, pp. 40–43, 2000. 73, 89

[49] M. Tachikura and T. Haibara, "Devitrification effect on optical-fiber strength reduction by fusion splicing," *J. Lightw. Technol.*, vol. 3, pp. 662–668, 1985. 73

[50] A. H. Rose, "Devitrification in annealed optical fiber," *J. Lightw. Technol.*, vol. 15, pp. 808–814, 1997. 73

[51] J. Kvavle, S. H. Schultz, and R. M. Selfridge, "Low loss elliptical core d-fiber to panda fiber fusion splicing," *Opts. Express*, vol. 16, pp. 13 552–13 559, 2008. 77

[52] A. J. van Wyk, P. L. Swart, and A. A. Chtcherbakov, "Fibre bragg grating gas temperature sensor with fast response," *Meas. Sci. Technol.*, vol. 17, pp. 1113–1117, 2006. 85, 86

[53] B. W. Asay, S. F. Son, P. M. Dickson, L. B. Smilowitz, and B. F. Henson, "An investigation of the dynamic response of thermocouples in inert and reacting condensed phase energetic materials," *Propellants, Explosives, Pyrotechnics*, vol. 30, pp. 199–208, 2005. 85

[54] T. L. Lowder, K. H. Smith, B. L. Ipson, A. R. Hawkins, R. H. Selfridge, and S. M. Schultz, "High-temperature sensing using surface relief fiber bragg gratings," *IEEE Photon. Tech. Lett.*, vol. 17, pp. 1926–1928, 2005. 86

[55] S. W. Lloyd, J. A. Newman, D. R. Wilding, R. H. Selfridge, and S. M. Schultz, "Compact optical fiber sensor smart node," *Rev. of Sci. Instrum.*, vol. 78, p. 035108, 2007. 87

[56] W. Kunzler, J. Newmann, D. Wilding, Z. Zhu, T. Lowder, R. Selfridge, and S. Schultz, "Advanced fbg sensing through rapid spectral interrogation," *Proc. SPIE*, vol. 6933, 2008. 87

[57] S. H. Cho, J. Park, B. Kim, and M. H. Kang, "Fabrication and analysis of chirped fiber bragg gratings by thermal diffusion," *ETRI Journal*, vol. 26, pp. 371–374, 2004. 91, 97

[58] D. Chardon and S. J. Huard, "Thermal diffusivity of optical fibers measrued by photoacoustics," *Appl. Phys. Lett.*, vol. 41, pp. 341–342, 1982. 94

[59] X. Chapeleau, D. Leduc, C. Lupi, F. Lopez-Gejo, M. Douay, R. L. Ny, and C. Boisrobert, "Local characterization of fiber-bragg gratings through combined use of low-coherence interferometry and a layer-peeling algorithm," *Appl. Opt.*, vol. 45, pp. 728–735, 2006. 97

[60] G. C. Frye and S. J. Martin, "On-line monitoring of volatile organic species," *Pollution Tech. Rev.*, vol. 212, pp. 215–224, 1993. 100

[61] D. P. Campbell, J. L. Moore, and J. M. . Cobb, "Optical system-on-a-chip for chemical and biochemical sensing: the chemistry," vol. Proc. SPIE 3540, 1998, pp. 153–161. 101

[62] J. Conzen, J. B$'$urck, and H. J. Ache, "Characterization of a fiber-optic evanescent wave absorbance sensor for nonpolar organic compounds," *Applied Spectroscopy*, vol. 47, pp. 753–763, 1993. 101, 102

[63] R. A. Potyrailo and G. M. Hieftie, "Use of the original silicone cladding of an optical fiber as a reagent-immobilization medium for intrinsic chemical sensors," *Fresenius J. Anal. Chem.*, vol. 364, pp. 32–40, 1999. 101, 102

[64] D. Degrandpre and L. W. Burgess, "A fiber-optic ft-nir evanescent field absorbance sensor," *Applied Spectroscopy*, vol. 44, pp. 273–279, 1990. 101

[65] G. L. Klunder and R. E. Russo, "Core-based intrinsic fiber-optic absorption sensor for the detection of volatile organic compounds," *Applied Spectroscopy*, vol. 49, pp. 379–385, 1999. 101

[66] X. Chen, K. Zhou, L. Zhang, and I. Bennion, "Optical chemsensor based on etched tilted bragg grating structures in multimode fiber," *Photon. Technol. Lett.*, vol. 17, pp. 864–866, 2005. 102, 106

[67] W. Liang, Y. Huang, Y. Xu, R. K. Lee, and A. Yariv, "Highly sensitive fiber bragg grating refractive index sensors," *Appl. Phys. Lett*, vol. 86, pp. 151 122–151 124, 2005. 102, 106

[68] A. Iadicicco, S. Campopiano, A. Cutolo, and M. Giordano, "Refractive index sensor based on microstructured fiber bragg grating," *Photon. Technol. Lett.*, vol. 17, pp. 1250–1252, 2005. 102, 106, 129

[69] G. B. Tait, G. C. Tepper, D. Pestov, and P. M. Boland, "Fiber bragg grating multi-functional chemical sensor," vol. Proc. SPIE 5994, 2005, p. 32. 102

[70] M. V. Chandak, Y. S. Lin, W. Ji, and R. J. Higgins, "Sorption and diffusion of volatile organic compounds in polydimethylsiloxane membranes," *J. of Appl. Polymer Sci.*, vol. 67, pp. 165–175, 1998. 102

[71] S. V. Dixon-Garrett, K. Nagai, and R. D. Freeman, "Ethylbenzene solubility, diffusivity, and permeability in polydimethylsiloxane," *Phys. Rev. Lett.*, vol. 39, pp. 1461–1472, 2000. 103

[72] K. Speath, G. Kraus, and G. Gauglitz, "In-situ characterization of thin polymer films for applications in chemical sensing of volatile organic compounds by spectroscopic ellipsometry," *Fresenius J. Anal. Chem.*, vol. 357, pp. 292–296, 1997. 103

[73] J. N. Lee, C. Park, and G. M. Whitesides, "Solvent compatibility of poly(dimethylsiloxane)-based microfluidic devices," *Anal. Chem.*, vol. 75, pp. 6544–6554, 2003. 103, 109

[74] F. M. Araújo, L. A. Ferreira, J. L. Santos, and F. Farahi, "Temperature and strain insensitive bending measurements with d-type fibre bragg gratings," *Meas. Sci. Technol.*, vol. 12, pp. 829–833, 2001. 113

[75] P. M. Blanchard, J. G. Burnett, G. R. G. Erry, A. H. Greenaway, P. Harrison, B. mangan, J. C. Knight, P. J. Russell, M. J. Ganders, R. McBride, and

J. D. C. Jones, "Two-dimensional bend sensing with single, multi-core optical fibre," *Smart Mater. Struct*, vol. 9, pp. 132–140, 2000. 113

[76] L. Jin, W. Zhang, J. Li, H. Zhang, B. Liu, Q. Tu, G. Kai, and X. Dong, "Two-dimensional bend sensing with a cantilever-mounted fbg," *Meas. Sci. Technol.*, vol. 17, pp. 168–172, 2006. 113

[77] X. Dong, H. Meng, Z. Liu, G. Kai, and X. Dong, "Bend measurement with chirp of fiber bragg grating," *Smart Mater. Struct*, vol. 10, pp. 1111–1113, 2001. 114, 116

[78] Y. Sen, Z. Yong, Z. C. Zhuo, W. Zheng, Y. Quian, and Y. S. Zhang, "Bend sensor using an embedded etched fiber bragg grating," *Micro. and Opt. Technol. Lett.*, vol. 43, pp. 414–417, 2004. 124

[79] B. J. Eggleton, P. A. Krug, L. Poladian, and F. Ouellette, "Long periodic superstructure bragg gratings in optical fibers," *Elect. Lett.*, vol. 30, pp. 1620–1622, 1994. 129

[80] L. A. Johansson, J. T. Getty, Y. A. Akulova, G. A. Fish, and L. A. Coldren, "Sampled-grating dbg laser-based analog optical transmitters," *J. Lightw. Technol.*, vol. 21, pp. 2968–2976, 2003. 129

[81] Y. Dai, X. Chen, X. Xu, C. Fan, and S. Xie, "High channel-count comb filter based on chipred sampled fiber bragg grating and phase shift," *Photon. Tecnol. Lett.*, vol. 17, pp. 1040–1042, 2005. 129

[82] X. Liu, "A dual-wavelength sampled fiber bragg grating and its application in l-band dual-wavelength erbium-doped fiber lasers," *Photon. Tecnol. Lett.*, vol. 18, pp. 2114–2116, 2006. 131, 201

[83] Y. O. Barmenkov, "Effective length of short fabry-perot cavity formed by uniform fiber bragg gratings," *Opts. Express*, vol. 14, pp. 6394–6399, 2006. 133

[84] X. Peng and C. Roychouduri, "Design of high finesse, wideband fabry-pérot filter based on chirped fiber bragg grating by numerical method," *Opt. Eng.*, vol. 39, pp. 1858–1862, 2000. 134

[85] J. W. Noh, R. Anderson, S. Kim, J. Cardenas, and G. P. Nordin, "In-plane photonic transduction of silicon-on-insulator microcantilevers," *Opts. Express*, vol. 16, pp. 12 114–12 123, 2008. 137, 139

[86] C. H. Wang, L. R. Chen, and P. W. E. Smith, "Analysis of chipred-sampled and sampled-chirped fiber bragg gratings," *Appl. Opt.*, vol. 41, pp. 1654–1660, 2002. 141

[87] X. Liu, Y. Gong, L. Wang, T. Wang, T. Zhang, K. Lu, and W. Zhao, "Identical dual-wavelength fiber bragg gratings," *J. Lightw. Technol.*, vol. 25, pp. 2706–2710, 2007. 199

Appendix

Appendix A

Detailed Processes

A.1 Fiber Preparation and Etching

1. Brake off section of D-fiber ∼80 cm in length.

2. Use the Luminos jacket striper or mechanical heat stripper to strip of the jacket on both ends of the fiber and a section ∼2 cm in length in the middle of the fiber.

3. Place the fiber in the etch boat with the shiny side flat side up and the stripped middle region in the center of the etch boat.

4. Cleave both ends of the fiber by placing the fiber flat side up in the Fujikura precision cleaver or using the "Battle-ax".

5. Slide the two fiber holders of the etch boat close together.

6. If the fiber does not bend straight up or down or the bend is not in the center of the stripped region adjust the placement of the fiber.

7. Place the stripped center region in the isopropanol alcohol (IPA) of the ultra sonic cleaner and turn the ultra sonic cleaner. The ultra sonic cleaner automatically turns off when the cleaning cycle is done.

8. Take the fiber out of the ultra sonic cleaner and slide the fiber holders away from each other to make the fiber taught.

9. Dry the fiber off with compressed air. It is important to blow the IPA off of the fiber or else a residue is left behind.

10. Place the fiber in a bath of DeContam and think good thoughts. Leave the fiber in the bath for at least a few minutes and then wash off the DeContam with DI water.

11. Clean out the water container in the fume hood, fill it up with DI water, and place it in the metal pan in the fume hood.

12. Place the etch boat on the water container and place the ends of the fiber in the xyz stage and optical power detector.

13. Connect the 1550 nm laser to the xyz stage and turn on the laser. Make sure that the polarizers are placed both at the source (on the xyz stage) and in front of the detector. The polarizers should be placed at 45° angles with respect to the flat surface of the D-fiber.

14. Align the fiber to the laser source by adjusting the xyz stage until maximum power is achieved.

15. The wavelength adjust knob can be used to check to see if the fiber is correctly aligned with respect to the polarizers. As the wavelength is tuned the power should fluctuate. It is best to try to get at least a 3 dB swing.

16. Put on personal protection equipment appropriate for HF handling (two pairs of gloves, apron, goggles, and face shield).

17. Make sure there is sufficient air flow through the fume hood.

18. Slightly open the lid of the HF to loosen the seal and place the container of HF in the metal pan in the fume hood.

19. Finish taking the lid off of the HF, being careful to watch out for droplets of HF that may be on the top of the lid, and place the lid upside down inside of the fume hood.

20. Place the etch boat on the container of HF and slide the fiber holders together so that ∼2 cm of the stripped fiber is immersed in the HF.

21. Close the fume hood door.

22. Start the Labview etching program.

23. Etch the fiber until the desired etch depth has been achieved by watching the complete oscillations in the output power. Usually the fiber is taken out at 3 oscillations which corresponds to ∼0.4 μm of cladding left above the core. (See Figure 3.5. Remove the fiber and put it directly into the DI water.

24. Put the lid on the HF container and put it back in its storage place.

25. Stop the Labview etching program.

26. Turn off the laser.

27. Slide the fiber holders away from each other to make the fiber taught and rinse clean using the bottle of DI water.

28. It is usually best to take the fiber into the clean room as quickly as possible to avoid any further contamination.

A.2 Sulfuric Acid Etch

1. Take the etch boat and the fiber into the clean room.

2. Suit up in the acid gear including an apron, splash goggles, face shield, and acid gloves.

3. Place a beaker of sulfuric acid onto a hot plate and heat the acid to 190°C.

4. Place the etch boat onto the beaker. Slide the magnets together until the stripped section of the fiber is submersed. If any jacket is immersed into the acid it will be eaten away.

5. Leave the fiber in the acid for ∼5 minutes.

6. Place the fiber into a beaker of water while you clean up and remove the acid gear.

7. Rinse the fiber in running water for 3 minutes.

A.3 Prepare the Fiber for Photoresist Application

A.3.1 Dehydration Bake

1. Tape the fiber to a clean wafer flat side up using the polyimide tape. Check to make sure that the fiber is flat side up with a microscope

2. Place the fiber in a dehydration oven set at 120°C.

3. Leave the fiber in the oven for at least an hour. It does not hurt to leave the fiber in the oven longer than an hour. Be very careful at this point because the fiber ends often get caught under wafer holders or other clean room users put containers on top of them.

A.3.2 Short RIE Etch to Roughen Up the Surface

1. Remove the fiber from oven and check to make sure that it is still flat side up.

2. Place the wafer and the fiber into the Anelva RIE.

3. Follow the standard operating procedures for the RIE.

4. Etch the fiber for 30 seconds using only CF_4 gas set to a flow rate of 12.5 and at a power of 300 watts. The flow should be at 12.5 during the etch. This flow rate usually corresponds to a set rate of $\sim$12.1.

A.4 Photoresist Application

1. Apply Surpass 4000 to the etched section of the fiber for one minute.

2. Rinse the fiber in running DI water. Rinse for at least 10 seconds.

3. Dry the fiber with nitrogen.

4. Re-tape the fiber to the center of the wafer. This re-tape is important because water is often underneath the tape that can cause the photoresist not spin on properly. Check the fiber under a microscope to ensure that it is flat side up.

5. With the fiber flat side up, place the end of four 2-inch pieces of tape on the back of the wafer. Wrap the excess fiber around the wafer sticking it to these pieces of tape. Once wrapped, stick the tape down on the other side of the wafer. NOTE do not squeeze the tape loop together.

6. Place the wafer on the spinner, turn on the vacuum pump.

7. Apply thinned Shipley 700 1.2L photoresist to the etched area of the fiber. The photoresist should be thinned 2 parts of resist to 1 part thinner. It is best to use photoresist that has been thinned recently. If the photoresist is older than a week, new photoresist should be thinned.

8. Spin the wafer and the fiber at 6000 rpm for 1 minute with an acceleration of 15.

9. Turn off the vacuum pump and place the wafer on a hot plate set to 90°C for 1 minute.

10. Take the fiber off the hotplate and remove the tape. Hopefully the tape is still looped. If it is not a razor blade can be used to assist in the tape removal. Be careful not to break the wafer or cut the fiber with the blade.

11. Remount the fiber parallel to the flat edge of the wafer about 1 inch above the edge. Make sure the fiber is flat side is up. Check the edges of the etched region (closest to the tape) using a microscope to make sure that the fiber is flat side up. Do not check the whole length of the fiber or else the photoresist will be prematurely exposed.

12. Place the wafer and fiber in a black wafer holder. Try to wrap the the ends of the fiber inside of the holder. Be careful not to break the ends when closing the holder.

A.5 Expose the Fiber

1. Turn on the"LASER IN USE" sign.
2. Put the correct safety goggles on for use with UV wavelengths.
3. Turn on UV curing lamp. This lamp is used to pre-expose the fiber to define the grating region.
4. Measure the power at the mirror. To determine exposure time divide 21000 by the power (in microwatts), this gives the exposure time in seconds.
5. Set the shutter to the appropriate time interval.
6. Make sure only the yellow lights are on.
7. Remove the fiber from the black wafer holder.
8. Place the desired mask over the fiber (uniform of some length, super structured, or Fabry-Pérot) and expose the fiber under the UV lamp for 30 seconds.
9. Mount the wafer next to the mirror with the fiber in a horizontal position. The wafer and fiber should be mounted so that the edge of the etched region is at the edge of the mirror. Check to maker sure that the fiber is parallel to the optics table and perpendicular to the mirror.
10. Turn off the yellow lights and open the shutter (the shutter automatically closes at the end of the preset time interval.)
11. Place the wafer back into the black wafer holder.

A.6 Develop the Fiber

1. Take the fiber back into the clean room. DO NOT take it out of the black wafer holder until under yellow lights.
2. Place the wafer in the white dipper holder.

3. Immerse the wafer and the fiber in the developer, MF-24A, for 10 seconds. Agitate the wafer while in the developer.

4. Remove the wafer from the developer and place it under running DI water to stop the developing process. Rinse the fiber and the wafer thoroughly.

5. Dry the fiber and the wafer with nitrogen.

6. Place the wafer on a hotplate set to 90°C for five minutes. This hard bakes the photoresist.

7. After baking the fiber it is very likely not to be flat side up. Check the fiber under the microscope and remount it if necessary. Remount the fiber back in the middle of the wafer.

8. Continue to use the black wafer holder to transport the wafer and fiber. This will help to keep the fiber clean.

9. Test the fiber Bragg grating by looking at its reflection and transmission spectra.

A.7 Transfer the Grating into the Glass

1. Place the wafer into the Anelva RIE.

2. Follow the standard operating procedures for the RIE.

3. Etch the fiber for 1 minute using just CF_4 gas and the same settings as described above in Section A.3.2.

A.8 Remove the Photoresist

1. Use a cleanroom swab soaked in acetone to remove the photoresist from the fiber.

2. Remove the tape and allow acetone and IPA to freely run down the fiber.

3. If so desired the fiber can be placed in IPA in an ultra-sonic cleaner.

4. Blow dry the fiber using nitrogen.

Appendix B

Transfer Matrix Code

The transfer matrix method that was presented in Ch. 2 was shown to be an accurate method for the modeling of FBGs. This appendix explains the implementation of the transfer matrix method using MATLAB. Examples of uniform and non-uniform gratings are presented. The method is valid as long as the discrete uniform sections are modeled to be much longer than a grating period.

The implementation of the method is mostly taken from Othonos and Kali [6]. The transfer matrix method consists of the discretization of any grating structure into uniform grating pieces. The uniform grating pieces are solved using the analytical solution to the coupled mode equations in matrix form. The matrix solutions for each uniform grating piece are multiplied together to give the full grating response. To create a full reflection or transmission spectrum the method is applied for a number of different wavelengths.

B.1 The Coupling Coefficient for SR-FBGs

Besides the grating length, the strength of the grating in the code can be defined by the coupling coefficient, κ, or by the change in the effective index of the guided mode, d_{neff}. These parameters can be determined either numerically or experimentally for the SR-FBGs of this work. Experimentally these parameters are found by measuring the transmission or reflection spectra of a SR-FBG and fitting these spectra to the output spectra from the transfer matrix method for a given grating length.

To find κ numerically the modes in the unperturbed D-fiber are first found without a grating according to the previous work of Smith [4]. To construct the unperturbed waveguide it is assumed that the D-fiber cross section extends to the center line of the grating. The resulting fields are then used in Eq. (2.3) to find the coupling coefficient. The integration is performed from the center line of the grating to the surface of the grating at the given point in z. For example, if at a certain point in z there is a trough in the grating, the electric field is integrated from the center of the grating down to the bottom of the grating. Figure B.1 shows a diagram of a D-fiber with a grating on the top surface. At the right in the figure is a vertical cut of the fiber showing how the topography varies in the z-direction.

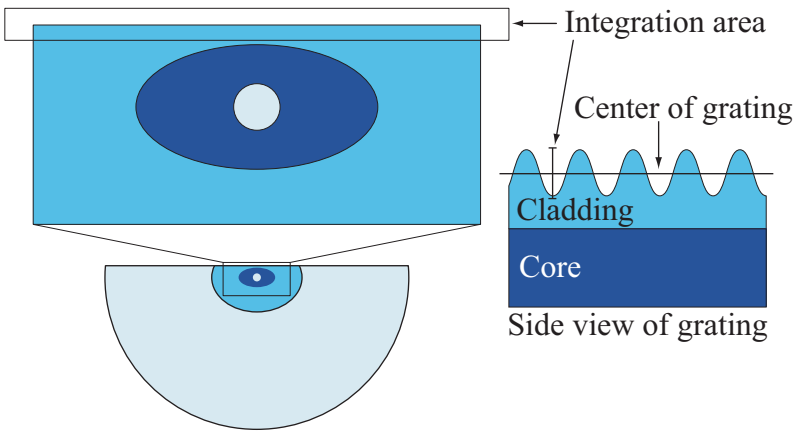

Figure B.1: Diagram showing the profile of a grating on a D-fiber from the front and side.

In practice, once the field of the mode is found, it is interpolated onto a finer grid, and κ is determined as a function of the grating height for a given number of points between a trough and a peak. In a trough, the height is $\frac{-h}{2}$ and at a grating peak the height is $\frac{h}{2}$, where h is the peak-to-trough grating height. Once *kappa* is determined as a function of the grating height, the median value is then used as the coupling coefficient in the transfer matrix method.

B.2 Examples of Different FBG Structures

The model has been setup in order to simulate many different grating structures without having to make major changes to the code. The main inputs for the code are:

- `n0: the effective index of the guided mode`
- `L: the grating length`
- `lambda_d: the desired Bragg wavelength`
- `lambda: the wavelengths overwhich to perform the simulation`
- `k: the coupling coefficient`
- `dneff: the average effective index change`
- `on_off: the grating structure, 1 is grating 0 is no grating`

The array on_off controls the structure of the FBG. The array should be created such that it represents one unit cell of overall grating structure. Examples of how this array is constructed are given in the following examples.

B.2.1 A Uniform FBG

The uniform FBG is the simplest grating structure to simulate. For a uniform FBG only one transfer matrix is needed to describe the full grating structure. The on_off array is set to 1. Figure B.2 shows the simulated reflection and transmission spectra for a 1 cm long uniform grating with a coupling strength of 300 m^{-1}.

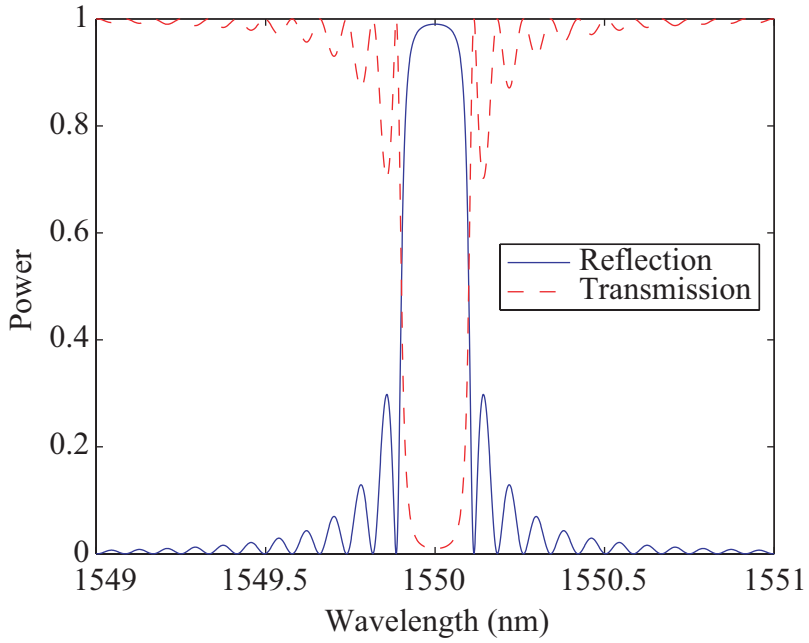

Figure B.2: Simulated reflection and transmission spectra for a uniform FBG.

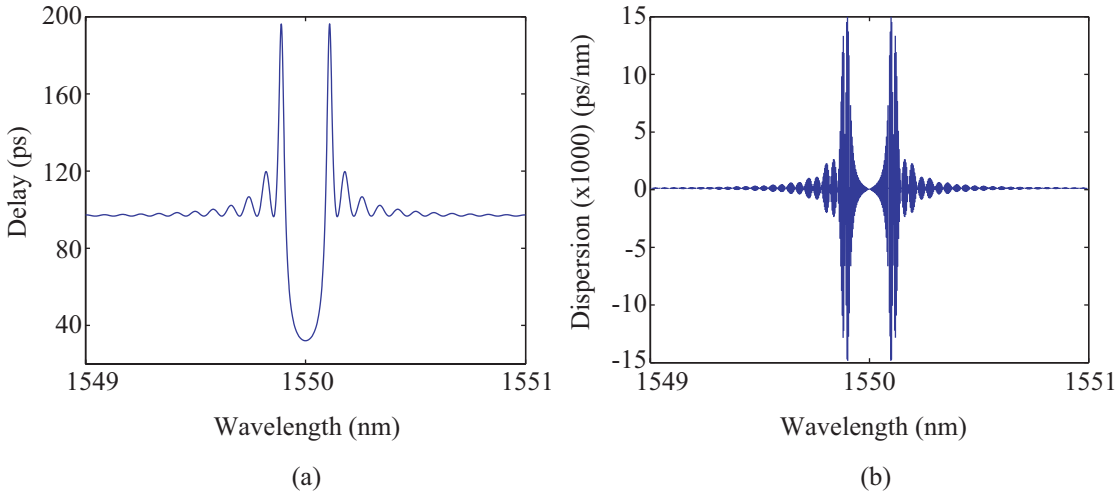

Figure B.3: Simulated (a) group delay and (b) dispersion from a uniform FBG.

The group delay and the dispersion of the reflected light from the grating can be determined from the phase of complex reflection coefficient, r [6]. The phase of the reflected light is given as

$$\phi = \arctan \frac{Imag(r)}{Real(r)}. \tag{B.1}$$

The group delay, τ, for the light reflected back from the grating is given as

$$\tau = \frac{d\phi}{d\omega} = \frac{\lambda^2}{2\pi c}\frac{d\phi}{d\lambda}, \tag{B.2}$$

where c is the speed of light. The dispersion D is the rate of change of the group delay and is therefore given as

$$\begin{aligned} D &= \frac{d\tau}{d\lambda}, \\ &= \frac{2\tau}{\lambda} - \frac{\lambda^2}{2\pi c}\frac{d^2\phi}{d\lambda^2}. \end{aligned} \tag{B.3}$$

Figure B.3 show the simulated group delay and dispersion of the reflected light for the uniform FBG.

The function used to create the uniform grating is:

```
function [on_off, k_temp, dz_temp]=uniform(k, L)

%---k is the coupling coefficient
%---L is the grating length

on_off=[1];
k_temp=[k];
dz_temp=L;
```

B.2.2 Modeling Chirped FBGs

A chirped FBG is a grating in which either the period or the DC refractive index varies along the grating length. The result of such a variation is a reflection bandwidth that is increased. The increase in reflection bandwidth can be understood

as a grating with different Bragg conditions that are met by a larger wavelength spectrum. With all other variables being equal, the increase in bandwidth results in a decrease in reflectivity. Figure B.4(a) shows a diagram of a period chirped refractive index profile while Fig. B.4 shows a diagram of a DC index chirped profile.

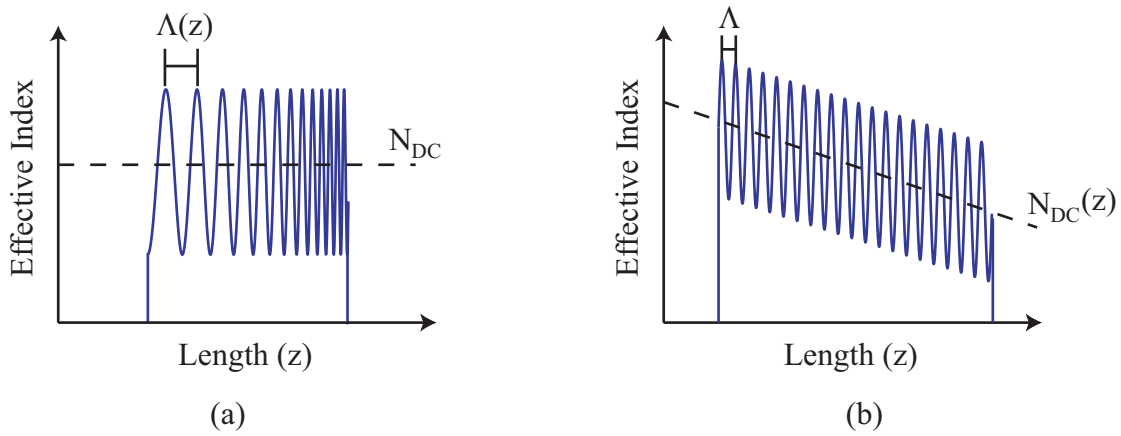

Figure B.4: Diagram of a (a) period chirp and (b) index chirp profile along the grating length.

The transfer matrix method makes modeling of a chirped FBG very easy. The chirped grating is first discretized into small uniform grating sections each with its own grating period and DC index profile. To create the chirp, the subsequent section of grating has a different grating period or DC index. This approach is continued for the full length of the grating. It should be noted that because the modeling of the chirp is done in a discrete manner, the results might differ slightly than those found experimentally which most likely experience a continuous chirp. In most situations this fact is not detrimental to the simulation of real gratings. The modeler must remember though that the individual grating sections should be much longer than a grating period. A length of 50 times longer than the grating period is a good rule of thumb [6].

Figure B.5(a) shows the reflection spectrum from a simulated chirped 1 cm long FBG. The coupling coefficient is again set to 300 m^{-1} and the chirp is a linear

period chirp from 534.25 nm to 534.75 nm. There are several things to notice about the chirped grating's reflection spectrum compared to the reflection spectrum of the uniform grating. The first is the increase in bandwidth from about 0.2 nm for the uniform grating of Fig. B.2 to about 2.0 nm for the chirped grating. The second important feature to notice is the decrease in reflectivity for the chirped grating. The third noticeable feature is the reduction in the Fabry-Pérot like fringes on either side of the main lobe. This reduction is due to the fact that both sides of the grating no longer reflect the same wavelength [11]. The last spectral feature to notice is the non-uniformity across the top of the spectrum.

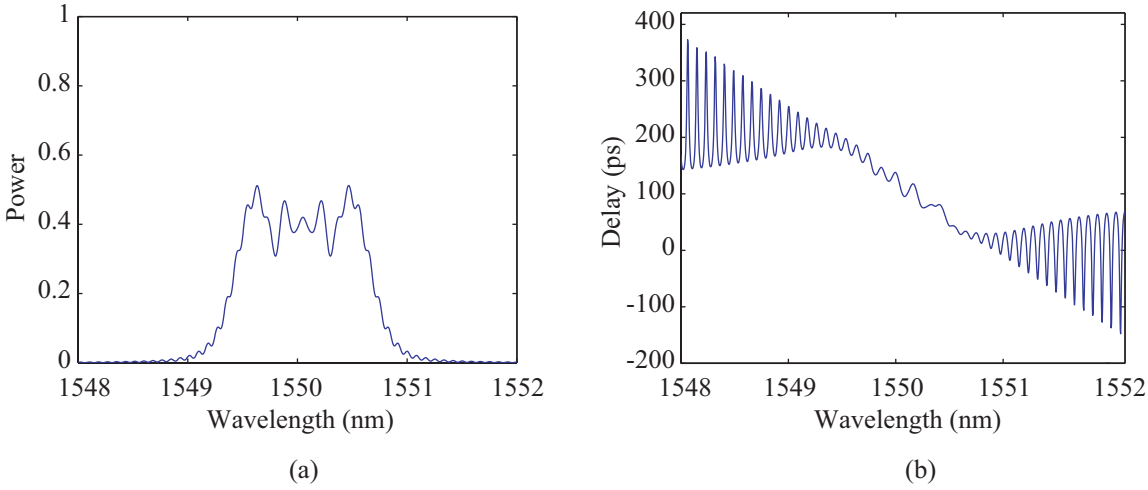

Figure B.5: Simulated (a) reflection spectrum and (b) group delay of a chirped fiber Bragg grating.

Besides spectral differences, the dispersion properties of a chirped grating are also different then those for a uniform grating. Fig. B.5(b) shows the group delay of the reflected light from the grating. Because the rate of change of the group delay is no longer zero in the region of the design wavelength the light experiences dispersion as it propagates the length of the grating. This property is very useful as dispersion compensation in many existing telecommunication networks [6].

The function used to create the chirped grating is:

```
function [on_off, k_temp, dz_temp, Lam, n0]=chirped(opt,k, L, Lam, n0,...
start, stop, mm)

%---opt = 'p' means the chirp is a period period chirp
%---opt = 'i' means the chirp is an index chirp
%---mm is the number of discrete pieces used to create the chirp
%---start is the starting index or grating period for the chirp
%---stop is the stoping index or grating period for the chirp

if opt=='i'
    on_off=1;
    on_off=repmat(on_off,1,mm);
    dz_temp=L/mm;
    dz_temp=repmat(dz_temp,1,mm);
    n0=linspace(start,stop,mm);
    Lam=repmat(Lam,1,mm);
    k_temp=repmat(k,1,mm);

elseif opt=='p'
    on_off=1;
    on_off=repmat(on_off,1,mm);
    dz_temp=L/mm;
    dz_temp=repmat(dz_temp,1,mm);
    n0=repmat(n0,1,mm);
    Lam=linspace(start,stop,mm);
    k_temp=repmat(k,1,mm);

else
    disp('Error: Please specify the type of chirp');
    return;
end
```

B.2.3 Modeling Apodized FBGs

In many applications it is desirable to lower the reflectivity of the sidelobes with respect to the main lobe. This process is known as apodization and consists of a variation along the fiber in the envelope of the refractive index modulation amplitude. For example, if the FBG is to be used in a wavelength division multiplexing scheme as a wavelength filter then it is important to have high rejection of the non-filtered light in order to eliminate cross talk across channels [6]. Another important use of apodization is to eliminate the non-uniformities across the top of the spectrum for a chirped grating. Eliminating these irregularities also linearizes the group delay for improved dispersion compensation [3].

Again the transfer matrix method works well for simulation of an apodized grating. The same process of discretization that is used for a chirped grating is again used for the apodized grating. Because the grating is being split into discrete sections the same rule of thumb for grating lengths needs to be used.

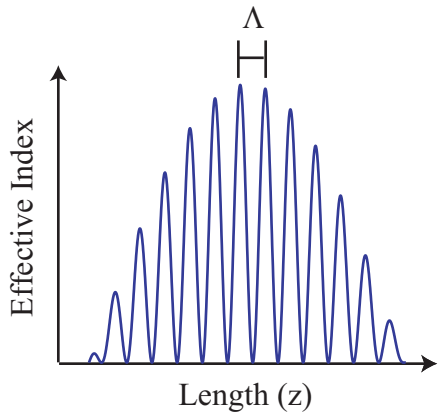

Figure B.6: Diagram of a raised-cosine apodization index profile.

Figure B.6 shows a diagram for the index of refraction profile of an apodized grating. There are many apodizing functions which may be used to reduce the grating sidelobes. Two common functions are the Gaussian and the raised-cosine. The

Gaussian profile is of the form

$$n_{eff}(z) = d_{neff}\exp\left(\frac{4\ln 2(z-a_0)^2}{\mathrm{FWHM}^2}\right), \tag{B.4}$$

where N_{DC} is the DC effective index value. The raised-cosine profile is of the form

$$n_{eff}(z) = d_{neff}\frac{1}{2}\left[1+\cos\left(\frac{\pi(z-a_0)}{FWHM}\right)\right], \tag{B.5}$$

where a_0 corresponds to the middle of the apodizing function.

Figure B.7(a) shows a comparison of the uniform FBG spectrum to the the spectrum from a raised-cosine apodized FBG. Again both gratings are simulated as 1 cm long with a maximum coupling coefficient of 300 m^{-1}. Fig. B.7 shows the same spectra in units of dB. The apodizing function is centered at the middle of the grating with a FWHM equal to half the grating length. The reduction in the sidelobes reflectivity is immediately noticeable to around -40 dB. Other noticeable differences are the the reduction in overall reflectivity and a broadening of the main lobe. These are the major tradeoffs whenever side lobe reduction is performed in many different engineering applications.

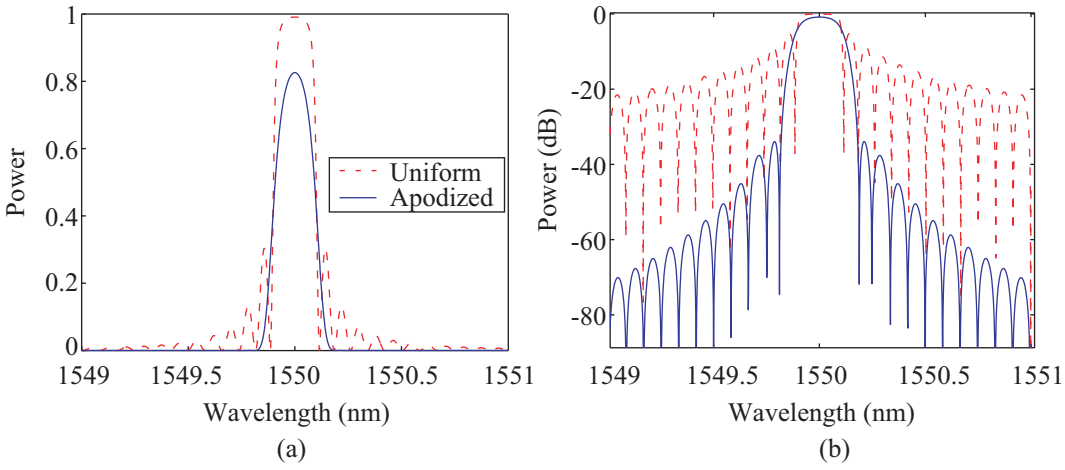

Figure B.7: Simulated reflection spectra for a uniform and apodized FBG.

Figure B.8(a) shows the result of apodizing the chirped grating of the previous section with the same apodizing profile of this section. As expected the

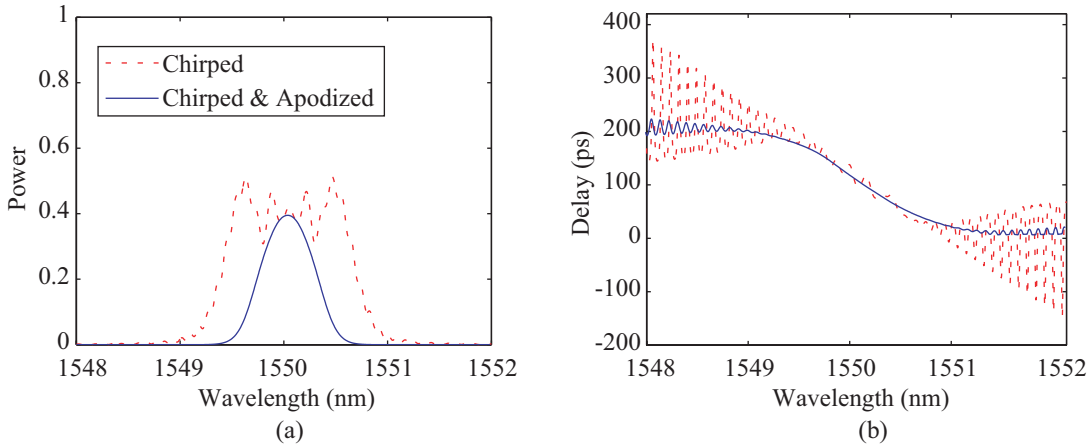

Figure B.8: Comparison of (a) reflection spectra and (b) group delay for a chirped only and chirped/apodized FBG.

irregularities at the top of the spectrum disappear. There is however a slight reduction in the bandwidth and the reflectivity indicating that the irregularities in the chirped spectrum are due to side lobes that are reduced when the grating is apodized. Fig. B.8(b) shows the resulting group delay when the chirped grating is apodized. The delay is a much smoother function and even exhibits a linear trend in the center which could be extremely important in telecommunication applications.

The function used to create the chirpted grating is:

```
function [on_off, k_temp, dz_temp]=apodized(opt,k, L, FWHM, a0, mm)

%---opt = 'c' is a raised-cosine apodization
%---opt = 'g' is a gaussian apodization
%---FWHM is the full-width-half-max of the apodizing function
%---a0 is the center of the apodizing function
%---mm is the number of discrete segments

if opt=='c'
    on_off=1;
    on_off=repmat(on_off,1,mm);
    dz_temp=L/mm;
```

```
    dz_temp=repmat(dz_temp,1,mm);

    %%% The apodizing function %%%
    z_temp=(1:1:mm).*dz_temp;
    k_temp=1/2*k.*(1+cos(pi.*(z_temp-a0)/(FWHM)));

elseif opt=='g'
    on_off=1;
    on_off=repmat(on_off,1,mm);
    dz_temp=L/mm;
    dz_temp=repmat(dz_temp,1,mm);

    %%% The apodizing function %%%
    z_temp=(1:1:mm).*dz_temp;
    k_temp=k.*exp(-4.*log(2).*(z_temp-a0).^2./(FWHM.^2));

else
    disp('Error: Please specify the type of apodizing function');
    return;
end
```

B.2.4 Modeling Super Structured FBGs

The transfer matrix code lends itself to the modeling of super structured gratings with uniform subgratings. In order to model the super structured grating the unit cell of the grating structure is first identified as one subgrating and one gap. In the code this is represented as:

```
on_off=[1 0];
k_temp=[k 0];
dz_temp=[sub_grat gap];
```

The unit cell is then extended the full grating length and the simulation performed. Figure B.9 shows examples of the reflection spectra from a SS-FBG with varying duty

cycles. In the simulation the subgratings and total grating length are fixed at 100 μm and 1.5 cm respectively. The change in the effective index is set to 2x10^{-4}.

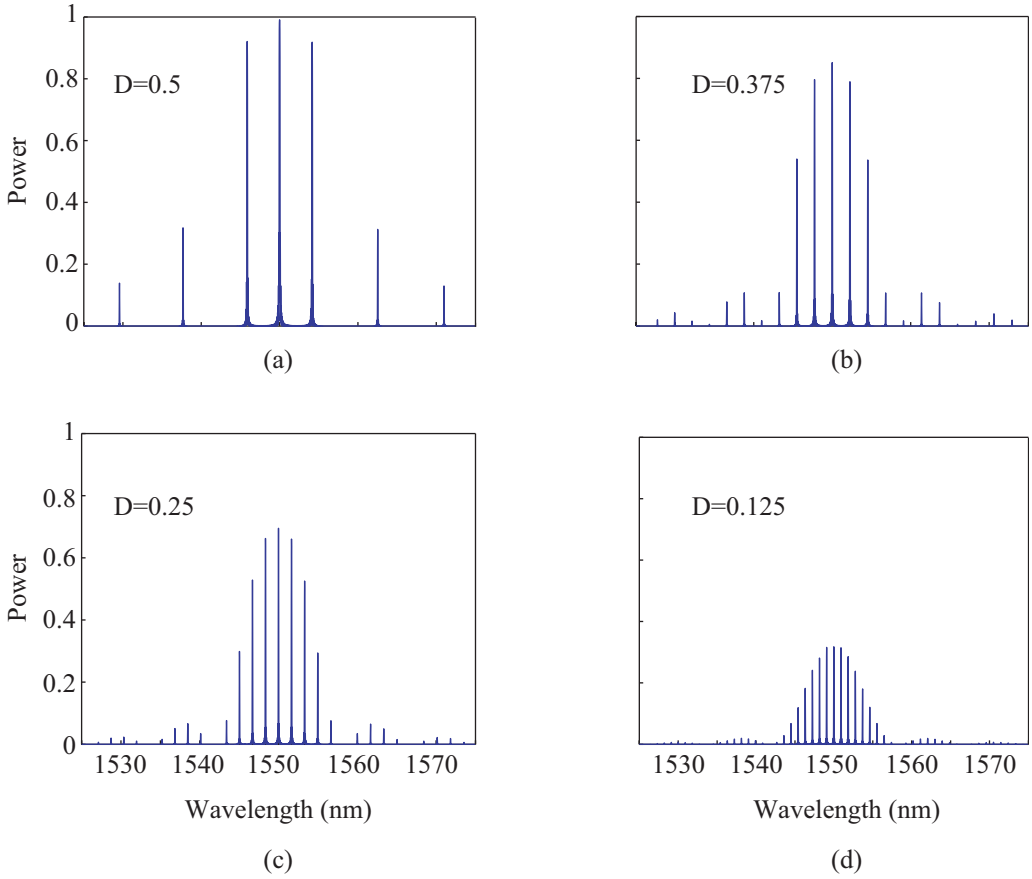

Figure B.9: Simulated reflection spectra for SS-FBGs with (a) a 50% duty cycle, (b) a 37.5% duty cycle, (c) a 25% duty cycle, and (d) a 12.5% duty cycle.

The function for the super structured grating is:

```
function [on_off, k_temp, dz_temp, Lam, n0]=super_structured(k, L,...
 sub_grat, gap)

%---sub_grat is the length of one subgrating section
%---gap is the length of one gap region
```

```
on_off=[1 0];
dz_temp=[sub_grat gap];
k_temp=[k 0];

%mm is the number of discrete sections for a given length L
mm=floor(L./sum(dz_temp));

%extends on_off of the grating to cover the full length, L
on_off=repmat(on_off,1,mm);

%extends dz_temp to cover the full grating
dz_temp=repmat(dz_temp,1,mm);

%extends the coupling coef to cover the full grating
k_temp=repmat(k_temp,1,mm);
```

B.2.5 Modeling Fabry-Pérot FBGs

Another type of structured grating is the FP-FBG. Unlike the SS-FBG that consists of many subgratings and many gaps, the FP-FBG consists of only two subgratings with one gap. In order to model this type of grating again the unit cell of the grating structure is identified as:

```
on_off=[1 0 1];
k_temp=[k1 0 k2];
dz_temp=[FBG1 0 FBG2];
```

The unit cell is the complete grating structure therefore it does not need to be extended any further as is the case with a SS-FBG. Figure B.10 shows the simulated reflection spectrum from a FP-FBG.

The function for simulating a FP-FBG is:

```
function [on_off, k_temp, dz_temp]=fabry_perot(k1, k2, FBG1, gap, FBG2)

%---k1 is the grating strength of the first mirror
%---k2 is the grating strength of the second mirror
%---FBG1 is the grating length for the first mirror
%---gap is the length between the two mirrors
%---FBG2 is the grating length for the last mirror

on_off=[1 0 1];
k_temp=[k1 0 k2];
dz_temp=[FBG1 gap FBG2];
```

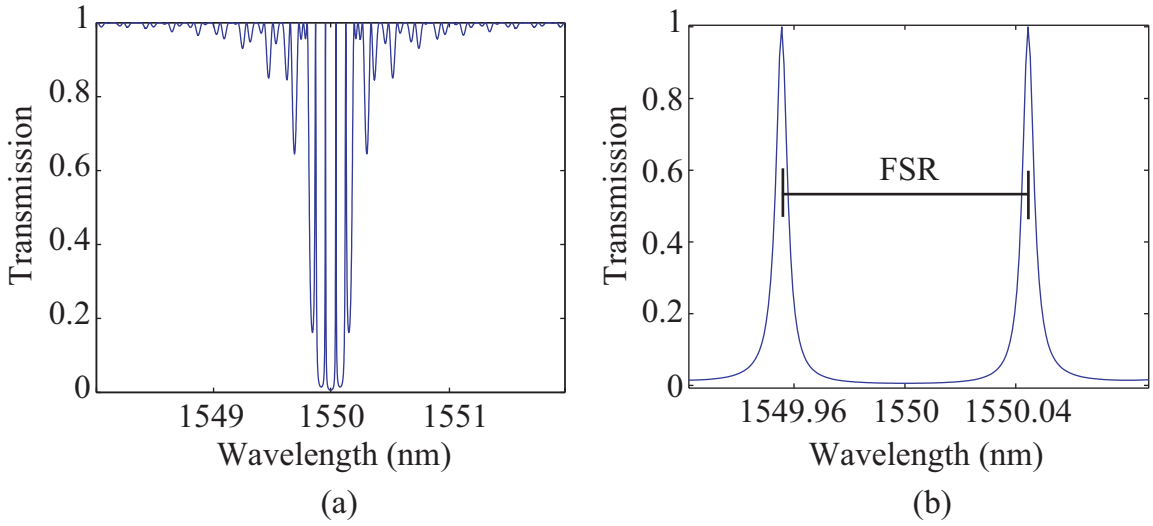

Figure B.10: (a) Simulated transmission spectrum of FP-FBG. (b) Same spectrum zoomed in around two of the transmission peaks.

B.3 The Main Code

```
clear all; close all;

tic
N=2000;                 %Number of wavelength samples
L=1e-2;                 %Length of the grating
n0=1.45                 %Avergage effective index
dneff=2e-4;             %Change in effective index
lambda_d=1550e-9;       %Design wavelength

%---initial conditions 'u' is the forward propagating wave and 'v'...
%---is the backward propagating wave
uv=[1;0];

%---Wavelength range for simulation (1 nm / 1000 points = 1 pm resolution)
lambda=linspace(1549e-9,1551e-9,N);

%---Set or calculate kappa
%k=300;                 %coupling strength in m^-1;
k=pi*dneff/lambda_d    %Calculate kappa

%---Period of the grating.  This can either be set or calculated from the
%---design wavelength
Lam=lambda_d/(2*(n0));

%---Call the function of the grating you wish to simulate
[on_off, k_temp, dz_temp]=uniform(k, L);
%[on_off, k_temp, dz_temp, Lam, n0]=chirped('i', k, L, Lam, n0, n0,...
% n0+.001, 100);
%[on_off, k_temp, dz_temp]=apodized('g',k, L, L/2, L/2, 100);
%[on_off, k_temp, dz_temp]=super_structured(k, L, 100e-6, 100e-6);
```

```
%[on_off, k_temp, dz_temp]=fabry_perot(k, k, 3.5e-3, 5e-3, 3.5e-3)

M=length(on_off);

%---Extend the variables that might not have been extend in the functions
if length(Lam)~=M
    Lam=repmat(Lam,1,M);
end
if length(n0)~=M
    n0=repmat(n0,1,M);
end

for n=1:N
    n
    for m=1:M
        dz=dz_temp(m);
        k=k_temp(m);

        del=2*pi*n0(m)/lambda(n)-pi/Lam(m);
        alpha=sqrt(abs(k).^2-del.^2);

        %---transfer matrix kernel
        T11=cosh(alpha*dz)+i*del/alpha*sinh(alpha*dz);
        T12=k/alpha*sinh(alpha*dz);
        T21=k'/alpha*sinh(alpha*dz);
        T22=osh(alpha*dz)-i*del/alpha*sinh(alpha*dz);
        T_temp=[T11 T12; T21 T22];

       if m==1
           T=T_temp*eye(2);
       else
           T=T_temp*T;
```

```
       end
    end
    %---fields after propagating through the grating
    umvm=T*uv;
    r(n)=umvm(2)/umvm(1);                %Complex reflection coefficient
    R(n)=abs(umvm(2))^2/abs(umvm(1))^2;  %Reflectance
    Tran(n)=1/abs(umvm(1))^2;            %Transmittance
end
toc
%---Check to make sure the grating is the right length
check=sum(dz_temp)

figure(1);
plot(lambda*1e9,R)
titel('Reflection')

figure(2);
plot(lambda*1e9,Tran)
title('Transmission')

figure(3);
P_R=10*log10(R);
P_t=10*log10(Tran);
plot(lambda*1e9,P_t,lambda*1e9,P_R)
title('Reflection and Transmission in dB')

phase=atan(imag(r)./real(r));
delay=2*lambda(1:end-1).^2./(2.*pi.*3e8).*(diff(phase)./diff(lambda));

figure(4)
ind=find(delay>=0);
plot(lambda(ind)*1e9,delay(ind)*1e12);
```

```
title('Group delay')

lambda=lambda(ind);
delay=delay(ind);
dispersion=2*delay(1:end-2)./lambda(1:end-2)...
-lambda(1:end-2).^2./(2.*pi.*3e8).*...
(diff(phase(ind),2)./diff(lambda,2));

figure(5)
plot(lambda(1:end-2)*1e9,dispersion(1:end)*1000)
title('Dispersion')
```

Appendix C

Fourier Analysis of Super Structured Gratings

While the transfer matrix method gives a general intuition as to the wavelength location of each resonant peak an analytical expression for the peak separation can be determined using Fourier methods due to the periodic nature of the sampling function. The long period super structure, $f(z)$, can be thought of as a rectangular function of length L, $rect_L(z)$, convolved with a comb of delta functions with a period P, $comb_P(z)$ [87].

$$f(z) = rect_L(z) \otimes comb_P(z). \tag{C.1}$$

Figure C.1 shows the resulting structure that results from the convolution.

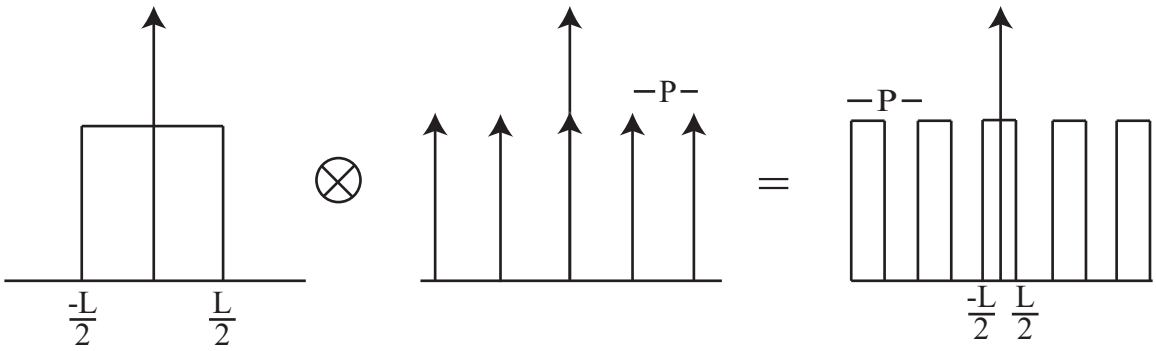

Figure C.1: Diagram showing the convolution of a rect function with a comb of delta functions to create the periodic super-structure of the grating.

The spatial Fourier transform is applied to the periodic super-structured grating envelope $f(z)$ in order to determine the spatial frequencies of the resonant

peaks. Basic Fourier theory states that the Fourier transform of two functions that are convolved in the spatial domain is simply the product of the Fourier transforms of each individual function. Equation C.2 shows the Fourier transform relationship

$$F(\beta) = F\{rect_L(z)\}F\{comb_P(z)\}, \tag{C.2}$$

where β is defined as the spatial frequency. The spatial frequency β equals $\frac{2\pi}{\Lambda}$.

The Fourier transform of $f(z)$ in Eq. C.1 is given by

$$F(\beta) = \frac{2\sin(\frac{L}{2}\beta)}{\beta}\frac{2\pi}{P}\sum_{n=-\infty}^{\infty}\delta\left(\beta - n\frac{2\pi}{P}\right). \tag{C.3}$$

Eq. C.3 can be shifted such that it is centered about the designed grating period. The shifted equation is given as

$$F(\beta-\beta_0) = \frac{2\sin\left[\frac{L}{2}(\beta-\beta_0)\right]}{\beta-\beta_0}\frac{2\pi}{P}\sum_{n=-\infty}^{\infty}\delta\left(\beta - \beta_0 - n\frac{2\pi}{P}\right). \tag{C.4}$$

where $\beta_0 = \frac{2\pi}{\Lambda_0}$ and Λ_0 is the designed grating period.

Figure C.2 shows the absolute value of the Fourier transform for a superstructure that consists of 100 μm wide grating sections with a 50% duty cycle. The dashed line represents the envelope of the Fourier transform and the solid lines represent the actual Fourier components. Each of these Fourier components creates a resonant peak in the reflection spectrum of the SS-FBG.

The resonant wavelength spacing, or spacing between Fourier components, can be solved analytically by taking the partial derivative of the spatial frequency with respect to the designed Bragg wavelength. The spatial frequency is defined as

$$\beta = \frac{2\pi}{\Lambda}, \tag{C.5}$$

where $\Lambda = \frac{\lambda_B}{2n_{eff}}$ is derived from the grating equation. The partial derivative of the spatial frequency with respect to the Bragg wavelength is found to be

$$\frac{\partial\beta}{\partial\lambda_B} = \frac{-4\pi n_{eff}}{{\lambda_B}^2}. \tag{C.6}$$

The partial derivative is replaced with a Δ representation and the negative sign ignored to give the channel spacing as

$$\Delta\lambda = \frac{{\lambda_B}^2\Delta\beta}{4\pi n_{eff}}. \tag{C.7}$$

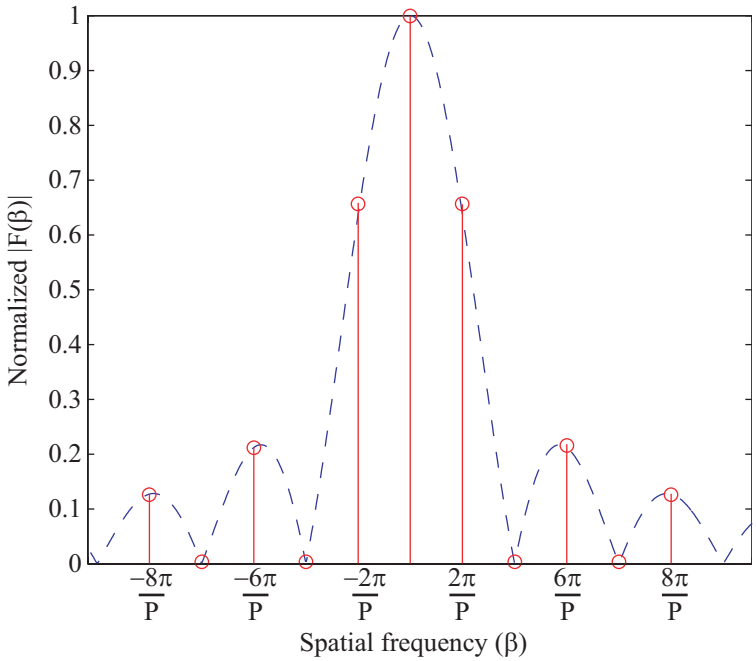

Figure C.2: Graph showing the normalized magnitude of the Fourier transform for a super-structured grating with a 50% duty cycle.

The spacing between the spatial frequencies of the Fourier components, $\Delta\beta$, is given in Eq. C.4 as $\frac{2\pi}{P}$. Substituting into Eq. C.7 gives the final spacing between resonant reflection peaks as [82]

$$\Delta\lambda = \frac{{\lambda_B}^2}{2n_{eff}P}. \tag{C.8}$$